7-1-2003

Spectral imaging of human portraits and image quality

Qun Sun

SPECTRAL IMAGING OF HUMAN PORTRAITS AND IMAGE QUALITY

by

Qun Sun

B.S. East China Normal University, Shanghai, China (1985)
M.S. Florida International University, Miami, USA (1997)

A dissertation submitted in partial fulfillment of
the requirements of the degree of Doctor of Philosophy
in the Chester F. Carlson Center for Imaging Science
of the College of Science
Rochester Institute of Technology

July 2003

Signature of the Author_____

Accepted by_____ 7/31/03

Coordinator, Ph.D. Degree Program Date

CHESTER F. CARLSON
CENTER FOR IMAGING SCIENCE
COLLEGE OF SCIENCE
ROCHESTER INSTITUTE OF TECHNOLOGY
ROCHESTER, NEW YORK

CERTIFICATE OF APPROVAL

Ph.D. DEGREE DISSERTATION

The Ph.D. Degree Dissertation of Qun Sun
has been examined and approved by the
dissertation committee as satisfactory for the
dissertation requirement for the Ph.D. degree
in Imaging Science

Dr. Mark D. Fairchild

Dr. Edward M. Granger

Dr. Roy S. Berns

Dr. Francisco H. Imai

07/31/03
Date

THESIS RELEASE PERMISSION
ROCHESTER INSTITUTE OF TECHNOLOGY
COLLEGE OF SCIENCE
CHESTER F. CARLSON
CENTER FOR IMAGING SCIENCE

Title of Dissertation

SPECTRAL IMAGING OF HUMAN PORTRAITS AND IMAGE QUALITY

I, Qun Sun, hereby grant permission to the Wallace Memorial Library of R.I.T. to reproduce my thesis in whole or in part. Any reproduction will not be for commercial use or profit.

Signature of Author

08/12/03

Date

SPECTRAL IMAGING OF HUMAN PORTRAITS AND IMAGE QUALITY

By

Qun Sun

Submitted to the Chester F. Carlson Center for Imaging Science
College of Science In partial fulfillment of the requirements
for the Ph.D. degree at the Rochester Institute of Technology

April 2003

ABSTRACT

This dissertation addresses the problem of capturing spectral images for human portraits and evaluating image quality of spectral images. A new spectral imaging approach is proposed in this dissertation for spectral images of human portraits. Thorough statistical analysis is performed for spectral reflectances from various races and different face parts. A spectral imaging system has been designed and calibrated for human portraits. The calibrated imaging system has the ability to represent not only the facial skin but also the spectra of lips, eyes and hair from various races as well. The generated spectral images can be applied to color-imaging system design and analysis.

To evaluate the image quality of spectral imaging systems, a visual psychophysical image quality experiment has been performed in this dissertation. The spectral images were simulated based on real spectral imaging system. Meaningful image quality results have been obtained for spectral images generated from different spectral imaging systems. To bridge the gap between the physical measures and subjective visual perceptions of image quality, four image distortion factors were defined. Image quality metrics were obtained and evaluated based statistical analysis and multiple regression analysis. The image quality metrics have high correlation with subjective assessment for image quality. The image quality contribution of the distortion factors were evaluated.

As an extension of the work other researchers in MCSL have initiated, this dissertation research will, working with other researchers in MCSL, put effort to build a publicly accessible database of spectral images, Lippmann2000.

DEDICATION

This dissertation is dedicated to those who make my life so special—

Zhuanfen, Jeffrey, and my parents.

Acknowledgements

I would like to use this opportunity to express my deep thanks to those who participated my experiment and helped me to make this dissertation research done.

I would like to thank Dr. Ed. Granger for his guidance and support. Special thanks for his will to be my dissertation committee chair.

I would give great thanks to Dr. Roy Berns for his tough and worthy course teaching which makes this dissertation research possible and much easy. Also thanks for his guidance and support for this dissertation research.

I would like to thank Dr. F. Imai for his guidance, inspiration and support. He makes my research papers much better than their originals. I also get many suggestions from discussing with him.

I would like to thank Mrs. Paula Alessi for her guidance and support. Also thanks to Eastman Kodak Co. for their financial support for this dissertation research.

I would like to thank Dr. Ethan Montag for his support. I apologize deeply that I forgot to acknowledge his great help in my CIC09 and JIST papers.

I would like to thank Dr. Noboru Ohta for his teaching me at the knowledge of color system optimization.

I would like to thank Dr. Mitchell Rosen and Dr. Garrett Johnson for their help and suggestions in programming.

Great thanks to faculty, staff members and students of Munsell Color Science Laboratory and Center for Imaging Science for their support and friendship.

I would like to give my great thank to my wife, Zhuanfen, for her inspiration and her special gift, our son, Jeffrey. They make my life so special.

Finally, I would like to give my great, special thanks to my advisor, Dr. Mark Fairchild for his guidance, encouragement, inspiration and support. Without his help, this dissertation can not be done.

TABLE OF CONTENTS

LIST OF FIGURES X
LIST OF TABLES XV

1. INTRODUCTION.....1

2. BACKGROUND LITERATURE REVIEW.....5

2.1 Spectral Characterization of Human Face.....5
2.1.1 Spectral Characterization of Human Skin.....5
2.1.2 Spectral Characterization of Eyes, Hair and Lips.....6
2.2 Spectral Imaging.....8
2.2.1 Spectral Image and Spectral Imaging System.....9
2.2.2 Spectral Imaging for Human Portraitures.....11
2.2.3 Principal Components Analysis.....12
2.3 Image Quality for Spectral Imaging.....18
2.3.1 Subjective Measure.....19
2.3.2 Qualitative Objective Measure.....19
2.3.3 Image Quality in Spectral Imaging.....20
2.3.4 Objective Picture Quality Scale (PQS) Method.....21
2.3.5 Color Difference and Color Appearance Models.....23
2.3.6 Color Difference for Color Images.....24
2.3.7 Image Quality of Color Image.....26
2.3.7.1 Graininess Factor.....27
2.3.7.2 Sharpness Factor.....27
2.3.7.3 Contrast Factor.....28
2.4 Spectral Database: Lippmann2000.....28

3. SPECTRAL IMAGING FOR HUMAN PORTRAITURE.....30

3.1 Spectral Imaging System Design.....30
3.2 Imaging System Calibration.....33
3.2.1 Imaging Spot Calibration.....34
3.2.2 Spectral Reflectance of Mirror.....35
3.2.3 Optoelectronic Conversion Function of Digital Camera.....36
3.2.4 Spectral Sensitivities of Digital Camera.....38
3.3 Spectral Imaging Experiment.....40
3.4 Statistical Analysis of Spectral Reflectances of Human Face.....41
3.4.1 PCA Results from Various Races and Different Face Parts.....47
3.4.2 Color Reproduction Based on Different Basis Functions.....51
3.4.3 Statistical Analysis for Skin Spectra.....58
3.4.4 Summary.....66
3.5 Estimating Spectral Image.....67

3.5.1 Linearization and White Correction....68
3.5.2 Transform Matrix....69
3.5.3 Modeling Accuracy....72
3.5.4 Spectral Image Display....77
3.5.5 Noise Discussion....83
3.6 Summary....84

4. IMAGE QUALITY ANALYSIS OF SPECTRAL IMAGE....85

4.1 Simulation of Spectral Imaging System....85
4.1.1 IBM Research Pro\3000 Camera System....86
4.1.2 Simulation of Gray Scale Response....89
4.1.3 Error Correction for Measured Data....92
4.1.4 Simulation of Face Spectral Reflectance Response....97
4.1.4.1 Using 3 Basis Functions....98
4.1.4.2 Using 6 Basis Functions....99
4.1.5 Recalibration for Spectral Imaging System....100
4.1.5.1 Using 3 Basis Functions....101
4.1.5.2 Using 6 Basis Functions....102
4.1.6 Color Accuracy of PCA Using Different Wavelength Steps and Different Number of Basis Function....104
4.1.6.1 PCA Results for Face Spectra....105
4.1.6.2 Simulation Results for Face Spectra....107
4.1.6.3 PCA Results for Vrhel's Spectra....112
4.1.6.4 Simulation Results for Vrhel's Spectra....115
4.1.7 Noise Simulation in Spectral Imaging System....118
4.2 Calibration for LCD Display....119
4.2.1 Device Characterization of LCD Display....120
4.2.1.1 Spectral Characteristics....121
4.2.1.2 Chromaticity Stability of Primaries....122
4.2.1.3 Additivity....124
4.2.2 Characterization of LCD Display....125
4.2.2.1 Primary Transform Matrix....125
4.2.3.2 Electro-optical Transfer Functions....125
4.2.2.3 Calibration Accuracy and Optimization....126
4.2.3 Chromatic Adaptation Transform....129
4.3 Visual Experiment for Image Quality....132
4.3.1 Selection of Target Images....132
4.3.2 Visual Experiment Design....134
4.3.3 Visual Experiment....135
4.4 Comparative Image Quality Analysis....136
4.4.1 Basic Analysis of Visual Experiment Data....136
4.4.1.1 MOS Values....136
4.4.1.2 Color Difference Factor Values....141

4.4.1.3 Graininess Factor Values....143
4.4.1.4 Sharpness Factor Values....146
4.4.1.5 Contrast Factor Values....148
4.4.2 MOS vs. Color Difference Factor....150
4.4.3 MOS vs. Sharpness Factor....153
4.4.4 MOS vs. Graininess Factor....154
4.4.5 MOS vs. Contrast Factor....155
4.4.6 Image Quality Metric....156
4.4.6.1 Correlation Among the Distortion Factors....157
4.4.6.2 Quality Metric PQS....159
4.4.6.3 Contribution of the Distortion Factors....168
4.4.6.4 Limitations of PQS Applications....170
4.4.6.5 Empirical Image Quality Metric....171
4.5 Summary....172

5. CONTRIBUTIONS TO LIPPMANN2000....174

6. CONCLUSIONS....175

6.1 Conclusions in Spectral Imaging for Human Portraits....175
6.2 Conclusions in Image Quality of Spectral Imaging System....176
6.3 Scientific Contributions....177
6.4 Future Work....178

REFERENCES....180

APPENDICES....187

Appendix A: Fairman's Metameric Correction Using Parameric Decomposition....187
Appendix B: Procedure for Spectral Image Display Using sRGB Model....189
Appendix C: MTF of LCD Display....191

LIST OF FIGURES

Figure 2-1. Scheme picture of human skin.....5

Figure 2-2. Measured spectral data of human skin in early research. (a). mean spectral reflectances of human skin from various races (copied from Brunsting & Sheard's work,[13] 1929); (b). spectral transmittance for Hemologlobin and melanin (copied from Buck's work,[19] 1948). 7

Figure 2-3. Conventional PQS system.....22

Figure 2-4. Flow chart of computing S-CIELAB(copied from reference 49) 24

Figure 3-1. Spectral transmittance of filter, 202 half C.T blue.....31

Figure 3-2. Scheme of optic path of the spectral imaging system.....31

Figure 3-3. Picture of the spectral imaging system.....32

Figure 3-4. Spectral radiance of the lighting fallen on subject.....34

Figure 3-5. Spectral reflectance of the mirror.....36

Figure 3-6. The optoelectronic conversion curve of the camera.....37

Figure 3-7. Measured relative spectral sensitivities of digital camera. (a)Without external filter; (b) with external filter.....39

Figure 3-8. Measured spectral reflectances in terms of different races. (a) for Pacific-Asian; (b) for Caucasian; (c) for Black; (d) for Subcontinental-Asian; (e) for Hispanic.....43

Figure 3-9. Measured spectral reflectances in terms of different face parts. (a) for skin; (b) for hair; (c) for eyes; (d) for lips.....45

Figure 3-10. L*, a* b* plot and their corresponding projections for spectra of different races. Red dots are for Pacific-Asian, green for Caucasian, blue for Black, cyan for Hispanic and magenta for Subcontinental-Asian.....46

Figure 3-11. L*, a* b* plot and their corresponding projections for spectra of different parts. Red dots are for skin, green for hair,

blue for eyes and magenta for lips.....46

Figure 3-12. Graphs of the first three principal components of spectral reflectances for individual races and all races. Solid-dot line is for the 1st component, solid line for the 2nd component and dot line for the 3rd component. (a) Pacific-Asian; (b) Caucasian; (c) Subcontinental-Asian; (d) Black; (e) Hispanic; (f) All Races.....49

Figure 3-13. Graphs of the first three principal components of spectral reflectances each facial part. Solid-dot line is for the 1st component, solid line for the 2nd component and dot line for the 3rd component. (a) Skin; (b) hair; (c) eyes; (d) lips.....50

Figure 3-14. Mean spectral reflectances of individual races and all races.....51

Figure 3-15. Mean spectral reflectances of each facial part.....51

Figure 3-16. Mean skin spectral reflectances of individual races and all races.....58

Figure 3-17. Graphs of the first three basis functions for spectral reflectances of facial skin of individual races and all races. Solid-dot line is for the 1st component, solid line for the 2nd component and dot line for the 3rd component. (a) Pacific-Asian; (b) Caucasian; (c) Subcontinental-Asian; (d) Black; (e) Hispanic; (f) All Races.....60

Figure 3-18. Mean spectra of skin for individual races in Oulu data.....62

Figure 3-19. First three basis functions of skin spectra of individual races and all races in Oulu data. Solid-dot line is for 1st component, solid line for 2nd component and dot line for 3rd component. (a) Oulu Pacific-Asian; (b) Oulu Caucasian; (c) Oulu Black; (d) Oulu All.....63

Figure 3-20. Flow chart of estimating the tristimulus values from camera signals.....68

Figure 3-21. Histograms of color differences in modeling. (a) for 3P7T; ((b) for 3P17T; (c) for 6P7T.....74

Figure 3-22. Spectral reflectances of measured and estimated for trial sets of data using 3 basis functions with 7 terms of transform matrix. The abscissa is the wavelength in the unit of nm, the

ordinate is the spectral reflectance factor. 76

Figure 3-23. Original RGB images and estimated spectral images for display from a Pacific-Asian subject.....80

Figure 3-24. Original RGB images and estimated spectral images for display from a Caucasian subject.....81

Figure 3-25. Original RGB images and estimated spectral images for display from a Black subject.....81

Figure 3-26. Original RGB images and estimated spectral images for display from a Subcontinental-Asian subject.....82

Figure 3-27. Original RGB images and estimated spectral images for display from a Hispanic subject.....82

Figure 3-28. Original RGB images and estimated spectral images for display from author wearing glasses.....83

Figure 4-1. IBM Research Pro/3000 system (copied from Reference 71) . (a) copy stand and controller; (b) side lamps; (c) scanner head and column; (d) PC and color monitor. (copied from reference 71).....86

Figure 4-2. Optoelectronic conversion curve for 12 bit quantization at red channel...87

Figure 4-3. Absolute spectral radiant power of IBM Research Pro/3000 side lamp.....88

Figure 4-4. Normalized spectral sensitivity of IBM Research Pro/3000 camera.....88

Figure 4-5. Recalculated spectral sensitivities of DKC-ST5 Camera by using double interpolation procedure.....92

Figure 4-6. Spectral sensitivities of DKC-ST5 Camera by using and without using double interpolation procedure. The solid lines are for results using double interpolation while the doted lines are for conventional method.....93

Figure 4-7. The 4th to 6th basis functions based on all spectral from all races.....104

Figure 4-8. Vrhel's spectral data.....112

Figure 4-9. The first nine basis functions. (a) the first 3 basis functions;

(b) the 4th to 6th basis functions; (c) the 7th to 9th basis functions.....114

Figure 4-10. Spectral transmittance of Kodak Wratten No. 66.....115

Figure 4-11. Spectral radiance of the display white.....121

Figure 4-12. Spectral radiance of the display RGB primaries.....122

Figure 4-13. Measured chromaticity coordinates of RGB ramps.....123

Figure 4-14. Measured chromaticity coordinates of RGB ramps after black correction.....123

Figure 4-15. Electro-optical transfer functions for RGB channels.....126

Figure 4-16. Rendered images of two spectral imaging objects for face Imaging system.....133

Figure 4-17. Rendered images of two spectral imaging objects for IBM DCS Camera.....134

Figure 4-18. Interface for visual experiment.....135

Figure 4-19. MOS from novice observers vs. MOS from expert observers.....137

Figure 4-20. Standard deviations of MOS obtained from novice observers vs. corresponding standard deviations of MOS obtained from expert observers.....138

Figure 4-21. MOS values from image quality visual experiment. (a)Using 3 basis functions; (b) using 6 basis functions; (c) using 9 basis functions.....140

Figure 4-22. Color difference factor values from image quality visual experiment. (a)Using 3 basis functions; (b) using 6 basis functions; (c) using 9 basis functions 143

Figure 4-23. Graininess factor values from image quality visual experiment. (a)Using 3 basis functions; (b) using 6 basis functions; (c) using 9 basis functions.....145

Figure 4-24. The relationship between graininess factor and color difference factor...145

Figure 4-25. Sharpness factor values from image quality visual experiment. (a)Using 3 basis functions; (b) using 6 basis functions;

(c) using 9 basis functions 147

Figure 4-26 factor values from image quality visual experiment. (a)Using 3 basis functions; (b) using 6 basis functions; (c) using 9 basis functions.....149

Figure 4-27. MTF of LCD display.....150

Figure 4-28. MOS vs. mean image color differences. (a) for painting images; (b) for fruit images; (c) for Caucasian images; (d) for Black images.....151

Figure 4-29 MOS vs. standard deviation of image color difference factor. (a) painting images; (b) fruit images; (c) Caucasian images; (d) Black images.....152

Figure 4-30. MOS vs. sharpness factor. (a) for painting images; (b) for fruit images; (c) for Caucasian images; (d) for Black images.....154

Figure 4-31. MOS vs. graininess factor. (a) for painting images; (b) for fruit images; (c) for Caucasian images; (d) for Black images.....155

Figure 4-32. MOS vs. contrast factor. (a) for painting images; (b) for fruit images; (c) for Caucasian images; (d) for Black images.....156

Figure 4-33. PQS versus MOS.....162

Figure 4-34. PQS and MOS values for test images.....164

Figure 4-35. PQS_d versus MOS.....166

Figure 4-36. PQS_d and MOS values for test images.....168

Figure 4-37. MOS vs. Qm.....171

Figure A-1. LCD pixel structure under microscope.....191

Figure. A-2. Step response of the LCD display. a: row of series of dark pixel elements followed by a series of light pixel elements; b: signals that can cause this situation; c: displayed luminance transition; d: fixed unit-step signal; e: luminance response on this signal at various possible positions of the display element; f: average luminance response; g: line-spread function obtained by differentiating the average step response.....192

LIST OF TABLES

Table 3-1. Cumulative contribution percentage of principal components calculated from spectra of all races and individual races. See text for abbreviations.....48

Table 3-2. Cumulative contribution percentage of principal components calculated from face spectra of individual parts.....50

Table 3-3. Mean color difference in reproduction of individual races and all races using different sets of 3 principal components. The horizontal races are the spectral groups that yielded the principal components while the vertical races are the spectral groups the basis functions were applied to. See text for abbreviations.....52

Table 3-4. RMS values and mean metameric indices of spectral reproduction for individual races and all races using different sets of three principal components. The horizontal races are the spectral groups yielded the principal components while the vertical races are the spectral groups the basis functions were applied to. (1) RMS values, unit of 10^{-4}; (2) Metameric indices. See text for abbreviations.....55

Table 3-5. Mean color difference and indices of metamerism in reproduction of individual face parts using different sets of 3 principal components. The horizontal races are the spectral groups yielded the principal components while the vertical races are the spectral groups the basis functions were applied to. (1) Mean color differences; (2) Indices of metamerism.....57

Table 3-6. Cumulative contribution percentage of principal components calculated from spectra of skin spectra for individual races. See text for abbreviations.....59

Table 3-7. Color differences and indices of metamerism in spectral reproduction of skin for individual races when using 3 and 6 basis functions based on all spectra of all races. (1) color difference; (2) indices of metamerism. See text for abbreviations. See text for abbreviations.....61

Table 3-8. Cumulative contribution percentage of principal components calculated from spectra of skin spectra for individual races in Oulu data. PA is Pacific-Asian; C is Caucasian; B is Black; RA is all races.....63

Table 3-9. Color differences of spectral reproduction for skin spectra of individual races and all races in Oulu data using different sets of three principal components. C is Caucasian; PA is Pacific-Asian; B is Black; All skin is all skin spectra in Oulu data.....64

Table 3-10. Mean, maximum, minimum and standard deviation of color difference values calculated between spectral reflectances and their mean spectra in individual races. See text for abbreviations..... ..65

Table 3-11. Results of mean, maximum and minimum color difference values calculated from each pair of skin spectral reflectances of each subject within individual races. See text for abbreviations.....65

Table 3-12. Results of color and spectral reproductions using different transform matrices in system calibration.....73

Table 3-13. Results of color and spectral reproductions for the trial sets of Data using different transform matrices in system calibration.....74

Table 4-1. Linearized digits of Gray Scale Q14 and corresponding percentage errors to the reflectance factors.....90

Table 4-2. . Interpolated digits of Gray Scale Q14 and corresponding percentage errors to the reflectance factors.....91

Table 4-3. The simulated results for gray scales.....94

Table 4-4. Number of targets that their percentage errors in simulation were above 10%, 20%, and 30% for any RGB channels.....96

Table 4-5. The percentage errors of simulation for remain data sets after kicking-away game.....96

Table 4-6. Mean linearized digit values of the kicked-away data sets.....97

Table 4-7. Color differences of calibration in simulation using 3 basis functions with different transform matrices.....98

Table 4-8. Color differences of calibration in simulation using 3 basis functions with different transform matrices, based on good data sets from 10% error criterion.....99

Table 4-9. Color differences of calibration in simulation using 3 basis

functions with different transform matrices, based on good data sets from 20% error criterion.....99

Table 4-10. Color differences of calibration in simulation using 6 basis functions with different transform matrices.....100

Table 4-11. Color differences of calibration in simulation using 6 basis functions with different transform matrices, based on good data sets from 10% error criterion 100

Table 4-12. Color differences of calibration for imaging system using 3 basis functions, 441 data sets, and with different transform matrices.....101

Table 4-13. Color differences of calibration for imaging system using 3 basis functions, remained data sets using 10% criterion, and with different transform matrices.....102

Table 4-14. Color differences of calibration for imaging system using 3 basis functions, remained data sets using 20% criterion, and with different transform matrices.....102

Table 4-15. Color differences of calibration for imaging system using 6 basis functions, 441 data sets, and with different transform matrices.....102

Table 4-16. Color differences of calibration for imaging system using 6 basis functions, remained data sets using 10% criterion, and with different transform matrices.....103

Table 4-17. Cumulative contribution percentage of principal components calculated from spectra of all race with different wavelength steps.....106

Table 4-18. Color differences of face spectral reproduction based on 3 and 6 basis functions using different wavelength steps.....106

Table 4-19. Color differences between measured face spectra with 2nm step and estimated spectral based on 3 and 6 basis functions using different wavelength steps.....107

Table 4-20. Color differences between the simulated and measured 441 sets of face spectra that using the same wavelength steps.....108

Table 4-21. Color differences between the 441 measured face spectra using 2nm step and the corresponding simulated spectra using different wavelength steps.....109

Table 4-22. Color differences between all 550 sets of measured spectra using 2nm step and the corresponding simulated spectra using different wavelength steps.....110

Table 4-23. Cumulative contribution percentage of principal components calculated from Vrhel's spectra with different wavelength steps.....113

Table 4-24. Color differences of spectral reproduction for Vrhel's spectra based on 3, 6, and 9 basis functions using different wavelength steps.....114

Table 4-25. Color differences between original Vrhel's spectra with 2nm step and estimated spectra based on 3, 6, and 9 basis functions using different wavelength steps.....115

Table 4-26. Color differences between the simulated and Measured Vrhel's spectra that using the same wavelength steps.....116

Table 4-27. Color differences between measured Vrhel's spectra using 2nm step and the corresponding simulated spectra using different wavelength steps.....117

Table 4-28. Color differences between measured spectra of GretagMacbeth Color Checkers using 2nm step and the corresponding simulated spectra using different wavelength steps.....117

Table 4-29. Measured tristimulus values for display white, black, and peak RGB primaries.....124

Table 4-30. Measured tristimulus values for display white point and the sum of peak RGB primaries.....124

Table 4-31. Color differences in LCD characterization for forward path.....128

Table 4-32. Color differences in LCD characterization for loop path.....128

Table 4-33. Color differences in LCD characterization for forward path after optimization.....129

Table 4-34. Color differences in LCD characterization for loop path after Optimization.....129

Table 4-35. Covariance matrix of distortion factors.....157

Table 4-36. Cumulative contribution percentage of principal components for distortion actors.....158

Table 4-37. Correlations between distortion factors and their principal components.....158

Table 4-38. Coefficients s_{ji} for Eq. 4-33.....161

Table 4-39. Coefficients t_{ji} for Eq. 4-34.....162

Table 4-40. Correlation coefficients between PQS and MOS, and PQS_d and MOS...169

1 INTRODUCTION

This dissertation addresses the problem of capturing spectral images of human portraits and evaluating image quality of spectral imaging systems. Most of the traditional color-imaging and reproduction systems have been designed in a trichromatic fashion with three response functions, resulting in three color signals, i.e., RGB color values. These approaches can reproduce color quite capably. However, there are several problems inherent in these approaches, which will cause large color shifts. This becomes apparent in the image capture and reproduction of metameric objects[1]. The only way to solve these problems is to attempt to produce spectral matches between the original objects and their reproductions. The key idea is to replace the world of red, green and blue with the world of wavelength.[2] This dissertation research is concentrated on the spectral imaging of human portraits and corresponding image quality.

Facial color reproduction is an important aspect of color-imaging system design and analysis. Visible spectral images of human portraits are desired to test color imaging system design via computer simulation. The study of spectral imaging of human portraits in this dissertation is motivated in part by the previous multi-spectral image research of artwork[3, 4, 5, 6, 7] and realistic spectral image synthesis[1] in the Munsell Color Science Laboratory, and spectral skin color image research by Imai et al.[8] They provided formulations and methods involving spectral imaging system and spectral image capture. They also provided detail studies of spectral image application in human skin and computer graphics. However, a high quality spectral human portrait needs some specific considering of its own. Some previous spectral portrait image research[8] performed the

system calibration based on the painting samples which were the reproductions of the reflectance spectra of skin directly measured. These approaches required very accurate reproductions of skin at a fairly early stage to avoid propagating errors through all the following procedures. Moreover, those reproduced spectral paintings excluded the spectra of the lips, eyes and hair which are important parts of the human portrait information. These paintings also could not contain the geometric spectral information related to the specific subjects under specific lighting conditions. Experience in spectral image experiments also indicates that calibrated systems based only on the standard color checkers will not represent the spectra of human portrait with enough accurate. This dissertation includes efforts to calibrate the imaging system and capture spectral images of human portraits based on the spectral data directly recorded from human subjects with certain lighting conditions. The calibrated imaging system included the ability to represent not only the facial skin but also the spectra of lips, eyes and hair as well. The generated spectral images can be applied to color-imaging system design and analysis.

As the applications of spectral images become increasingly popular in recent years, image quality studies in this field have been of greater practical interest.[9,10,11,12] However, little has been studied on the evaluation of overall quality of spectral images obtained by digital spectral imaging systems. Typically, when designing a wide-band visible spectral imaging system, it is important to select a proper number of channels to capture the images. During processing stage, while applying principal components analysis (PCA) method, it is important to select the proper number of eigenvectors and transform matrix to construct the spectral images. Often, one needs to balance the accuracy of spectral

information and noise tolerance of the spectral images. Based on PCA method, more channels or more eigenvectors used will provide more accuracy of reconstructed spectral information. However, on the other hand, more channels or more eigenvectors used will yield more noise in the reconstructed spectral images.[10] Other issues, like the stability of transform matrix and the selection of objective function in imaging system optimization, will also affect the final spectral images. Image quality study for spectral imaging, therefore, is worth doing. This dissertation includes visual psychophysical experimental evaluation for spectral images. The spectral images were simulated using different imaging system settings. To bridge the gap between the physical measures and subjective visual perceptions of image quality, effort had been made to build the image quality metrics. Four distortion factors were defined to describe the impairment of image quality. Image quality metrics would be determined from the principal components analysis for distortion factors and multiple regression analysis. The importance of contribution from distortion factors was evaluated based on statistical analysis. Statistical analysis of image quality metrics was also performed.

As an extension of the work other researchers in MCSL have initiated, this dissertation research has, working with other researchers in MCSL, put effort to build a publicly accessible database of spectral images, Lippmann2000.

The following chapters first provide some background review in spectral imaging and image quality. Then details of spectral imaging system design for spectral imaging of human portraits are demonstrated. Statistical analysis of human facial spectra is provided and the estimated spectral images for rendering are given. To study further the spectral

imaging system, image quality analysis for the spectral imaging systems was then performed. Spectral imaging systems were simulated using different system settings. A visual image quality assessment experiment was carried out and subjective image quality scores were obtained. Four distortion factors were defined and computed. The results of the visual quality experiment and corresponding distortion factor measures were thoroughly investigated. Finally, image quality metrics are proposed to relate the subjective image quality assessment and objective distortion measures. Details of statistical analysis for image quality metrics and distortion factors are provided. Some suggestion to improve the spectral imaging system design is also provided. Further interesting issues and research directions in spectral imaging system and image quality are recommended and discussed.

2. BACKGROUND LITERATURE REVIEW

2.1 Spectral Characterization of Human Face

The color, or spectra of human subjects depends chiefly on the presence of pigment and blood.[13, 14] Different races and localizations of human beings have different spectral characteristics though the pigments involved are the same.

2.1.1 Spectral Characterization of Skin

Much research has been done on color of human beings, especially human skin. Biological and anatomical research indicates that the skin is made up of three layers, epidermis, dermis and hypodermis. Dealing with the color, we simply divide the skin into an outer thin layer, epidermis, and an inner, relatively thick layer, dermis as shown in Fig. 2-1.

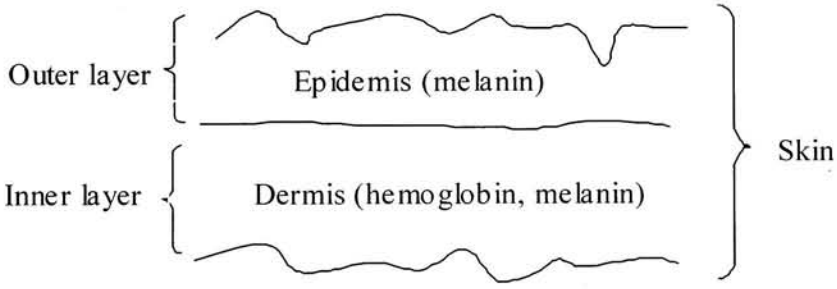

***Figure 2-1**. Scheme picture of human skin*

For normal human skin, the absorption of the epidermis is dominated by a black pigment called melanin though there are five different pigments in the skin.[15] The spectral characteristics of different races or different individuals are due only to variation in the amount of melanin present.[16, 17] People with dark brown or black skin have many melanin particles; people with medium to light brown skin have fewer; people with very

light brown to white skin have only a very few. Buck and Grum,[18] and Kollias and Baqer[17] performed experiments to measure the spectral characteristics of human melanin by measuring spectra of normal skin and vitiligo-involved skin of volunteers-patients. Their research indicated that the spectral reflectance of melanin in the visible range is monotonically increasing. The inner layer, dermis, is rich with blood vessels which contain hemoglobin. Hemoglobin has marked absorption bands around 575nm, 540nm and 410nm.[19, 20] Brumsting and Sheard[13, 14] indicated that the marked absorption bands of hemoglobin occur only when it bounds with oxygen within vivo skin. Those measured spectra are shown in Fig. 2-2. Heavily pigmented skin will present less pronounced effect of the hemoglobin absorption bands because of the masking effect of the greater amount of melanin pigmentation. Skin optics[21] further showed that the epidermis is a strongly forward scattering layer and, for all wavelengths considered, scattering is much more important than absorption. Details of skin biology are beyond the scope of this research.

2.1.2 Spectral Characterization of Eyes, Hair and Lips

The skin is not the only part of the human body that differs in color from one individual to another. The eyes and hair have the same elements affecting their coloring. In the eye, as in the skin, melanin is the dominant pigment material. However, in this case, the location of the melanin is as important as the amount. Research[15] indicated that, in brown and black eyes, there is melanin on the inside of the white and iris, and on the front of the iris as well. In blue eyes, the melanin is found only on the inside. While the white of the eye is opaque and lets no light pass at all, the colorless tissue of the iris does let some

light pass through. They scatter and change the colors in much the same way as the

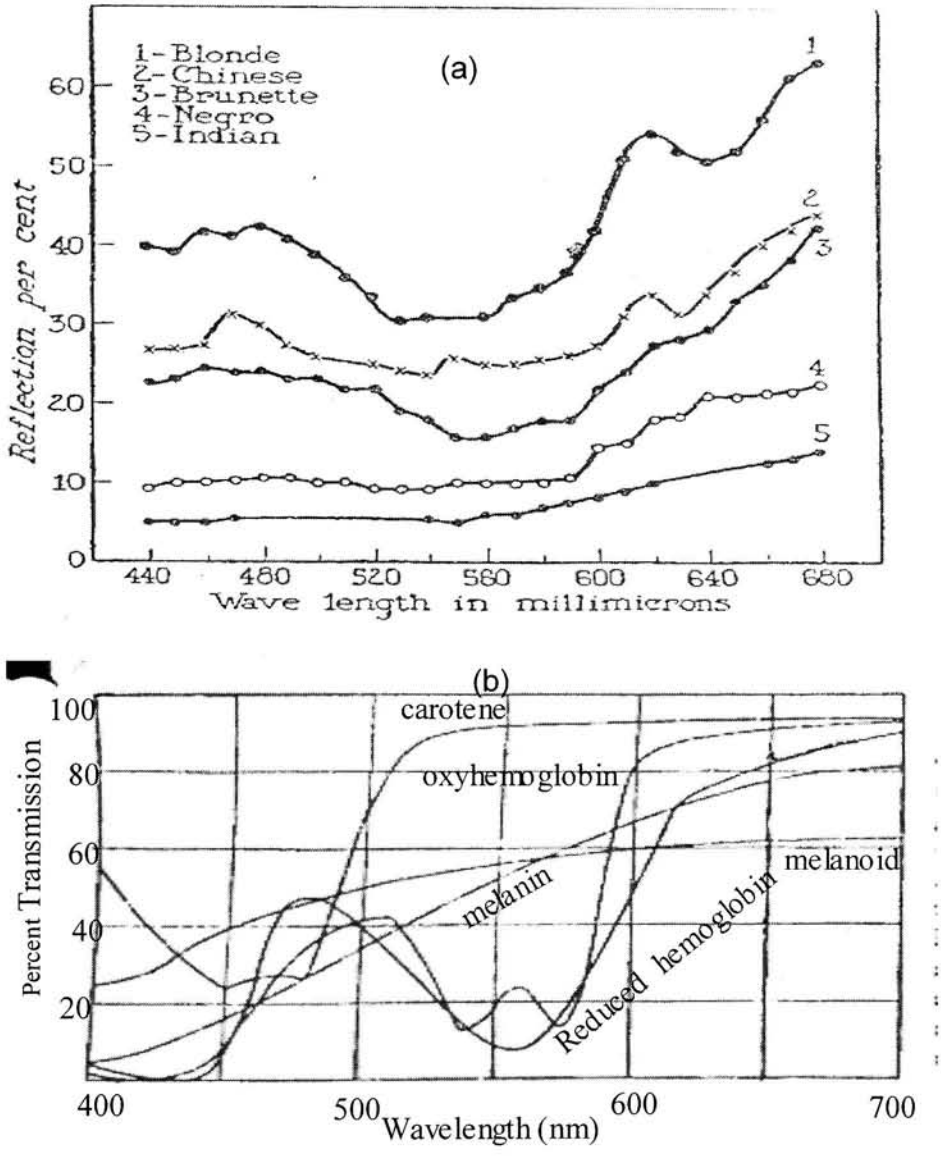

Figure 2-2. *Measured spectral data of human skin in early research. (a). mean spectral reflectances of human skin from various races (copied from Brunsting & Sheard's work,[13] 1929); (b). spectral transmittance for hemologlobin and melanin (copied from Buck's work,[19] 1948).*

colorless upper skin layers do. Therefore, like the sky looks blue because the atmosphere scatters the light passing through it, the iris appears blue rather than brown or black when the eyes have melanin only on the inside.

As similar in the skin and eyes, melanin, eumelanin (brown-black) and phaemelanin (yellow-red) in the hair sometimes has a red-gold pigment as well.[15] Hair contains a center section, a middle area and a scaly outer skin. When there are only a few melanin particles in the middle area, the colorless outer skin softens the brownish-black color of the melanin so much that the hair appears blond. When both the middle area and the center section of each hair are rich with melanin, the hair appears brown. And when the center section is packed with melanin the hair is black. Hair become white or gray when there is not any melanin at all or little melanin in the center or middle sections.

Human lips are rich with blood vessels. Therefore, the spectral properties of human lips are very close to that of hemoglobin with marked absorption bands around 575nm, 540nm and 410nm.

2.2 Spectral Imaging

Most of the traditional color-imaging and reproduction systems functioned in a trichromatic fashion with three response functions, resulting in three color signals, i.e., RGB color values. Because of the problems involved in the image capture and reproduction of metameric objects, spectral matches between the original objects and their reproductions are attracting the attention of many researchers in recent years.[1-7] Therefore, instead of providing RGB color values in traditional color images, each pixel

of the spectral images will provide the spectral reflectance information at that pixel. This dissertation concentrates on the spectral imaging system using wide-band method in the visible range.

2.2.1 Spectral Image and Spectral Imaging System

Multi-spectral image acquisition can be modeled using matrix-vector notation.[9] The illumination spectral power distribution can be expressed as in Eq. 2-1:

$$\mathbf{S} = \begin{bmatrix} s_1 & & & 0 \\ & s_2 & & \\ & & \ddots & \\ 0 & & & s_n \end{bmatrix}, \qquad (2-1)$$

where the index indicates the set of n wavelengths over the visible range. The object spectral reflectance can be expressed as $\mathbf{r} = [r_1, r_2, ..., r_n]^T$ where T means matrix transpose. The transmittance characteristics of the m filters will be given in the following form in Eq. 2-2 where $f_{i,j}$ represents the transmittance of jth filter in the wavelength of i:

$$\mathbf{F} = \begin{bmatrix} f_{1,1} & f_{1,2} & \cdots & f_{1,m} \\ \vdots & \vdots & \cdots & \vdots \\ f_{n,1} & f_{n,2} & \cdots & f_{n,m} \end{bmatrix}. \qquad (2-2)$$

The spectral sensitivity of the detector, i.e., CCD digital camera, will be given in Eq. 2-3 where the index indicates the set of n wavelengths over the visible range:

$$\mathbf{D} = \begin{bmatrix} d_1 & & & 0 \\ & d_2 & & \\ & & \ddots & \\ 0 & & & d_n \end{bmatrix}. \qquad (2-3)$$

Then the captured image is given in Eq. 2-4.

$$\mathbf{I} = (\mathbf{D} \cdot \mathbf{F})^T \cdot \mathbf{S} \cdot \mathbf{r} = \begin{bmatrix} \sum_{l=1}^{n} f_{l,1} \cdot d_l \cdot s_l \cdot r_l \\ \sum_{l=1}^{n} f_{l,2} \cdot d_l \cdot s_l \cdot r_l \\ \vdots \\ \sum_{l=1}^{n} f_{l,m} \cdot d_l \cdot s_l \cdot r_l \end{bmatrix}, \qquad (2-4)$$

where **I** is the digital counts of the pixel. The spectral reflectance of each pixel, theoretically, can be obtained using pseudoinverse from Eq.(2-4). However, in most cases, there are fewer digital counts than wavelengths for each pixel, the spectral reflectance obtained using pseudoinverse method here may yield large uncertainty and give large error. The advantage here is convenient to do simulation and check the results.[6] Therefore, PCA method will be performed as an alternative choice. This is discussed in detail below. The color vector can be obtained as $\mathbf{C} = \mathbf{A} \cdot \mathbf{I} = (X,Y,Z)^T$ where X, Y, Z are the CIE tristimulus values and A is a transfer matrix. The CIELAB L*, a*, b* are given by the non-linear transformation Ψ, where $\Psi(X,Y,Z) = L^*, a^*, b^*$.

The spectral reflectance R(x, y, λ), where x, y denote the spatial coordinates of the image pixel, can be estimated using spectral reconstruction methods based on statistical analyses, PCA. It can also be obtained by using interpolation techniques such as cubic spline done by Burns.[9] Burns and Berns[3] indicated that the method of PCA would give more accurate results than interpolation methods.

2.2.2 Spectral Imaging for Human Portraiture

Facial color reproduction is an important aspect of color-imaging system design and analysis. Visible spectral images of human portraits are desired to test color imaging system design via computer simulation. Previous research,[22, 23] based on 108 reflectance spectra of skin in faces of 54 Japanese women, showed that the spectral reflectances of human skin, can be represented by three basis functions using PCA. Therefore, the spectral reflectance of each pixel of the captured image could be estimated from the values of three color channels and the spectral radiance of the illuminant used. These experiments showed very successful results. However, the spectral reflectance database employed in these experiments was concentrated on a single race and only on skin. The spectral measurement geometry is generally fixed to 45/0 or d/0. Considering the capability of spectral imaging systems for different races of human portraits it seems worth including spectral reflectances of different races and those spectral data should include skin, hair, eyes and lips as well. Therefore, the number of basis functions used for this research need to be re-determined. Since the human face is not a planar but a 3-dimensional object, the spectra of the subjects observed by the camera could vary with any geometry. In other words, to perform an accurate calibration of the spectral imaging

system, the spectral database should be with large gamut including various geometric configurations. In addition, previous spectral portrait image researches performed the system calibration based on the painting samples which were the reproductions of the measured spectral reflectance of skin. Those paint samples were not available for us. Moreover, these approaches required very accurate reproductions of skin at a fairly early stage to avoid the errors passed through all the following procedures. Other researchers, such as Tominaga[24] calibrated their system and determined basis functions based on Munsell chips, paint chips and natural objects. We consider those methods could neither provide sufficient geometric information of the real spectral reflectances of the face nor represent them precisely. According to these considerations, therefore, we proposed a new procedure and designed a new spectral imaging system for human portraiture that has the capability to capture spectral images of various races and describe spectral reflectances of skin, hair, eyes and lips very well. This imaging system would perform system calibration and capture spectral images based on the spectral data directly recorded from the real human subjects with certain lighting and camera conditions. The spectral reflectances measured above will be analyzed by PCA. Based on the results of PCA, both three-wide-band and six-wide-band spectral images will be estimated respectively.

2.2.3 Principal Components Analysis

The PCA method is a mathematical technique that describes a multivariate set of measured data using basis functions, or called eigenvectors. The basis functions are formulated using specific linear combinations of the original variables. The basis

functions are uncorrelated and are computed in decreasing order of importance; the first function accounts for as much as possible of the variation in the original data, the second function accounts for the second largest portion of the variation in the original data, and so on. The PCA method attempts to construct a small set of basis functions that summarize the original data, thereby reducing the dimensionality of the original data. In practice, though the accuracy of spectral reconstruction depends on the number of basis functions used, 5 to 8 basis functions are sufficient for accurate spectral reconstruction used in artwork,[6, 9, 25, 26] while 3 basis functions are satisfied in spectral reproduction of human skin.[8] Details of the PCA can be found in many textbooks.[27, 28]

Applying the PCA method to the measured spectral reflectance of the objects, the number of basis functions for accurate spectral reproduction can be determined based on the cumulative proportion rates of the basis functions. Suppose six basis functions are sufficient to represent the spectral reflectance of human face, including skin, hairs, eyes and lips. The spectral reflectance of human face can then be expressed as a linear combination of the basis functions as in Eq. 2-5.

$$\mathbf{r} = \bar{\mathbf{r}} + \sum_{i=1}^{6} \alpha_i \cdot \mathbf{u}_i = \bar{\mathbf{r}} + (\mathbf{u}_1\, \mathbf{u}_2\, \mathbf{u}_3\, \mathbf{u}_4\, \mathbf{u}_5\, \mathbf{u}_6) \begin{pmatrix} \alpha_1 \\ \alpha_2 \\ \alpha_3 \\ \alpha_4 \\ \alpha_5 \\ \alpha_6 \end{pmatrix}, \qquad (2-5)$$

where $\bar{\mathbf{r}}$ is the average spectral reflectance, $\mathbf{u}_i$ are the basis functions, or eigenvectors, and α_i are the eigenvalues. The tristimulus values X, Y, Z can be calculated by Eq. 2-6:

$$
\begin{aligned}
X &= K \cdot \sum_{\lambda=380}^{780} E(\lambda) \cdot \overline{x(\lambda)} \cdot r(\lambda), \\
Y &= K \cdot \sum_{\lambda=380}^{780} E(\lambda) \cdot \overline{y(\lambda)} \cdot r(\lambda), \\
Z &= K \cdot \sum_{\lambda=380}^{780} E(\lambda) \cdot \overline{z(\lambda)} \cdot r(\lambda),
\end{aligned}
\tag{2-6}
$$

where r(λ) is the spectral reflectance, E(λ) is the spectral radiance of the illumination, $\overline{x(\lambda)}$, $\overline{y(\lambda)}$, $\overline{z(\lambda)}$ are the color matching functions, and K is a normalized constant. Eq.(6) can be converted to matrix notation as shown in Eq. 2-7:

$$
\begin{aligned}
X &= K\mathbf{e}^T \bar{\mathbf{x}}\mathbf{r}, \\
Y &= K\mathbf{e}^T \bar{\mathbf{y}}\mathbf{r}, \\
Z &= K\mathbf{e}^T \bar{\mathbf{z}}\mathbf{r},
\end{aligned}
\tag{2-7}
$$

where T represent the transpose, the matrix **e** and **r** are matrix notations of E(λ) and r(λ) respectively. And the matrices $\bar{\mathbf{x}}, \bar{\mathbf{y}}, \bar{\mathbf{z}}$ are color-matching function represented as follows:

$$
\bar{\mathbf{x}} = \begin{bmatrix} \overline{x_1} & & 0 \\ & \overline{x_2} & \\ & \ddots & \\ 0 & & \overline{x_n} \end{bmatrix}, \tag{2-8}
$$

$$
\bar{\mathbf{y}} = \begin{bmatrix} \overline{y_1} & & 0 \\ & \overline{y_2} & \\ & \ddots & \\ 0 & & \overline{y_n} \end{bmatrix}, \tag{2-9}
$$

$$
\bar{\mathbf{z}} = \begin{bmatrix} \overline{z_1} & & 0 \\ & \overline{z_2} & \\ & \ddots & \\ 0 & & \overline{z_n} \end{bmatrix}. \tag{2-10}
$$

From Eqs. 2-5 and 2-7 can then be written as

$$X = K\mathbf{e}^T \bar{\mathbf{x}} \left[\bar{\mathbf{r}} + (\mathbf{u}_1\ \mathbf{u}_2\ \mathbf{u}_3\ \mathbf{u}_4\ \mathbf{u}_5\ \mathbf{u}_6) \begin{pmatrix} \alpha_1 \\ \alpha_2 \\ \alpha_3 \\ \alpha_4 \\ \alpha_5 \\ \alpha_6 \end{pmatrix} \right], \qquad (2-11)$$

$$Y = K\mathbf{e}^T \bar{\mathbf{y}} \left[\bar{\mathbf{r}} + (\mathbf{u}_1\ \mathbf{u}_2\ \mathbf{u}_3\ \mathbf{u}_4\ \mathbf{u}_5\ \mathbf{u}_6) \begin{pmatrix} \alpha_1 \\ \alpha_2 \\ \alpha_3 \\ \alpha_4 \\ \alpha_5 \\ \alpha_6 \end{pmatrix} \right], \qquad (2-12)$$

$$Z = K\mathbf{e}^T \bar{\mathbf{z}} \left[\bar{\mathbf{r}} + (\mathbf{u}_1\ \mathbf{u}_2\ \mathbf{u}_3\ \mathbf{u}_4\ \mathbf{u}_5\ \mathbf{u}_6) \begin{pmatrix} \alpha_1 \\ \alpha_2 \\ \alpha_3 \\ \alpha_4 \\ \alpha_5 \\ \alpha_6 \end{pmatrix} \right], \qquad (2-13)$$

Eqs. 2-11 ~2-13 then can be rewritten as follows:

$$X = K\mathbf{e}^T \bar{\mathbf{x}}\bar{\mathbf{r}} + K\mathbf{e}^T (\bar{\mathbf{x}}\mathbf{u}_1\ \bar{\mathbf{x}}\mathbf{u}_2\ \bar{\mathbf{x}}\mathbf{u}_3\ \bar{\mathbf{x}}\mathbf{u}_4\ \bar{\mathbf{x}}\mathbf{u}_5\ \bar{\mathbf{x}}\mathbf{u}_6) \begin{pmatrix} \alpha_1 \\ \alpha_2 \\ \alpha_3 \\ \alpha_4 \\ \alpha_5 \\ \alpha_6 \end{pmatrix}, \qquad (2-14)$$

$$Y = K\mathbf{e}^T \bar{\mathbf{y}}\bar{\mathbf{r}} + K\mathbf{e}^T (\bar{\mathbf{yu}}_1\ \bar{\mathbf{yu}}_2\ \bar{\mathbf{yu}}_3\ \bar{\mathbf{yu}}_4\ \bar{\mathbf{yu}}_5\ \bar{\mathbf{yu}}_6) \begin{pmatrix} \alpha_1 \\ \alpha_2 \\ \alpha_3 \\ \alpha_4 \\ \alpha_5 \\ \alpha_6 \end{pmatrix}, \qquad (2-15)$$

$$Z = K\mathbf{e}^T \bar{\mathbf{z}}\bar{\mathbf{r}} + K\mathbf{e}^T (\bar{\mathbf{zu}}_1\ \bar{\mathbf{zu}}_2\ \bar{\mathbf{zu}}_3\ \bar{\mathbf{zu}}_4\ \bar{\mathbf{zu}}_5\ \bar{\mathbf{zu}}_6) \begin{pmatrix} \alpha_1 \\ \alpha_2 \\ \alpha_3 \\ \alpha_4 \\ \alpha_5 \\ \alpha_6 \end{pmatrix}. \qquad (2-16)$$

The first terms of Eqs. 2-14 ~ 2-16 can be treated as the contribution of the averaged spectral reflectance to the tristimulus values, and the second terms as the contribution of six basis functions or eigenvectors. Therefore, we have the following equation:

$$\begin{bmatrix} X \\ Y \\ Z \end{bmatrix} = \begin{bmatrix} \bar{X} \\ \bar{Y} \\ \bar{Z} \end{bmatrix} + \begin{bmatrix} X_1 & X_2 & X_3 & X_4 & X_5 & X_6 \\ Y_1 & Y_2 & Y_3 & Y_4 & Y_5 & Y_6 \\ Z_1 & Z_2 & Z_3 & Z_4 & Z_5 & Z_6 \end{bmatrix} \begin{bmatrix} \alpha_1 \\ \alpha_2 \\ \alpha_3 \\ \alpha_4 \\ \alpha_5 \\ \alpha_6 \end{bmatrix}, \qquad (2-17)$$

where $\bar{X}, \bar{Y}, \bar{Z}$ are the averaged tristimulus values and X_i, Y_i, Z_i(i = 1,2,...,6) are the tristimulus values corresponding to the six basis functions of spectral reflectance of human face. However, to determine the six eigenvalues, three more equations need to be provided. Therefore, a filter is employed, either in front of the lighting source or detector, to yield another three equations given in Eq. 2-18:

$$
\begin{aligned}
X_f &= K \cdot \sum_{\lambda=380}^{780} E(\lambda) \cdot \overline{x(\lambda)} \cdot T(\lambda) \cdot r(\lambda), \\
Y_f &= K \cdot \sum_{\lambda=380}^{780} E(\lambda) \cdot \overline{y(\lambda)} \cdot T(\lambda) \cdot r(\lambda), \\
Z_f &= K \cdot \sum_{\lambda=380}^{780} E(\lambda) \cdot \overline{z(\lambda)} \cdot T(\lambda) \cdot r(\lambda),
\end{aligned}
\qquad (2-18)
$$

where $T(\lambda)$ is spectral transmittance of the filter, X_f, Y_f, and Z_f are corresponding tristimulus values. Using the similar procedure as above, we can derive the final equations with matrix form as given in Eq. 2-19:

$$
\begin{bmatrix} X_f \\ Y_f \\ Z_f \end{bmatrix} = \begin{bmatrix} \overline{X_f} \\ \overline{Y_f} \\ \overline{Z_f} \end{bmatrix} + \begin{bmatrix} X_{f1} & X_{f2} & X_{f3} & X_{f4} & X_{f5} & X_{f6} \\ Y_{f1} & Y_{f2} & Y_{f3} & Y_{f4} & Y_{f5} & Y_{f6} \\ Z_{f1} & Z_{f2} & Z_{f3} & Z_{f4} & Z_{f5} & Z_{f6} \end{bmatrix} \begin{bmatrix} \alpha_1 \\ \alpha_2 \\ \alpha_3 \\ \alpha_4 \\ \alpha_5 \\ \alpha_6 \end{bmatrix}. \qquad (2-19)
$$

Combining Eqs. (17) and Eqs. (19), we have six independent equations with six unknown eigenvalues. The matrix form of these six equations is shown in Eq. 2-20:

$$
\begin{bmatrix} X \\ Y \\ Z \\ X_f \\ Y_f \\ Z_f \end{bmatrix} = \begin{bmatrix} \overline{X} \\ \overline{Y} \\ \overline{Z} \\ \overline{X_f} \\ \overline{Y_f} \\ \overline{Z_f} \end{bmatrix} + \begin{bmatrix} X_1 & X_2 & X_3 & X_4 & X_5 & X_6 \\ Y_1 & Y_2 & Y_3 & Y_4 & Y_5 & Y_6 \\ Z_1 & Z_2 & Z_3 & Z_4 & Z_5 & Z_6 \\ X_{f1} & X_{f2} & X_{f3} & X_{f4} & X_{f5} & X_{f6} \\ Y_{f1} & Y_{f2} & Y_{f3} & Y_{f4} & Y_{f5} & Y_{f6} \\ Z_{f1} & Z_{f2} & Z_{f3} & Z_{f4} & Z_{f5} & Z_{f6} \end{bmatrix} \cdot \begin{bmatrix} \alpha_1 \\ \alpha_2 \\ \alpha_3 \\ \alpha_4 \\ \alpha_5 \\ \alpha_6 \end{bmatrix}. \qquad (2-20)
$$

The eigenvalues are then given by using Eq. 2-21. After determine the six eigenvalues, the spectral reflectance of human face can be obtained by basis functions using Eq. 2-5.

$$\begin{bmatrix} \alpha_1 \\ \alpha_2 \\ \alpha_3 \\ \alpha_4 \\ \alpha_5 \\ \alpha_6 \end{bmatrix} = \begin{bmatrix} X_1 & X_2 & X_3 & X_4 & X_5 & X_6 \\ Y_1 & Y_2 & Y_3 & Y_4 & Y_5 & Y_6 \\ Z_1 & Z_2 & Z_3 & Z_4 & Z_5 & Z_6 \\ X_{f1} & X_{f2} & X_{f3} & X_{f4} & X_{f5} & X_{f6} \\ Y_{f1} & Y_{f2} & Y_{f3} & Y_{f4} & Y_{f5} & Y_{f6} \\ Z_{f1} & Z_{f2} & Z_{f3} & Z_{f4} & Z_{f5} & Z_{f6} \end{bmatrix}^{-1} \cdot \left[\begin{bmatrix} X \\ Y \\ Z \\ X_f \\ Y_f \\ Z_f \end{bmatrix} - \begin{bmatrix} \overline{X} \\ \overline{Y} \\ \overline{Z} \\ \overline{X_f} \\ \overline{Y_f} \\ \overline{Z_f} \end{bmatrix} \right]. \qquad (2-21)$$

2.3 Image quality for Spectral Imaging

Many factors will impact the spectral or color accuracy of spectral images. In the capturing stage, noise in the CCD sensors is a big factor to image quality.[9, 10] Burns and Berns[9, 10, 29] indicated that noise error in CCD will propagate through image transformation and cause the color shift in the final spectral images. The selection of wide-band or narrow band,[30] selection of filters[31] and number of channels[9] will also contribute to the image quality or color and spectral accuracy of reproduced spectral images. During construction stage, many transform matrices need to be optimized and other algorithms need to be applied to estimate the spectra. The selection of those optimization objects will also impact the accuracy the spectral reproduction.[32] Imai[32] compared various metrics that had been used for spectral matches. These metrics can be categorized in three classes: CIE color difference equations, spectral curves difference metrics and metamerism indices. Hill[33] proposed a observer matched basis functions method to control the channels of multi-channel display to reproduce colors at least error for every human observer and obtained very impressive results. Overall, most previous

research concentrated on the accuracy of spectral or color reproduction of spectral images. Only a little has been studied on the evaluation of overall image quality of spectral images obtained by digital spectral imaging systems. Thus, the study of image quality of spectral imaging system will guide us toward a more efficient and correct way to optimize our design for spectral imaging systems.

Image quality (IQ) is the integrated set of perceptions of the overall degree of excellence of the image.[34] IQ evaluation is usually divided into two classes, subjective measure and quantitative objective measure.

2.3.1 Subjective Measure

Subjective IQ is evaluated through visual assessment by human observers. Since the purpose of the most imaging system is to generate images from which human observers can extract relevant information, it is necessary to take into account the judgment of the human observer, subjective assessment. However, subjective assessments of quality are experimentally difficult and lengthy, and the results obtained may suffer from variability due to observers and to the test conditions.[35, 36] Therefore, from some point of view, subjective IQ is often regarded as inferior measurement method compared to objective IQ methods. [34]

2.3.2 Quantitative Objective Measure

Objective measures of IQ would not only overcome the difficulties suffered by subjective assessments, but also would produce repeatable results and reflect the perceptions of IQ. Further, the objective measures would provide constructive methods to improve the design process of imaging system. [37] However, as mentioned above, by some definition at

least, human observers are the final judges of image quality. The objective measure of IQ, therefore, should correlate as well as possible, with the human IQ assessment.

2.3.3 Image Quality in Spectral Imaging

Though people paid much attention to the spectral and color accuracy when designing a spectral imaging system, little has been reported in the field of overall image quality in spectral imaging system. Theoretically, perfect spectral match will guarantee perfect color match between an object and its reproduction. In practice, however, it is impossible to build a spectral imaging system that can reproduce any spectra perfectly well. Therefore, often, when designing a spectral imaging system, one has to balance among the accuracy of spectral information, noise tolerance and accuracy of color reproduction of the spectral images.[9] When building algorithms to estimate the spectra, there are many criteria to choose based on different practice needs. It is well known that minimizing spectral error does not guarantee most accurate color reproduction, except then spectral error is zero. Even considering the spectral error itself, there are many criteria to describe, such as root mean square (RMS) error, correlation coefficient and etc. Researchers did lot of work on this issue.[32, 33, 38] There are also many other issues involved in estimating the spectra in spectral imaging as mentioned in the introduction chapter. Conclusively, researchers mostly concentrated on the balance between the accuracies of spectral and color reproductions. Since the final product is the image, either black-white or color, it is reasonable and worth considering how these above issues will impact the quality of the final image. Results should provide us a helpful guide for designing a spectral imaging

system. Much previous research on the IQ of digital imaging system can provide some good suggestions to deal with the IQ in spectral imaging system.

During the past decade many kinds of digital devices such as digital cameras and digital scanners have been developed and widely used for color image recording instead of traditional analog photography. To study the potential capabilities of digital imaging systems, researchers have proposed many image quality models. [36, 38, 39, 40, 41, 42, 43, 44] Some of them connect technology variables with customer quality preferences, others connect physical image parameters with user quality preference.

2.3.4 Objective Picture Quality Scale (PQS) Method

Among those IQ models, Miyahara's [44] objective Picture Quality Scale (PQS) method is very impressive. It was originally proposed for quality estimation of monochromatic image coding. This method is based on classifying and quantifying actual distortions produced by coders and defining a set of partial distortion measures. The block diagram of PQS method is shown in Fig. 2-3. The approach is based on the perceptual properties of human vision. First the image signal is transformed into one that is proportional to the visual perception of luminance using the Weber-Fechner's law and then the frequency weighted errors are obtained. Second, perceived image disturbances are described and the corresponding objective distortion factors that quantify each image degradation are obtained. Five distortion factors are defined that two of them are for random errors, one for blocking and the rest two are for correlated errors. Third, the mean opinion score (MOS) is determined from visual assessment scale experiment of encoded images. Fourth, principal component analysis is carried out to quantify the correlation

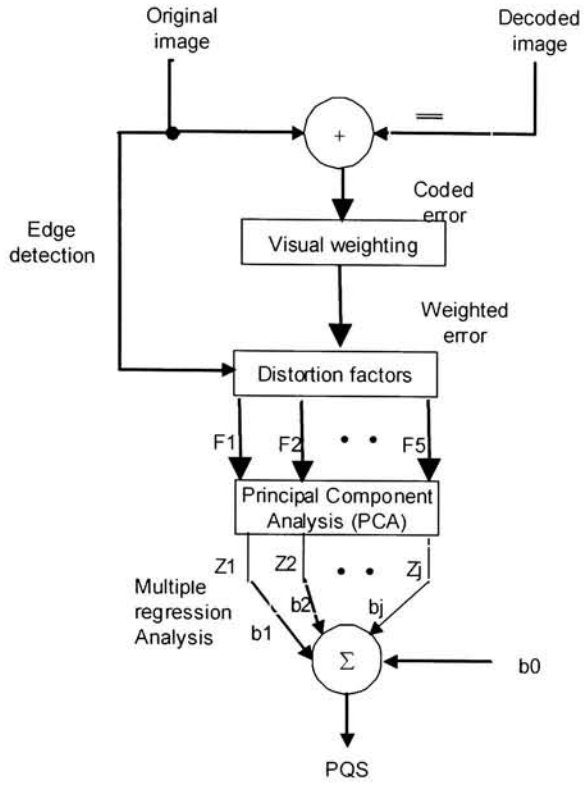

***Figure 2-3**. Conventional PQS system*

between distortion factors. Finally, a multiple regression analysis is carried out between the principal component vectors and the measured MOS values, hence, determining the PQS. Therefore, the obtained quality metric, PQS, will have very good correlation with the subjective measure, MOS. The concept of PQS method was followed in this research, not the step-by-step details. Distortion factors in our research need to be redefined. For instance, error yielded from wavelength step selection, random noise in illumination and CCD camera, could be important in measure of spectral image quality. Also, measures of color difference of color image should be involved and treated as a distortion factor. The task is definitely very challenging since a wide range of spectral image sources and their

corresponding specific algorithms are involved. Our interest was narrowed to some specific issues discussed below.

2.3.5 Color Difference and Color Appearance Models

In color reproduction, it is important to specify how accurately a color must be reproduced. Therefore, it is necessary to have an objective measurement for color differences. Such measurements are required to set and maintain color tolerances for production and sale of all colored materials.[47] There are several metrics of color difference widely applied in a variety of industries, such as CIELAB ΔE^*_{ab} , CIE ΔE^*_{94}[47] and, more recently, CIEDE2000.[48] It should be emphasized here that those metrics were designed for predicting the visual color difference of large isolated patches.

Color appearance models extend the current systems to allow the description of what color stimuli look like under a variety of viewing conditions.[47] Most of the effort in the formulation of color appearance models has been concentrated on the area of chromatic-adaptation transforms. Chromatic adaptation is the human visual system's capability to adjust to widely varying colors of illumination in order to approximately preserve the appearance of object colors. Chromatic-adaptation transforms are needed when dealing with color reproduction in cross-media. In this research our application of color appearance model will follow Fairchild's revision of CIECAM97s.[49] The CIE 1997 Interim Color Appearance Model (Simple Version), abbreviated CIECAM97s was proposed in 1997 in response to the needs of the imaging industry for a single-applicable, color appearance model for device-independent color imaging application. The revised model makes it more practically applicable.

2.3.6 Color Difference for Color Images

When dealing with perceived color difference between images, traditional method is to apply a standard color difference formula on a pixel-by-pixel basis and then examine statistics such as mean, standard deviation, etc. This often produces undesirable results when dealing with images that have been spatially altered, such as those processed with halftone algorithm.[51] To solve this problem, Zhang and Wandell proposed the S-CIELAB metric that extended the standard CIELAB ΔE equation by using a series of spatial filters.[51] The flow chart using original S-CIELAB is shown in Figure 2-4.

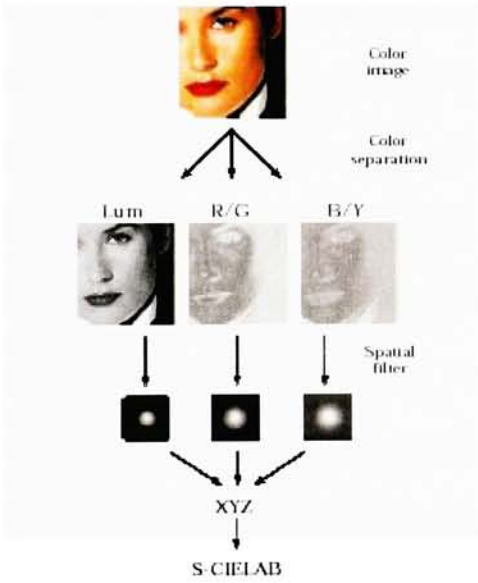

***Figure 2-4**. Flow chart of computing S-CIELAB(copied from reference 51)*

To compute the color difference, digital color images are spatially filtered using a pattern-color separable method[51] and then converted into CIELAB representation. The first step in using S-CIELAB is to transform the input images into a device independent space, such as CIE XYZ tristimulus values or LMS cone responses. This can be done

very easily for spectral images with the device characterization and using chromatic-adaptation. The filtering is then performed in an opponent color space, AC_1C_2, that containing one luminance and two chrominance channels. The AC_1C_2 color space were determined through a series of psychophysical experiments testing for pattern color separability.[52] The transformation between AC_1C_2 and XYZ is given in Eq. 2-22.

$$\begin{bmatrix} A \\ C_1 \\ C_2 \end{bmatrix} = \begin{bmatrix} 0.279 & 0.72 & -0.107 \\ -0.449 & 0.29 & -0.077 \\ 0.086 & -0.59 & 0.501 \end{bmatrix} \begin{bmatrix} X \\ Y \\ Z \end{bmatrix} \qquad (2-22)$$

The details of the spatial filters can be found in references 50 and 51. In this research, however, the filtering will be performed in the frequency domain, rather than the spatial domain, by following Johnson and Fairchild's method.[49] Filtering in the frequency domain is performed using a simple multiplication, rather than a series of convolutions in spatial domain. Also, specifying the filters purely in the frequency domain allows for more precise control over the shape of the filter. The opponent channels must be first transformed into frequency domain by using Fourier transform. The filter in the luminance channel is given by a simple description of the general shape of the human contrast sensitivity function (CSF) proposed by Movshon and Kiorpes[53] as shown in Eq. 2-23:

$$csf_{lum}(f) = 75 \cdot f^{0.2} \cdot e^{-0.8 \cdot f}, \qquad (2-23)$$

where f is the frequency. It is important to note that csf_{lum} here behaves as a band-pass filter with peak around 4 cycle per degree (cpd). As recommended by Johnson and Fairchild,[50] csf_{lum} can be normalized such that the DC component will not change after

filtering. This will make it consistent with the existing color difference formulas that accurately predict color differences of simple patches. Two chrominance channel filters are given in Eq. 2-24 and Eq. 2-25 respectively:

$$csf_{rg}(f) = a_1 \cdot e^{b_1 \cdot f^{c1}} + a_2 \cdot e^{b_2 \cdot f^{c2}}, \tag{2-24}$$

$$csf_{by}(f) = a_3 \cdot e^{b_3 \cdot f^{c3}} + a_4 \cdot e^{b_4 \cdot f^{c4}}, \tag{2-25}$$

where csf_{rg} and csf_{by} are filters for chrominance red-green channel and chrominance blue-yellow channel respectively, a_1= 109.1413, b_1= -0.0004, c_1= 3.424, a_2= 93.6, b_2= -0.0037, c_2= 2.168, a_3= 7.033, b_3= 0.000, c_3= 4.258, a_4= 40.691, b_4= -0.104, c_4= 1.649.

The filtered opponent channels are then transformed back into CIE XYZ space using the inverse of Eq. (2-22). The color differences between the original and the reproduced image, therefore, can then be calculated pixel-by-pixel using CIELAB ΔE^*_{ab} formula. The mean color difference then can be obtained to represent the color difference between these two images. An alternative way is to apply CIEDE2000 color difference equation on the filtered images.[50]

2.3.7 Image Quality of Color Image

To deal with the IQ of color image in this research, we need to define some distortion factors. The color difference for color image as mentioned above can be a candidate for one of the distortion factors. Since noise is always involved in imaging system, therefore, the graininess can be chosen as another distortion factor to represent the noise effect. Different number of channels or basis functions, different objects in optimization procedures to estimate the spectra and number of terms of digits used in multivariable regression will impact the accuracy of spectra and color. These accuracies of spectra and

color will affect the spreading level of spectra and colors around their true values, hence, impact the sharpness and contrast of the final color images for display. Therefore, sharpness and contrast can be treated as distortion factor as well.

2.3.7.1 Graininess Factor

Typically, root mean square (RMS) granularity is popularly used as an objective measure in evaluating the graininess of the images.[54] In this experiment, the objective measure of graininess is defined as the RMS error of original and its reproduction images, in the luminance channel of S-CIELAB opponent color space, after filtering as mentioned in previous section.

2.3.7.2 Sharpness Factor

To evaluate the effect of resolution on perceived image quality, Barten [55, 56, 57] proposed so-called square root integral (SQRI) as shown in Eq. 2-26.

$$SQRI = \frac{1}{\ln 2}\int_0^{f_{\max}} \sqrt{\frac{M(f)}{Mt(f)}}\frac{df}{f}, \tag{2-26}$$

where f is the angular spatial frequency at the eye of the observer in cpd, f_{max} is the maximum angular spatial frequency displayed. $M(f)$ is the modulation threshold function (MTF) of the display, and $Mt(f)$ is the modulation threshold function of the eye. The inverse of the modulation threshold function of the eye is usually called the contrast sensitivity function (CSF) which is given in Eq. 2-27.[57]

$$CSF(f) = \frac{1}{Mt(f)} = a \cdot f \cdot e^{-b \cdot f} \cdot \sqrt{1 + c \cdot e^{b \cdot f}}, \tag{2-27}$$

where

$$a = \frac{540 \cdot (1 + 0.7/L)^{-0.2}}{1 + 12/[w \cdot (1 + f/3)^2]}, \quad b = 0.3 \cdot (1 + 100/L)^{0.15}, \quad c = 0.06,$$

and w is the angular display size in degree, calculated from the square root of the picture area, and L is the effective display luminance in candelas per square meter. Barten[57] also suggested that, for pictures with a large luminance range, such as pictorial scenes, a luminance values equal to twice the average luminance should be used. It should be emphasize that SQRI is independent of image content. Researchers [57, 58, 59] indicated that SQRI values were correlated well to the subjective image sharpness for each individual image.

2.3.7.3 Contrast Factor

Calabria and Fairchild[13] proposed an empirical mathematical equation of Single Image Perceived (SIPk) contrast. This equation provides us a tool to judge contrast in color image without reference to an original image. Though the validity of this equation for other image experiments needs further study, SIPk was selected as fourth distortion factor in this experiment. SIPk is given in Eq. 2-28.

$$SIPk = -1.505 + 0.131k_c + 0.151k_l + 666.216k_s\ , \tag{2-28}$$

where k_c, k_l, k_s are image chroma standard deviation, lightness standard deviation and the standard deviation of high-frequency lightness image (filtering by Sobel filter) respectively.

2.4 Spectral Database: Lippmann2000

Mitchell Rosen, a color scientist in MCSL, proposed to create a publicly accessible database of spectral images. This database is named Lippmann2000 in honor of Gabriel

Lippmann who in 1891 devised a method to perfectly reconstruct the spectral content of real world scenes.[61] This site has been conceived of as a resource for investigators in the field of spectral imaging with emphasis on the sub-topics of interest to the research staff and faculty of the Munsell Color Science Laboratory. Currently, it contains six sections. They are Real World Spectral Images, Synthesized Spectral Images, Technical Papers on Spectral Imaging, Programs Useful for Spectral Imaging Research, Spectral Database and Spectral Imaging Links. It is still an ongoing database. Some data and technical reports from this dissertation research have been contributed to the Lippmann2000 database.

3. SPECTRAL IMAGING FOR HUMAN PORTRAITURE

In this research, spectral imaging for human portraits from various races is dealt with. As mentioned in previous chapters, for better imaging system calibration, new approach of capturing spectral images of human portraiture is proposed. The designed imaging system will be calibrated directly based on real human subjects and has the capability to provide accurate spectral images of human faces, including facial skin as well as the lips, eyes, and hair, from various ethnic races. The facial spectral reflectances obtained were analyzed by PCA method. Based on the results of PCA, spectral images using both three and six wide-band spectral sampling were estimated.

3.1 Spectral Imaging System Design

The portrait studio digital camera used for this research was a SONY DKC-ST5 Digital Photo Camera. It is a high-quality electronic photography system, using a three-chip high-resolution CCD camera with total 1,400,000 pixels. Its A/D conversion uses a 10-bit lookup table for each R, G and B channel, which makes flexible color gradation representation. Its output image is 24-bit, 8-bit for each channel, size of 2048×2560 pixels with TIFF format. A 202 half C.T blue filter, Professional Lighting Filters, Bogen Photo Corp., was chosen to give additional filtered RGB for six-band spectral imaging. Its spectral transmittance is shown in Fig. 3-1 which was measured using a Macbeth Color-Eye 7000, spectrophotometer. The criterion here is to choose a filter with some variation in spectral transmittance and the transmittance should not be too low in any

wavelength. Mathematically, adding one filter should provide three linear independent equations as mentioned in previous sections. Considering the fact that, generally, the blue channel image of CCD camera has relative low image-noise ratio, it is better to choose a filter with relatively high spectral transmittance in the short wavelengths. Fig. 3-1 shows that the spectra have more absorption in long wavelengths than that in short wavelengths.

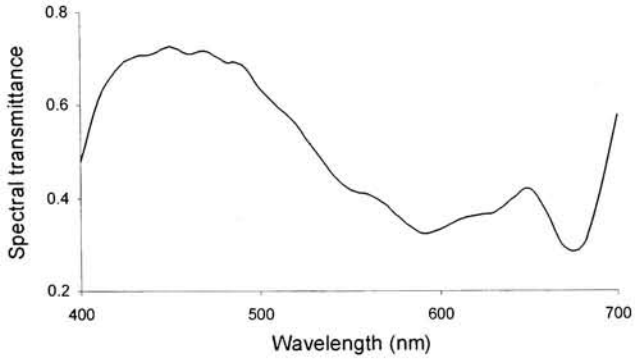

***Figure 3-1**. Spectral transmittance of filter, 202 half C.T blue.*

The lighting system consisted of two lighting heads (Scanlite Digital 1000, Elinchrom) with Halogen Photo Optic lamps (FEL/1000w, 120V). A Photo Research Inc. SpectraScan 704 (PR-704) spectroradiometer was used in the spectral measurement. The

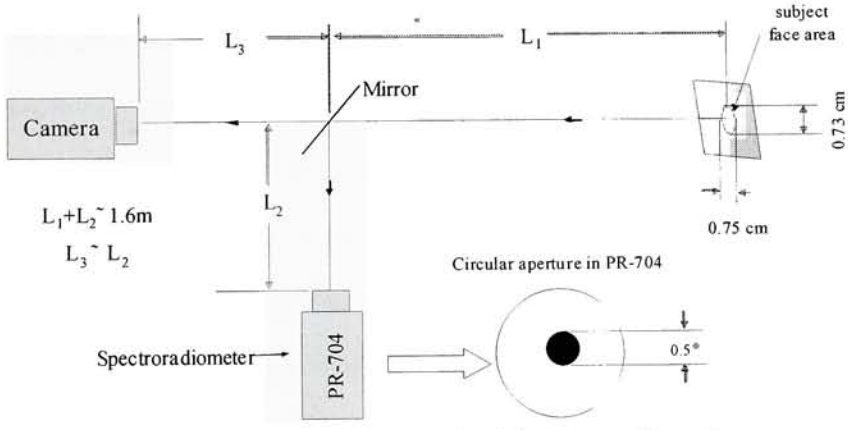

***Figure 3-2**. Scheme of optic path of the spectral imaging system.*

wavelength range used in this experiment is in visible region, 400 ~ 700nm with 2nm interval. The optical path of the spectral imaging system is shown in Fig. 3-2.

A picture of the main imaging system is shown in Fig. 3-3.

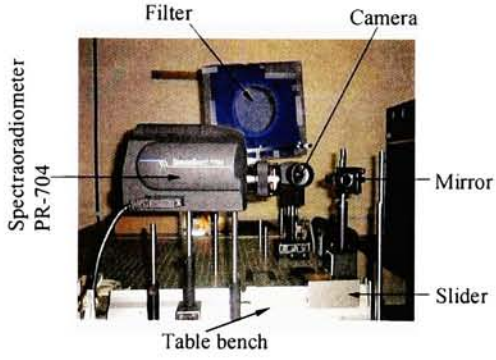

***Figure 3-3**. Picture of the spectral imaging system.*

One difficult part of this research was to measure the spectral reflectance and its corresponding digital count (mean value) at the same position. This was accomplished by adding an optical mirror and spectroradiometer PR-704 as shown in Fig. 3-2 and Fig. 3-3. The circular aperture setting of 0.5 degree in PR-704 was used for the spectral measurement as illustrated in Fig. 3-2. A mirror was attached to a slide mounted carrier that could move along the table bench. This system was calibrated so that the pixel positions in the image of a subject that contributed to the spectral measurement in PR-704 were known. The distance from the subject to PR-704, L_1+L_2 in Fig. 6, was selected in such a way that the uncertainty of calibrated pixel area was less than 2.5% on the assumption that the subject surface would move back and forth around the calibrated position within 2cm. The distance selected was about 1.6m. A longer distance could have been selected for accuracy purposes. However, the area covered by the aperture of PR-

704 would be too large and the spectra measured would be spatially averaged too much. It was estimated that, with ~3% error of subject surface that corresponding to subject moving back and forth about ±3 cm, the color difference, ΔE^*ab was less than 0.08 on average of 540 samples. This proved that the designed imaging-measurement system, theoretically, was quite accurate. The distances from mirror to PR-704 and mirror to digital camera were almost the same.

During the experiment the subject was sitting on a chair with his/her head against a holder. The subject was asked to adjust his/her chair up and down, left and right, until the position of interest fell into the grid box which was shown on the monitor. The author first took a picture of the subject, then moved the mirror to its calibrated position and made a spectral measurement of the same subject at the same position. The spectral reflectances of various face surfaces of subject and his/her corresponding camera responses, digital counts, therefore, were then obtained. Based on this system setting, the spectral measurements matched the different geometries as detected by the camera.

3.2 Imaging System Calibration

During the experiment, the camera automatic white balance was disabled by setting the temperature to 3,200K for tungsten lighting. For signal-noise considerations, the shutter speed was set to 1/1000 with the exposure of ISO160. Under the lighting and camera conditions we would use for real image capturing, a high quality white reference, barium sulfate coated paper with spectrally flat and uniform property, was employed to adjust the camera setting so that the image of white reference (at the position where subject sat for

imaging) would give maximum digit values without saturation and satisfy the white balance. The spectral radiance of the lighting on the position where real subjects sat for imaging was measured by PR-704 with the white reference as a standard. The measured spectral radiance is shown in Fig. 3-4.

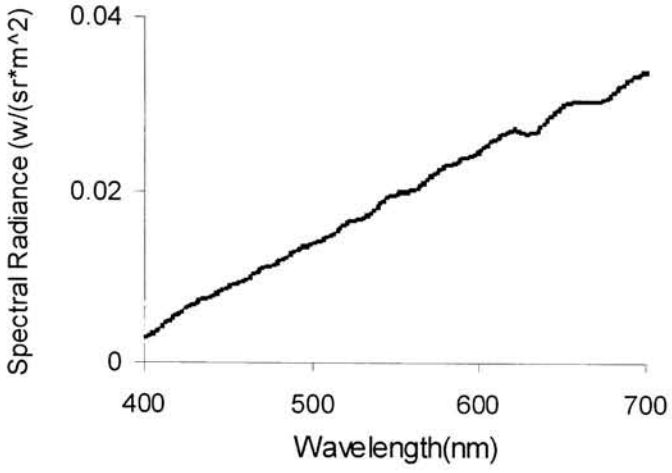

Figure 3-4. *Spectral radiance of the lighting fallen on subject*

Fig. 3-4 shows that the spectral radiance of the lighting used in this experiment has relatively very smaller intensity in the range of short wavelength. This is a disadvantage since it will produce even more noise in the blue channel of the digital camera. Some other necessary measurements and calibrations were performed before the experiment was completed.

3.2.1 Imaging Spot Calibration

Printed samples with different shapes and sizes were used to calibrate the imaging spot so that the pixel positions in the image of a subject that contributed to the spectral measurement in PR-704 could be determined. Printed samples with various sizes were placed at the imaging position and their spots viewed from the PR-704 were checked.

The sample with its spot viewed through PR-704 matching the aperture spot of the PR-704 was selected as spot calibration target. Image of this selected printed sample was then taken by the digital camera. Its corresponding pixel positions in the image could then be determined. In practice, an equation was used to fit the spot pixels in the image. In the following experiment, this equation was used to determine the pixels of the subjects' face area that contributed to the spectral measurements. An important note here is that this procedure was repeated from time-to-time to make sure that each component of the imaging system had not been moved. The camera system has a function to create a grid box with any size and any position in the image frame that could be displayed on an attached monitor. A fixed grid box located at the center of image frame was created and its position and size were fixed through the whole experiment. The size of this grid box was adjusted to the same diameter size as the image spot of the printed spot calibration target. With those settings, it was easy and safe to maintain the imaging system at its calibrated position through whole period of the imaging experiments.

3.2.2 Spectral Reflectance of Mirror

To measure the spectral reflectance of the mirror under the experimental condition, we first placed the white reference paper, as mentioned above, at the calibrated position where real subjects would be placed for pictures and spectral measurement. Next, we measured the spectral radiance of that position with the mirror and PR-704 located at their calibrated positions. Then, we placed the PR-704 perpendicularly to the white reference paper, without mirror, with the same distance as that from PR-704 to mirror plus mirror to white paper at the previous step and took the measurement of spectral

radiance. Knowing the spectral reflectance of the white reference paper, the spectral reflectance of the mirror, therefore, could be easily calculated. Its spectral reflectance is shown in Fig. 3-5.

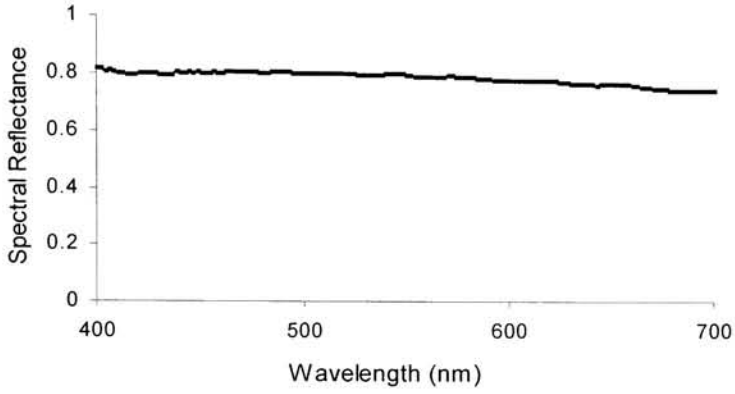

***Figure 3-5**. Spectral reflectance of the mirror*

3.2.3 Optoelectronic Conversion Function of Digital Camera

The next pre-experiment measurement was to measure the optoelectronic conversion function (OECF) of the camera. Most digital cameras have nonlinear photometric response that the relationship between the digital numbers in the image file and the scene reflectance which produced the digits is nonlinear. This relationship is known as the optoelectronic conversion function. The nonlinearity is employed to minimize visual artifacts caused by optical and digital limitations.[63] To connect those digits to the tristimulus values, the digits should be first linearized to transform to linear reflectance space based on the optoelectronic conversion function. The common methods are fit procedure using one-dimensional look-up table involving interpolation or a polynomial function etc.

The camera setting and lighting system were the same as used for real imaging. The OECF was determined by imaging gray scales, Kodak GrayScale, Q14, with the addition

of a high quality white paper mentioned above and a complete dark. The gray scale was located at the position where subject would sit for real imaging. Each gray scale was taken one shot containing three R, G, and B channel images. The images of gray scales were taken at the same position to avoid the non-uniformity of the illumination involved. The camera system has a function to create a grid box with any size and any position shown on the screen of an attached monitor. Using this function, during measurement, each gray scale was easily placed at the same position shown by grid box which was located at the center of the image frame. For each gray scale, the digital count of image for each channel was a mean of the pixel values clipped at the center area of the image with the pixel size of 31x41 pixels.

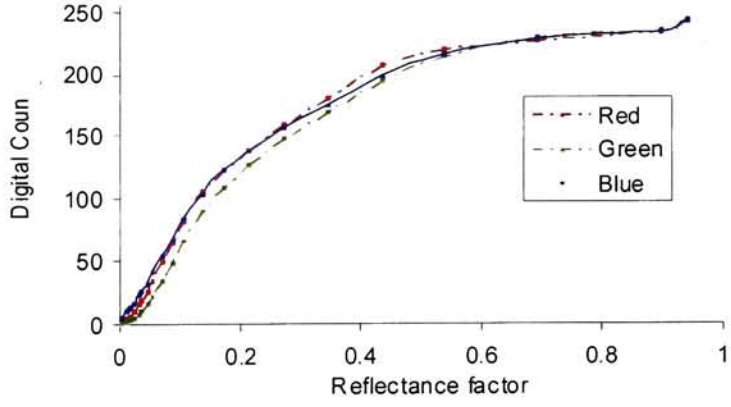

***Figure 3-6**. The optoelectronic conversion curve of the camera*

The composite OECF of the camera is shown in Fig. 3-6. The OECF curves shown in Fig. 3-6 are not linear. After comparing with many fit methods, such as low-order polynomial fit, exponential fit, GOG model[68] fit and etc., we find that three 1-D look-up tables will be a best choice to relate the digital counts to reflectance factors. This might

hint that the OECF for this camera is piece-wise linear. As mentioned in the previous section, the linearized R, G, B will be calculated based on OECF using these three 1-D look-up tables.

3.2.4 Spectral Sensitivities of Digital Camera

Two methods, monochromator method and interference filter method, could be employed to measure the spectral sensitivity responses of the digital camera. Imai[62] showed that the monochromator method is a better choice and therefore it was used for this experiment. A light source Module Model 740-20 (serial 8553) in connection with double monochromators, part of the Optical Radiation Measurement System Model 740A (serial 185268-5) from Optronic Laboratories Inc., was used in this measurement. Hewlett Packard Hamsom 6274A DC Power Supply (0 – 60V 0 – 15A) was set to provide stable 0.06A current to the light. This light source with double monochromator provided narrow-band illumination at the 10nm exit slit, over a range of 380 – 780nm at 5nm intervals. An optic fiber with a neutral filter was attached to the exit slit. The surface of the digital camera lens was kept to a proper distance, 91cm for this experiment, from the surface of the optic fiber. The experiment was performed in a dark environment. Each image was cropped in the same position centered in the light spot producing a proper, i.e., 60x50 pixels, 2-D RGB image. Based on the OEF measured above, 2-D RGB images were then linearized into reflectance space. After dark current correction, the averaged linearized digital counts for each channel of the digital camera over wavelength range then could be obtained. Next, a calibrated photo-detector (Optronic Laboratories Inc., OL730-5C Silicon Photo detector SIN:1152 Hex Key with calibration certification data:

May 30, 1998) was attached to the exit slit. The spectral response of this standard photo-detector was given and the source spectral irradiance, radiance and current were measured over the same range used above by Optronic Laboratories Inc., Radiometer 730A (serial: 850190).

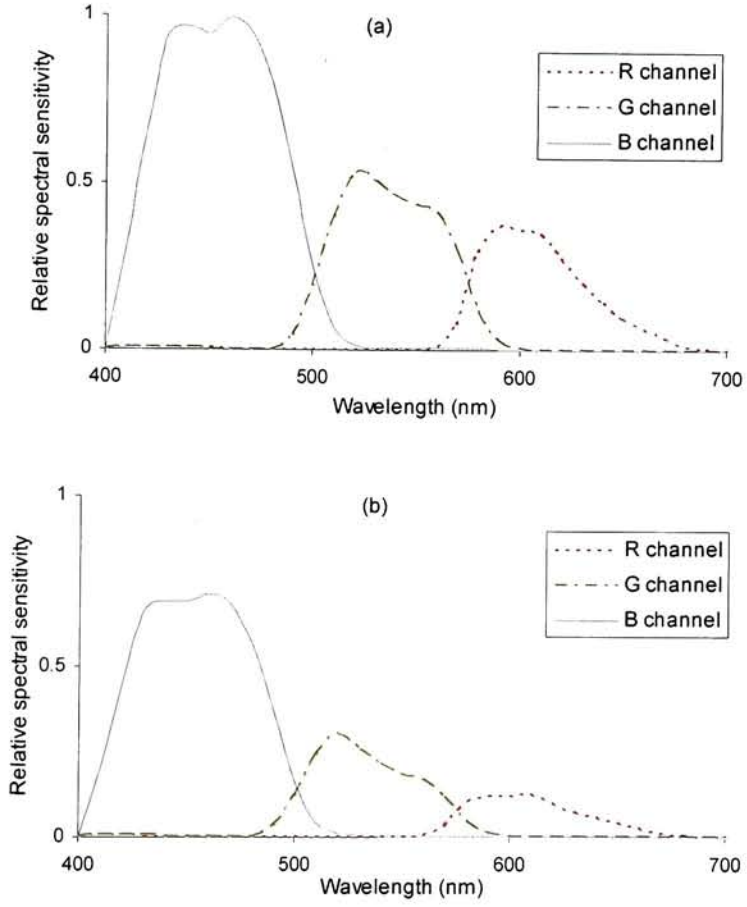

***Figure 3-7**. Measured relative spectral sensitivities of digital camera. (a)without external filter;(b)with external filter, 202 half C.T. blue.*

Based on the average linearized digital counts and the measured irradiance or radiance and current data, the spectral sensitivity of R, G, and B channels of the digital

camera could be obtained. The relative spectral sensitivity of the camera is shown in Fig. 3-7.

The spectral sensitivity of the camera indicates that the wavelength response range of the camera is from 380nm to 700nm. Therefore, just as many researchers used, we will choose the wavelength range of 400nm to 700nm in our measurement. Since the PR704 can measure the spectra with the range from 380nm to 780nm with 2nm interval, all spectral data used in this experiment were interpolated into wavelength step of 2nm. The color matching function (CIE 1931, 2° observer), and other standard illumination spectra would then be interpolated into wavelength step of 2nm from 400nm to 700nm.

3.3 Spectral Imaging Experiment

A total 34 of subjects from age 18 to 40, 11 female and 23 male participated in the experiment. The experiment was performed from June to January, about 8 months. The subjects can be categorized into five races, 11 subjects for Pacific-Asian, 8 for Caucasian, 7 for Black, 6 for Subcontinental-Asian and 2 for Hispanic.[64] During the experiment the subject was sitting on a chair with his/her head against a holder. For each subject, two images, with and external filter, were taken for future spectral image construction. They were then the asked to adjust his/her chair up and down, left and right, until the position of interest face area fell into the grid box which was shown on the monitor. The author first took two pictures of the subject, with and without external filter, then moved the mirror to its calibrated position and made spectral measurement of the same subject at the same position. Each subject provided 16 spectral reflectances which, in general, would

contain 10 for facial skin, 3 for hair, 2 for eye and 1 for lips. The locations of spectral measurement were randomly selected considering uniformity of sampling. Therefore, a total 540 of spectral reflectances and their corresponding camera digits were obtained for imaging system calibration and modeling.

3.4 Statistical Analysis for Spectral Reflectances of Human Face

The measured spectral reflectances in terms of different races are shown in Fig 3-8. Light-pigmented races, the Pacific-Asian and Caucasian, display obvious absorption bands while those absorption bands are, more or less, masked for heavy-pigmented races, the Black and Suncontinental-Asian . Those spectral reflectances in terms of different face parts are shown in Fig. 3-9.

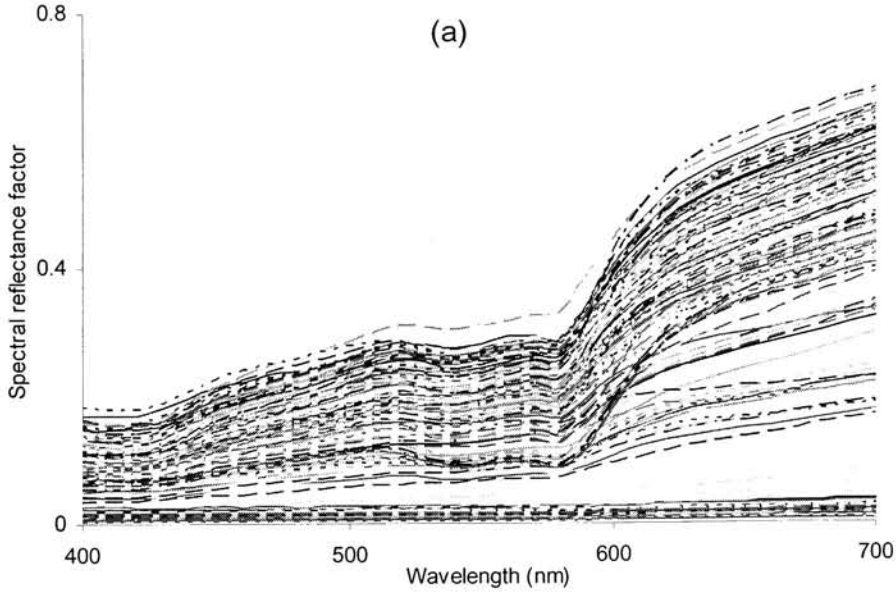

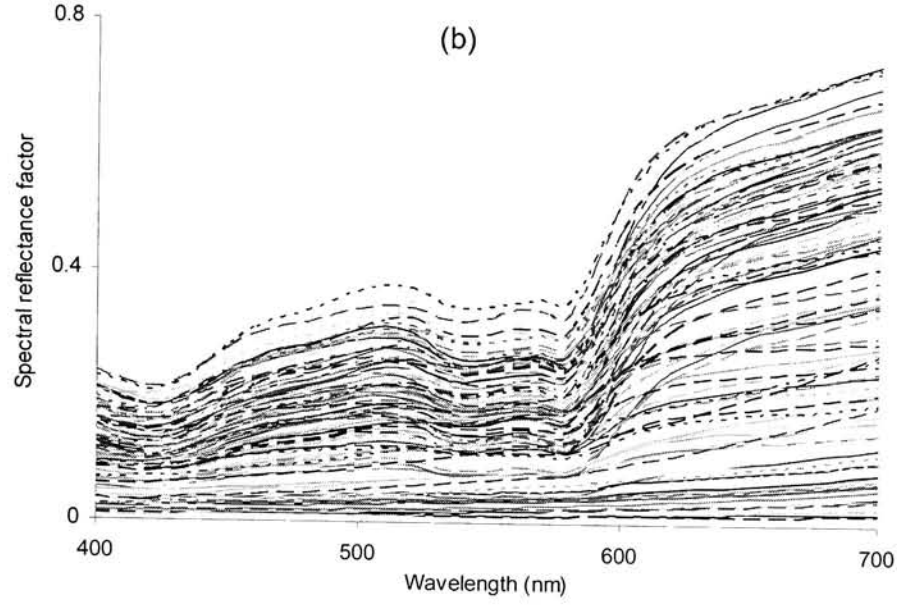
(b)
0.8
0.4
0
Spectral reflectance factor
400
500
600
700
Wavelength (nm)

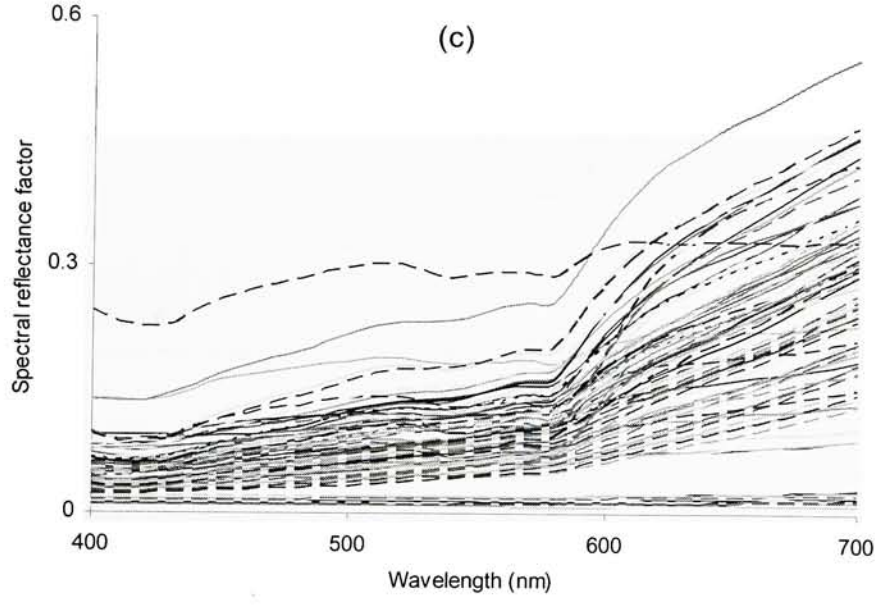
(c)
0.6
0.3
0
Spectral reflectance factor
400
500
600
700
Wavelength (nm)

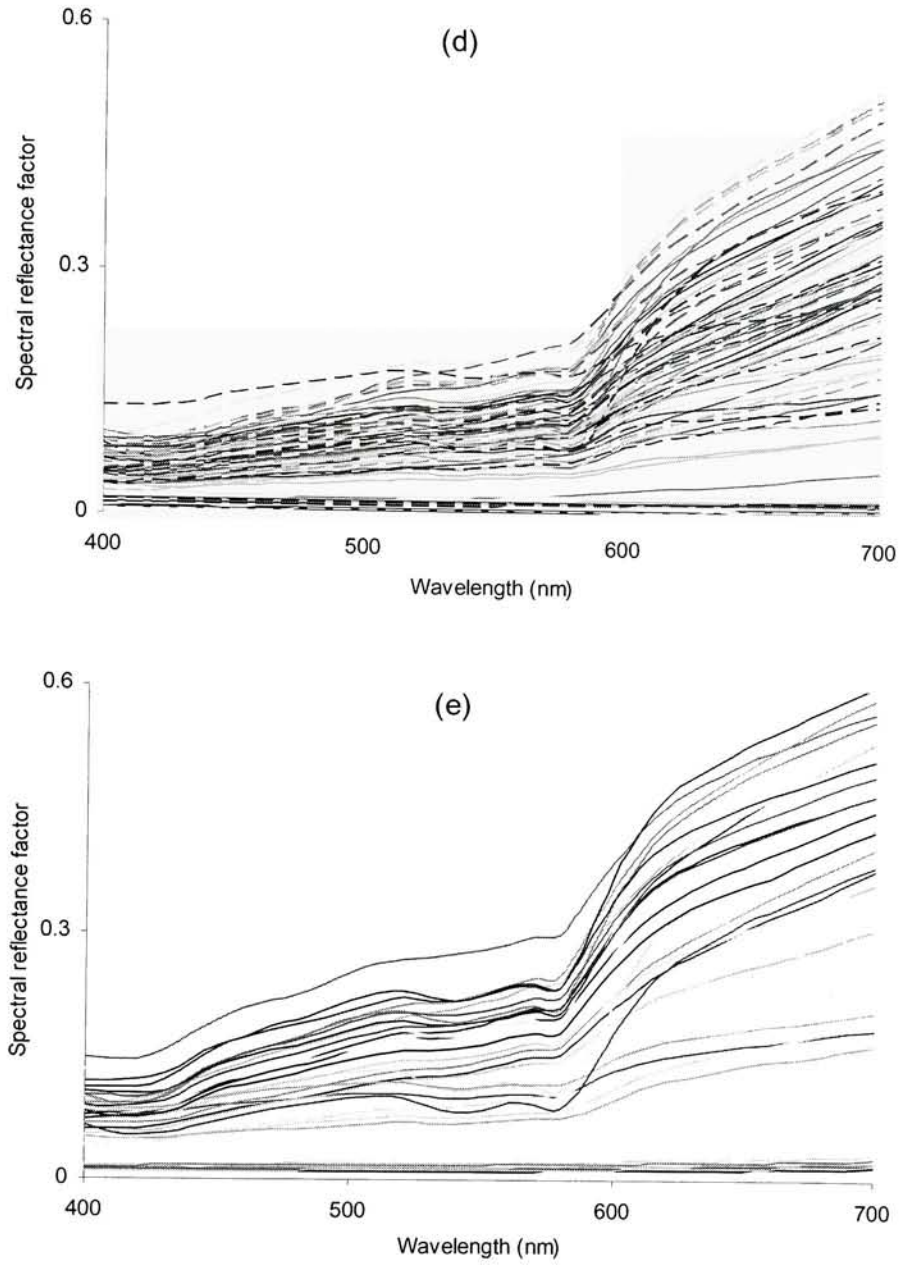

***Figure 3-8**. Measured spectral reflectances in terms of different races. (a) for Pacific-Asian; (b) for Caucasian; (c) for Black; (d) for Subcontinental-Asian; (e) for Hispanic.*

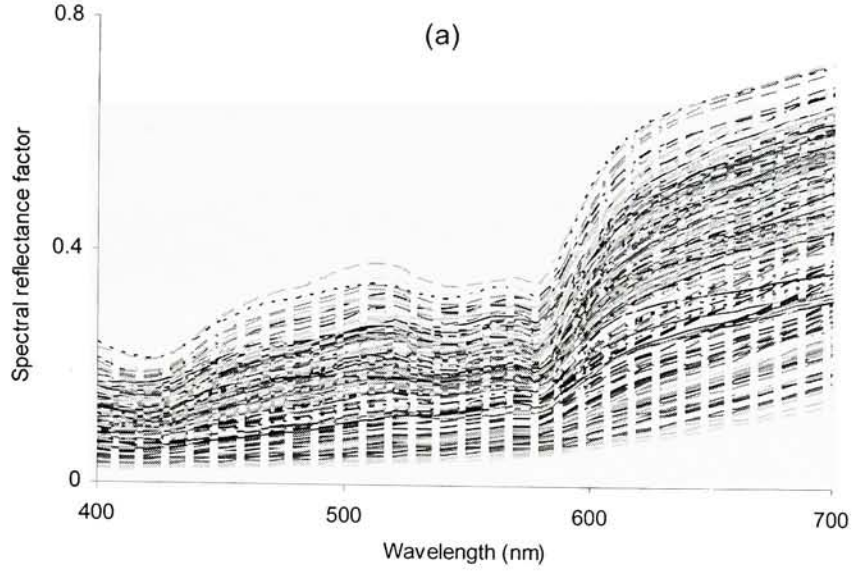
(a)
0.8
0.4
0
Spectral reflectance factor
400
500
600
700
Wavelength (nm)

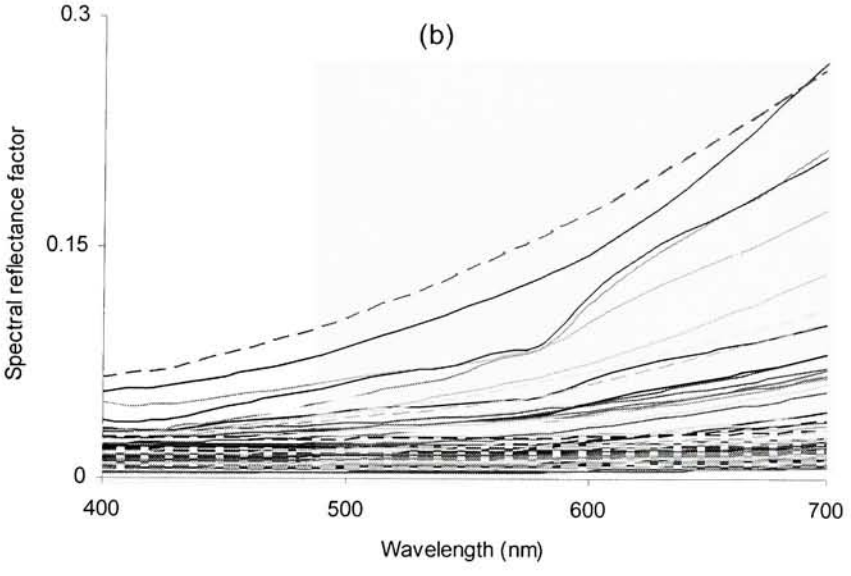
(b)
0.3
0.15
0
Spectral reflectance factor
400
500
600
700
Wavelength (nm)

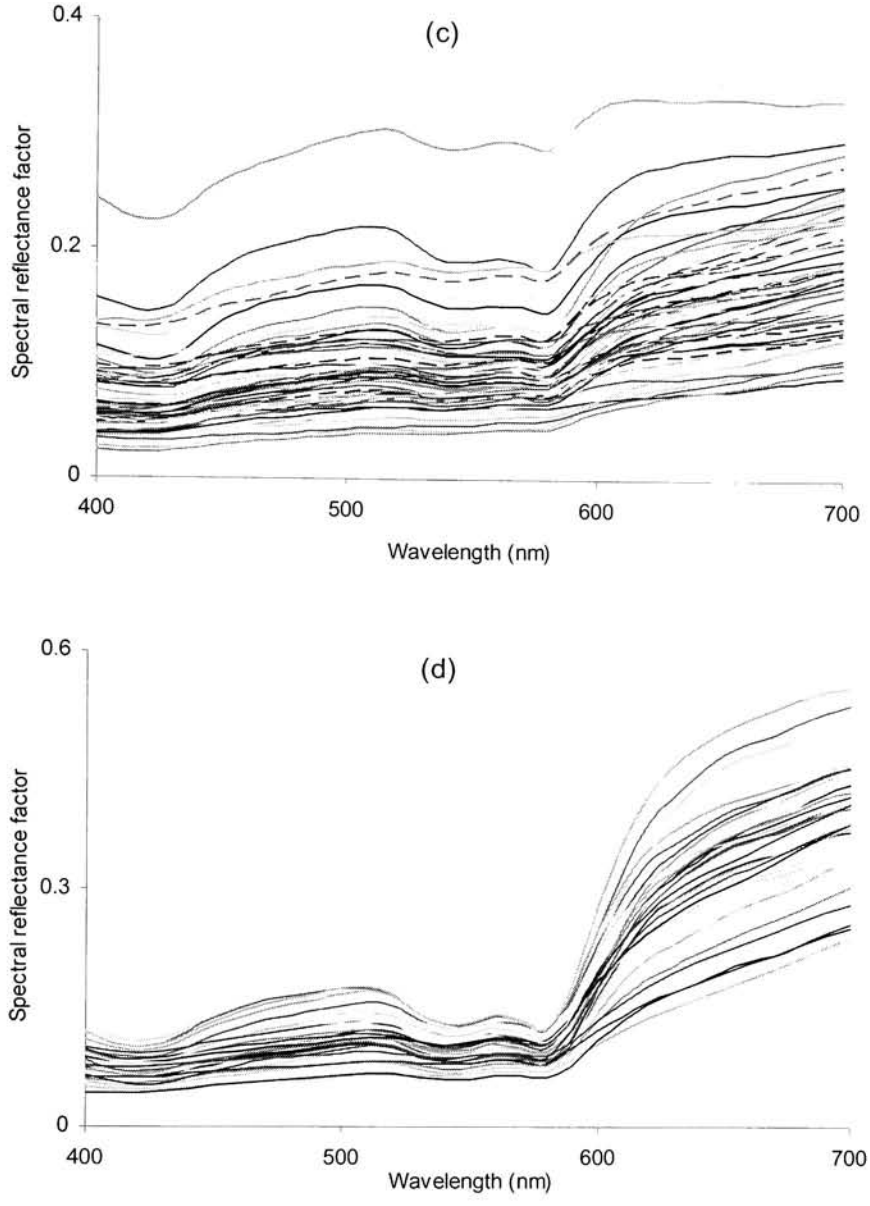

Figure 3-9. *Measured spectral reflectances in terms of different face parts. (a) for skin; (b) for hair; (c) for eyes; (d) for lips*

The spectral reflectances in terms of different face parts display distinguished spectral characterizations. For example, the spectra of hair display monotonically increasing behavior without obvious absorption bands while spectra of lips showing strong absorption bands. Those behaviors are discussed in detail in the following sections.

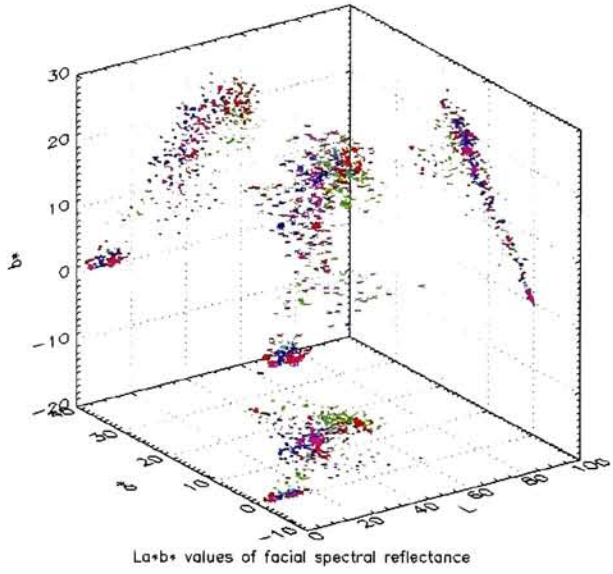

Figure 3-10. *L*, a* b* plot and their corresponding projections for spectra of different races. Red dots are for Pacific-Asian, green for Caucasian, blue for Black, cyan for Hispanic and magenta for Subcontinental-Asian.*

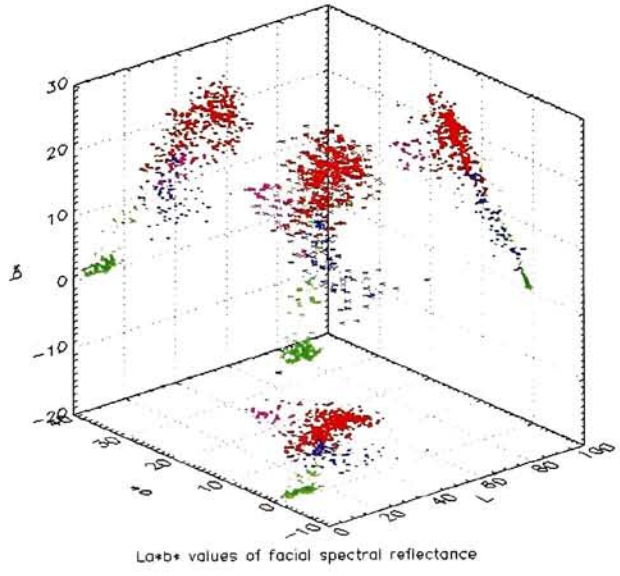

Figure 3-11. *L*, a* b* plot and their corresponding projections for spectra of different parts. Red dots are for skin, green for hair, blue for eyes and magenta for lips.*

To provide more visual pictures of the measured spectral reflectances of the human face, the L*, a* and b* 3D plot and their corresponding projections are shown in Fig. 3-10 and Fig. 3-11 where Fig. 3-10 is for individual races and Fig. 3-11 is for different face parts. Fig. 3-10 indicates that in CIELAB space, the spectral reflectances of human face are mixed together and there are no significant clusters for different races. However, if we plot them based on different face parts, it shows significant clusters for different face parts. This suggests that different face parts have their specific spectral and color characterizations. This property may give us some practical suggestion when performing pattern recognition for human face.

3.4.1 PCA Results from Various Races and Different Face Parts

PCA method will be employed to analyze the statistical characterizations of the spectral reflectances. Based on the PCA results, the cumulative contribution percentages of the first one to six principal components for spectral reflectances of all races (the combined data set) as well as individual races are shown in Table 3-1. The abbreviations PA for Pacific-Asian, C for Caucasian, SB for Subcontinental-Asian, B for Black, H for Hispanic and AR for all races will be used in the following sections.

The results in Table 3-1 show that the first three principal components will cover over 99.8% of the variance for all spectral data of all races and spectral data of individual races as well. This suggests that a spectral imaging system with the proper selection of three basis functions will provide sufficiently accurate spectral reconstruction for all races as well as any individual races. Further observation indicates that, with three basis

functions, the spectral reconstruction of Pacific-Asian, Caucasian and Hispanic races will have slightly more accurate results than that for Black and Subcontinental-Asian.

Table 3-1. *Cumulative contribution percentage of principal components calculated from spectra of all races and individual races. See text for abbreviations.*

Race	Number of principal components					
	1	2	3	4	5	6
PA	98.56	99.76	99.95	99.98	99.99	99.99
C	97.75	99.65	99.91	99.96	99.98	99.99
SB	97.39	99.47	99.84	99.99	99.99	100.00
B	94.12	99.46	99.82	99.98	99.99	100.00
H	98.57	99.73	99.95	99.99	100.00	100.00
AR	97.89	99.57	99.89	99.97	99.99	99.99

The corresponding first three principal components are shown in Fig. 3-12. Fig. 3-12 indicates that the first three principal components of each race and all races have very similar shapes. This suggests the possibility that the first three principal components of any race may be used to describe the spectra of other races.

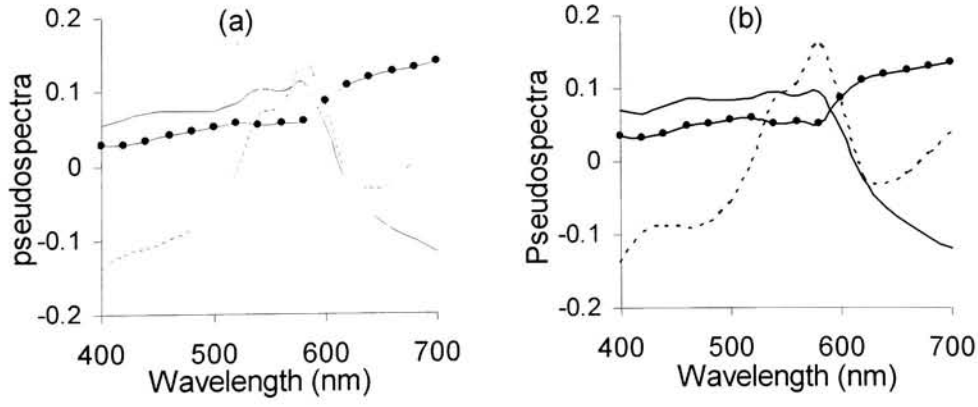

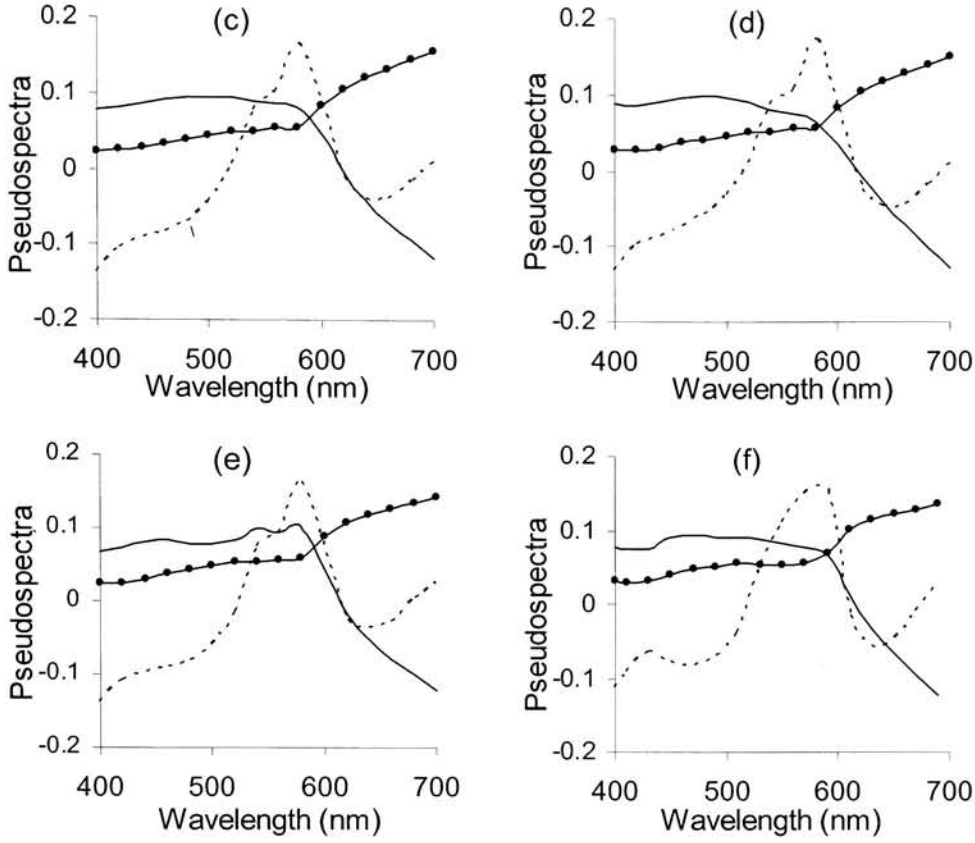

Figure 3-12. *Graphs of the first three principal components of spectral reflectances for individual races and all races. Solid-dot line is for the 1st component, solid line for the 2nd component and dot line for the 3rd component. (a) Pacific-Asian; (b) Caucasian; (c) Subcontinental-Asian; (d) Black; (e) Hispanic; (f) All Races.*

The cumulative contribution percentages of the first one to six principal components for spectral reflectances of each facial part are given in Table 3-2. Not surprisingly, the first three principal components for most parts will provide over 99.8% of the variance of spectra with one exception of spectra of lips which is about 99.7%. The PCA results in Table 3-1 and 3-2 here also verify that the spectra, or color, of the human body depends chiefly on the presence of pigment and blood; melanin and hemoglobin. The corresponding first three principal components, or basis functions, are shown in Fig. 3-13.

Table 3-2. *Cumulative contribution percentage of principal components calculated from face spectra of individual parts.*

Parts	Number of principal components					
	1	2	3	4	5	6
Skin	97.90	99.40	99.83	99.95	99.98	99.99
Hair	98.76	99.88	99.95	99.99	100.00	100.00
Eye	91.97	99.53	99.81	99.95	99.98	99.99
Lip	95.86	99.17	99.67	99.88	99.95	99.97

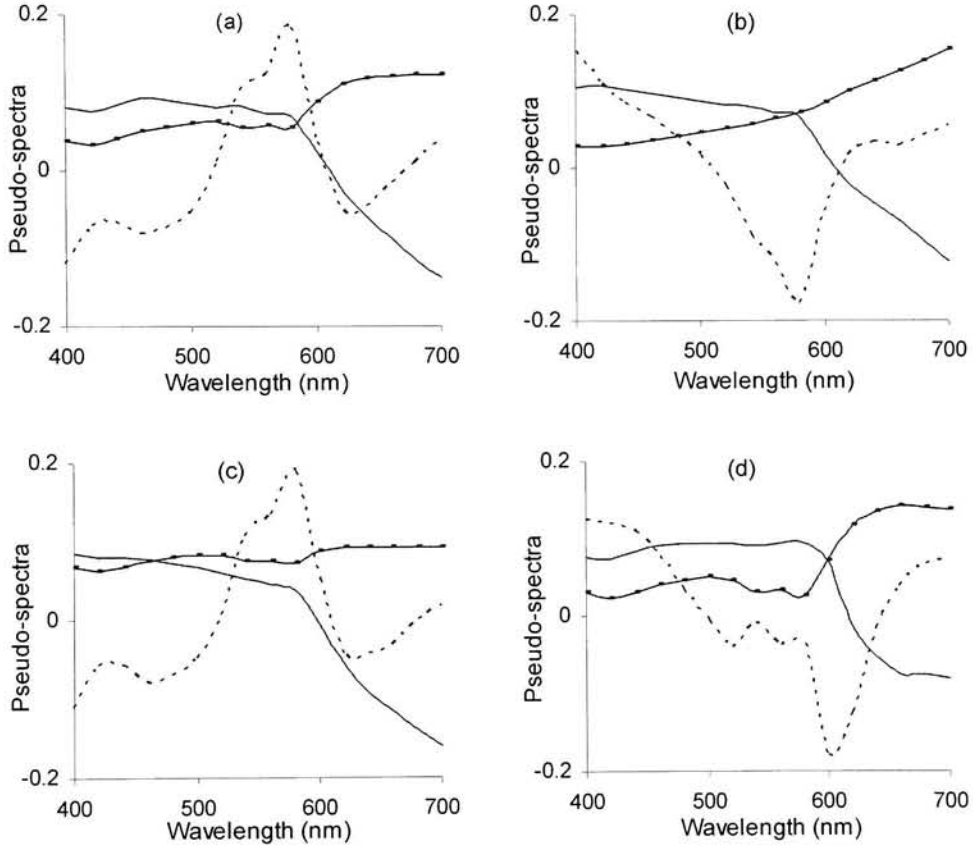

Figure 3-13. *Graphs of the first three principal components of spectral reflectances for each facial part. Solid-dot line is for the 1st component, solid line for the 2nd component and dot line for the 3rd component. (a) Skin; (b) hair; (c) eyes; (d) lips.*

3.4.2 Color Reproductions Based on Different Basis Functions

To calculate the colors the spectra should be reconstructed using Eq. 2-5. Therefore, the mean spectra are also required. The mean spectra of individual races and each face part are shown in Fig. 3-14 and Fig. 3-15 respectively for demonstration.

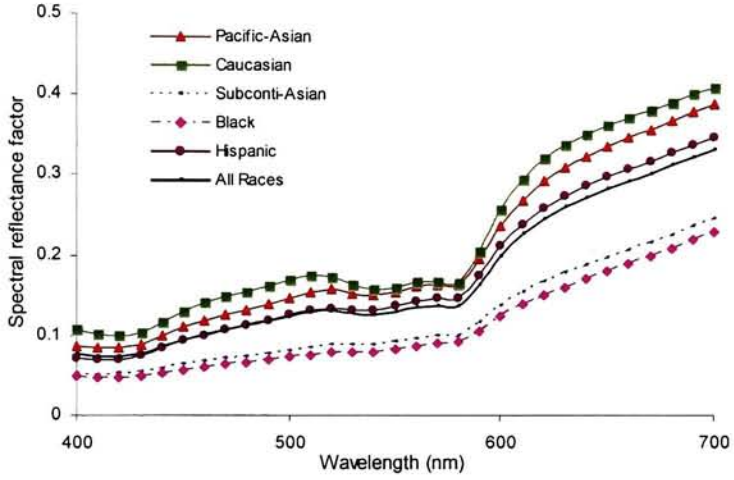

***Figure 3-14**. Mean spectral reflectances of individual races.*

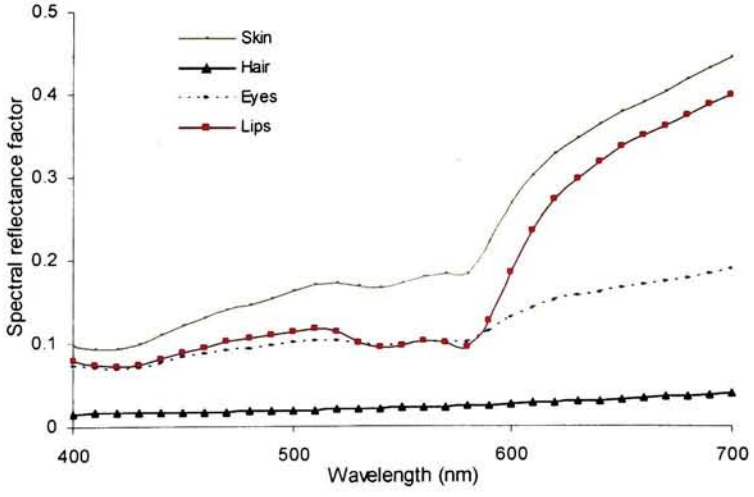

***Figure 3-15**. Mean spectral reflectances of each human facial part.*

Next the mean color differences between spectral reflectances measured and reconstructed based on the first three basis functions are considered for the application of certain sets of basis functions to their own group and to spectra of other groups as well. The color difference equation applies the CIELAB color difference with the CIE 2° observer and D_{50} illuminant. The results shown in Table 3-3 are for different races. The horizontal items are the spectral groups that yielded the principal components while the vertical items are the spectral groups the basis functions were applied to. Similar item arrangements are applied to the Tables 3-4, 3-5 and 3-9.

Table 3-3. *Mean color difference in reproduction of individual races and all races using different sets of 3 principal components. The horizontal races are the spectral groups that yielded the principal components while the vertical races are the spectral groups the basis functions were applied to. See text for abbreviations.*

	PA	C	SA	B	H	AR
PA	**0.45**	0.95	0.73	1.05	0.60	0.98
C	0.66	**0.65**	1.06	1.20	0.65	0.83
SA	0.77	1.30	**0.54**	0.81	0.92	1.28
B	1.00	1.52	0.68	**0.84**	1.16	1.51
H	0.47	0.76	0.73	1.07	**0.46**	0.90
AR	0.67	1.05	0.76	1.00	0.78	**1.10**

The basis functions based on spectra of all races will give smaller color difference for races of Pacific-Asian, Caucasian and Hispanic than that for races of Black and Subcontinental-Asian. This may be due to the facts that in heavy pigmented races, such as Black and Subcontinental-Asian, the spectral characteristics of hemoglobin are masked and show some slight specific property in spectra that need more basis functions to reproduce at the same level of accuracy as that for light pigmented races. It could also be due to the fact that more noise was involved in those data with lower signal level.

Considering individual race, not surprisingly, most races will have smallest color difference when the basis functions used for spectral reconstruction are based on their own spectra data (the diagonal color difference values). The basis functions based on light pigment races will give smaller color difference when they are applied to light pigment races. The same is true for the basis functions based on heavy pigment races applied to heavy pigment races. Mathematically, for basis functions based on all races, the variance of the data of five races are comparatively large because of including both low- and high-order statistics; for one race using its own set of basis functions the variance of spectral data is comparatively small because of the inclusion only low-order statistics. Therefore, generally, the best color reproduction or spectral matching will occur when spectra of each race employ its own set of basis functions.

Most interesting is that the first three basis functions based on any individual race can provide a smaller mean color difference for overall spectral reconstruction of all races than that derived from the three basis functions based on overall spectra (the last row). The first three basis functions of Pacific-Asian will provide the smallest color difference for overall spectra of all races; it will improve about 40%. Moreover, using this set of three basis functions, the color difference of spectral reconstruction for other races will be decreased about 20 ~ 55% compared to that using the first three basis functions yielded from overall spectra. This suggests that to obtain better color reproduction of spectral imaging system, when using three basis functions under illumination D_{50}, the basis functions based on spectra of Pacific-Asian race will be the best choice, not the basis functions based on spectra of overall races. This may be partly due to the fact that the

Pacific-Asian is medium pigmented race and its spectra have both characteristics shown in light and heavy pigmented races.

One thing should be emphasized here is that for calibration purposes, the spectral data of all races is still required to get the maximum spectral range. Further research indicates that when using six basis functions, the set of basis functions based on the spectra of overall races will be much better the choice for color reproduction of the overall spectra . The same is true in the case of using six basis functions that the best color reproduction will occur when spectra of each race employs its own set of basis functions.

One should always keep in mind, however, that the best colorimetric matching does not always guarantee to provide the best spectral matching, and vice versa. Considering spectral reproduction itself, it may be better to estimate the root mean square (RMS) error between original spectra and reconstructed spectra. To more precisely demonstrate the color reproduction of spectral matching, the indices of metamerism employing Fairman's metameric correction using parameric decomposition (Appendix A) are an alternative choice. Table 3-4.1 and 3-4.2 show the results of RMS error and mean metameric indices using the same sets of basis functions as in table 3-3, respectively. The indices of metamerism were calculated using illuminants D50 and A.

Table 3-4 indicates that for best spectral matching of overall spectra the set of basis functions based on spectra of overall races will be the best choice. Because of the reason mentioned above, the best spectral reproduction or spectral matching for spectra of each race will occur when it employs its own set of basis functions (the diagonal values). Table 3-4 also shows that overall reconstructed spectra based on the basis functions

yielded from light pigmented races will provide better color as well as spectral reproduction. As similar to the situation in the results of Table 3-3, Table 3-4.2 shows that the basis functions based on spectra of Pacific-Asian will still give much better color reproduction when applying to overall spectra of all races although basis functions based on spectra of all races will be the best choice, precisely.

Table 3-4. *RMS values and mean metameric indices of spectral reproduction for individual races and all races using different sets of three principal components. The horizontal races are the spectral groups yielded the principal components while the vertical races are the spectral groups the basis functions were applied to. (1) RMS values, unit of 10^{-4}; (2) Metameric indices. See text for abbreviations.*

	PA	C	SA	B	H	AR
PA	**29**	41	69	75	32	34
C	56	**38**	108	107	50	43
SA	51	55	**30**	32	48	40
B	57	58	34	**32**	54	43
H	27	32	62	69	**24**	32
AR	47	47	70	72	44	**39**

(1)

	PA	C	SA	B	H	AR
PA	**0.15**	0.29	0.38	0.46	0.21	0.26
C	0.25	**0.18**	0.51	0.52	0.23	0.19
SA	0.37	0.49	**0.24**	0.32	0.37	0.34
B	0.46	0.56	0.30	**0.34**	0.46	0.39
H	0.14	0.28	0.30	0.39	**0.18**	0.23
AR	0.28	0.35	0.37	0.43	0.29	**0.28**

(2)

Further research indicates that using more than three basis functions, basis functions based on spectra of all races will provide smaller errors in spectral and colorimetric matching compared to using other sets of basis function based on other individual races though the differences may not be visually detectable. In practice, however, we should consider the advantage provided by spectral of all races.

It should be emphasized here that caution should be used when using RMS error to analyze the spectral reproduction since RMS error only provides information on the absolute spectral difference between measured and estimated results. For example, in Table 3-4.1, RMS values for Caucasian and Black are the same when using basis functions based on all spectra. However, considering the much smaller absolute values of spectral reflectances of Black compared to that of Caucasian, one concludes that basis functions based on all spectra will provide better spectral reproduction for Caucasian than for Black, which can be proved from the results in Table 3-4.2 that the mean index of metamerism for Black is double the value for Caucasian.

The results shown in Tables 3-5 are indices of metamerism and RMS spectral error for spectral reconstruction using various sets of three basis functions for spectra of different facial parts. Table 3-5.1 indicates that the set of first three basis functions based on all spectra will give at least double mean color difference for hair spectral reconstruction compared that for other parts (the last column). This may be due to the fact that spectral reflectances of hair are so dark that spectral reconstruction using three basis functions based on all data will yield some negative values in some wavelengths, hence larger color difference. The results also indicate that the basis functions from skin cannot be used to describe the spectra of hair. On the other hand, somewhat surprisingly, basis functions based on spectra of hair can be used to describe other parts very well. However, since most part of human portrait will deal with skin, it is worth using the set of basis functions yielded from overall spectra with the cost of relatively large color difference of spectral reproduction for hair. Our further research indicates that this problem can be

solved using more number of basis functions based on overall spectra. Considering three basis functions based on spectra of lips, it shows that due to their specific spectral characteristics, they cannot be used to describe spectra of other parts.

***Table 3- 5**. Mean color difference and indices of metamerism in reproduction of individual face parts using different sets of 3 principal components. The horizontal races are the spectral groups yielded the principal components while the vertical races are the spectral groups the basis functions were applied to. (1) Mean color differences; (2) Indices of metamerism.*

	Skin	Hair	Eyes	Lips	AR
Skin	**0.64**	0.97	1.04	4.57	0.75
Hair	6.16	**0.13**	0.98	16.38	2.57
Eyes	1.20	0.40	**0.37**	2.03	0.62
Lips	1.45	0.70	1.13	**0.69**	1.13
AR	1.81	0.72	0.95	6.28	**1.10**

(1)

	Skin	Hair	Eyes	Lips	AR
Skin	**0.17**	0.82	0.23	0.90	0.18
Hair	1.95	**0.05**	0.29	4.47	0.71
Eyes	0.31	0.67	**0.12**	0.62	0.16
Lips	0.19	0.88	0.41	**0.13**	0.22
AR	0.53	0.66	0.24	1.50	**0.28**

(2)

The corresponding indices of metamerism are shown in Tables 3-5.2. Table 3-5.2 proves that the set of first three basis functions based on all spectra will provide very good color and spectral reproduction for skin, eyes and lips with the cost of relatively high color and spectral error for hair. On the other hand, somewhat interesting, basis functions based on spectra of eyes will provide the smallest mean metameric index of overall spectra. However, it is not a best choice for spectral reproduction of skin. As mentioned, it is worth using the set of basis functions yielded from overall spectra, which will improve about 30% color and spectral reproduction of spectra of skin compared to that using basis functions based on eyes.

3.4.3 Statistical Analysis for Skin Spectra

Since facial skin is the most important part in color and spectral reproduction of human portraits its spectral characterization is considered in more detail. As an overview to the skin spectra of individual races, their mean spectra are plotted in Fig. 3-16.

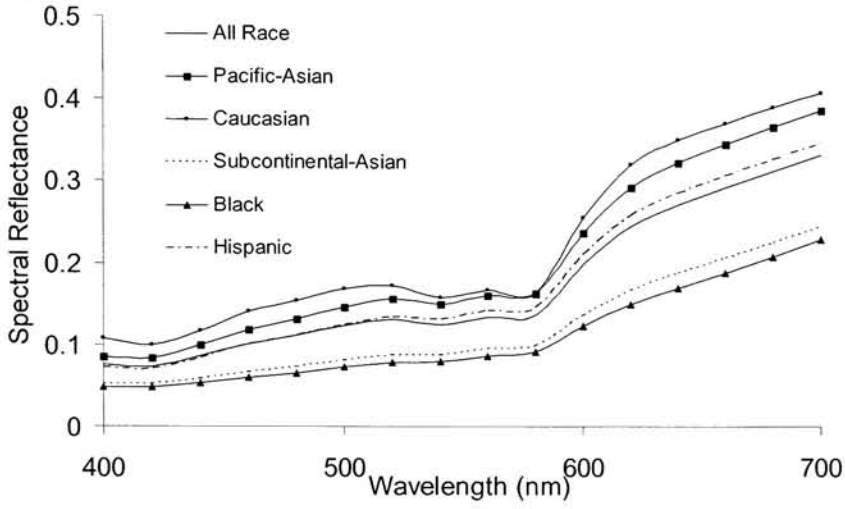

***Figure 3-16**. Mean skin spectral reflectances of individual races and all races.*

Fig. 3-16 shows that each race has roughly similar shape of mean skin spectral reflectance. However, the heavy pigmented races, Black and Subcontinental-Asian, mask most of the spectral characterization of hemoglobin and appear more nearly monotonically increasing, revealing the spectral characteristic of melanin in the visible range. Light pigmented races, Caucasian, Pacific-Asian and Hispanic, on the other hand, show apparent absorption bands of hemoglobin around 575nm, 540nm and 410nm. Those spectral characteristics are consistent with the results discussed in the introduction section. The cumulative contribution percentages of the first one to six basis functions of skin spectra for individual races are shown in Table 3-6. It shows that three basis functions will cover over 99.7% of variance of skin spectra for each race.

***Table 3-6**. Cumulative contribution percentage of principal components calculated from spectra of skin spectra for individual races. See text for abbreviations.*

Race	Number of Principal Components					
	1	2	3	4	5	6
PA	95.65	99.04	99.69	99.89	99.95	99.96
C	94.21	99.01	99.71	99.84	99.94	99.97
SA	97.36	99.34	99.78	99.98	99.99	99.99
B	97.77	99.60	99.92	99.98	99.99	99.99
H	96.40	99.45	99.82	99.97	99.98	99.99

The corresponding first three basis functions are shown in Fig. 3-17. Fig. 3-17 shows that for skin spectra, three light-pigmented races have very similar first three basis functions while the same is true for two heavy-pigmented races. However, it is obvious that the third basis functions of light and heavy pigmented races are different. This may be due to the fact that skin of heavy-pigmented races has a masking effect on spectral characterization of hemoglobin. Comparing basis functions based on spectra of all skin in Fig. 3-17(f) and basis functions based on all spectra of all races in Fig. 3-12(f) shows that the two sets of first three basis functions are very similar. This may be the reason why basis functions based on all spectra of all races can provide quite accurate color and spectral reproduction for spectra of skin, and vice versa.

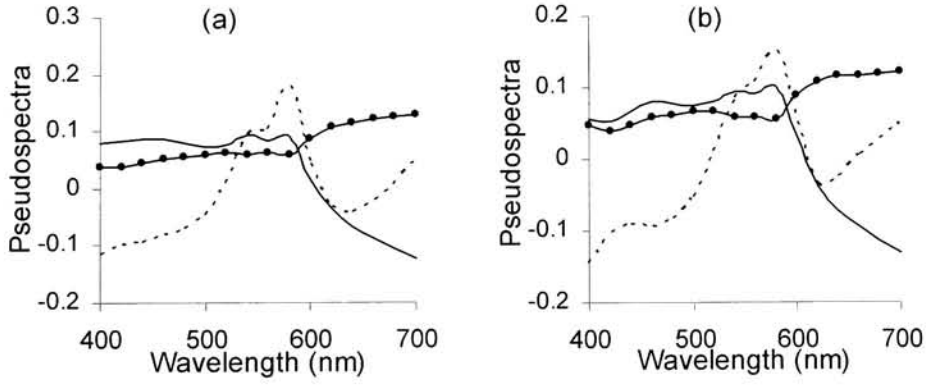

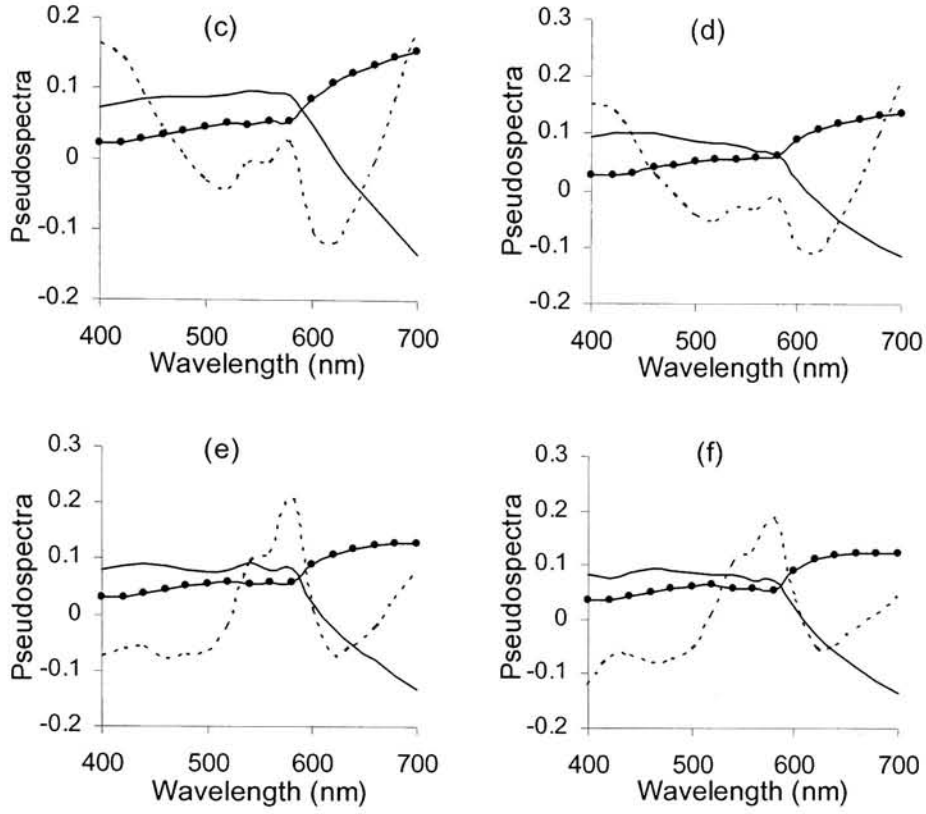

Figure 3-17*. Graphs of the first three basis functions for spectral reflectances of facial skin of individual races and all races. Solid-dot line is for the 1st component, solid line for the 2nd component and dot line for the 3rd component. (a) Pacific-Asian; (b) Caucasian; (c) Subcontinental-Asian; (d) Black. (e) Hispanic. (f) All Races.*

The results of color and spectral reproduction of skin for individual races when using 3 and 6 basis functions based on all spectra of all races are given in Table 3-7. It shows that three basis functions based on all spectra of all races will provide good color and spectral reproduction for light-pigmented skin (Pacific-Asian, Caucasian and Hispanic) while there are relatively large color difference and metameric indices, but still small enough for practical application, for heavy-pigmented skin (Black and Subcontinental-Asian). It also suggests that color and spectra reproduction will be improved when using more basis functions, especially for heavy pigmented skin.

Table 3-7. *Color differences and indices of metamerism in spectral reproduction of skin for individual races when using 3 and 6 basis functions based on all spectra of all races. (1) color difference; (2) indices of metamerism. See text for abbreviations.*

No.	PA	C	SA	B	H	AllSkin
3	0.53	0.67	0.83	1.17	0.53	0.75
6	0.16	0.20	0.11	0.08	0.17	0.15

(1)

No.	PA	C	SA	B	H	AllSkin
3	0.14	0.15	0.21	0.28	0.12	0.18
6	0.02	0.02	0.01	0.01	0.02	0.02

(2)

The spectral reflectances shown above were measured using remote-type method. It is worth doing some comparison with spectra measured by contact-type method from other researchers. Based on current available spectral data we will concentrate only on skin spectra. The skin spectra measured by contact-type method here are provided by Dr. Pietikäinen from Oulu University, Finland[65] and referred to as the Oulu data. The Oulu data contains 357 spectra measured from facial skin of 119 subjects with a Minolta CM-2002 spectrophotometer. Each subject provided 3 spectral measurements from the left and right cheek and the forehead. Details of the Oulu data are given in reference 64. The Oulu data are characterized into three races, Pacific-Asian, Caucasian and Black. There were 10 Pacific-Asian, 101 Caucasian and 8 Black subjects. The mean skin spectra of individual races in the Oulu data are shown in Fig. 3-18. Comparing Fig. 3-16 and Fig. 3-18, it shows that mean skin spectra of Oulu data are higher than mean skin spectra in our data for the same races. This is due to two major reasons. One is the different locations selected for spectral measurements. Our measurement selected more locations than the Oulu data measurement. The other reason is the different measurement geometries

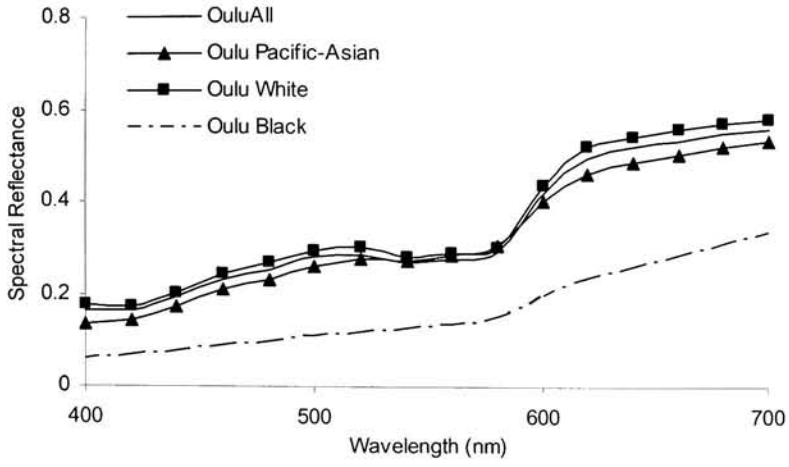

***Figure 3-18**. Mean spectra of skin for individual races in Oulu data.*

involved in the two data sets. Our spectral data contained various geometries while Oulu data contained only d/8 geometry.[66] It could also be partly due to the population difference in two measurements. Our data had spectra from 8 Caucasian, 11 Pacific-Asian and 7 Black subjects while these numbers were 101, 10 and 8 respectively for Oulu data. Fig. 3-18, like Fig. 3-16, shows apparent absorption bands of hemoglobin around 575nm, 540nm and 410nm for light pigmented races. first three basis functions of Oulu data are shown in Fig. 3-19.

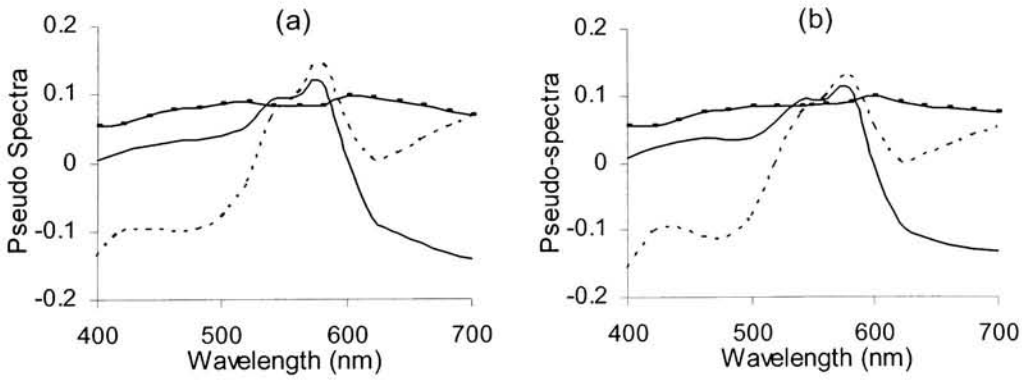

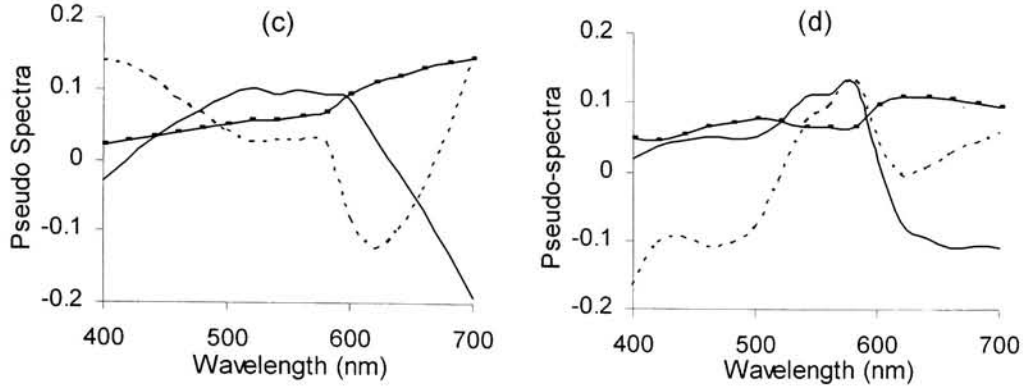

***Figure 3-19**. First three basis functions of skin spectra of individual races and all races in Oulu data. Solid-dot line is for 1st component, solid line for 2nd component and dot line for 3rd component. (a) Oulu Pacific-Asian; (b) Oulu Caucasian; (c) Oulu Black; (d) Oulu All.*

Comparing Fig. 3-17 and Fig. 3-19, it shows that basis functions of light-pigmented skin have very similar shapes while basis functions of heavy-pigmented skin, Black skin, have very similar shapes of their own.

***Table 3-8.** Cumulative contribution percentage of principal components calculated from spectra of skin spectra for individual races in Oulu data. PA is Pacific-Asian; C is Caucasian; B is Black; RA is all races.*

Race	Number of Basis Functions					
	1	2	3	4	5	6
PA	93.42	97.52	99.27	99.71	99.91	99.97
C	82.41	95.24	98.53	99.37	99.74	99.87
B	98.30	99.71	99.87	99.97	100.00	100.00
AR	94.20	98.45	99.60	99.81	99.92	99.96

The cumulative contribution percentages of the first one to six principal components of skin spectra for individual races in the Oulu data are shown in Table 3-8. Table 3-8 shows that the cumulative percentage using three basis functions for light pigmented races, Pacific-Asian and Caucasian, in Oulu data are relatively small compared to that of the spectral data in Table 3-6. Japanese skin spectra reported by Imai[1] has comparable

cumulative percentage using three basis functions with that of Pacific-Asian skin in our spectral data. The reason for this difference is unknown, but we presume that geometric difference may play a role.

For comparison purpose, we here also calculated the color differences applying various three basis functions shown in Fig. 3-12 to skin spectra in Oulu data. The results are shown in Table 3-9.

***Table 3-9**. Color differences of spectral reproduction for skin spectra of individual races And all races in Oulu data using different sets of three principal components. C is Caucasian; PA is Pacific-Asian; B is Black; All skin is all skin spectra in Oulu data.*

	C	PA	B	All Skin
C	**0.42**	0.56	3.89	0.45
PA	0.48	**0.26**	1.53	0.33
B	1.51	1.08	**0.85**	0.54
All Skin	0.50	0.57	3.45	**0.44**

Not surprisingly, basis functions based on all races will provide the best color reproduction for overall skin spectra. Also, like the results in Table 3-3, basis functions based on light pigmented skin cannot provide good color reproduction for heavily pigmented skin, and vice versa.

So far the color and spectral reproductions of skin spectral reflectances using different sets of basis functions based on statistical analysis have been discussed. One may want to know the deviation or degree of deviations of color within the skin spectral reflectances of individual races and individual subjects. Table 3-10 shows the mean color differences between the skin spectral reflectances and their mean spectra (shown in Fig 3-16 and Fig 3-18) of individual races.

Table 3-10. *Mean, maximum, minimum and standard deviation of color difference values calculated between skin spectral reflectances and their corresponding mean skin spectra in individual races. See text for abbreviations.*

	Mean	Max	Min	Std
C	5.07	12.33	1.03	2.55
PA	6.48	17.48	1.15	3.31
B	6.99	18.81	1.03	4.03
SA	5.97	27.98	0.67	4.33
H	5.22	15.55	1.03	3.4
Oulu PA	2.98	7.54	0.65	1.64
Oulu B	5.70	15.87	0.24	3.86
Oulu C	3.48	11.98	0.60	1.94

Table 3-11. *Results of mean, maximum and minimum color difference values calculated from each pair of skin spectral reflectances of each subject within individual races. See text for abbreviations.*

	Mean	Max	Min
C	6.25	17.66	0.32
PA	7.05	19.59	1.56
B	8.09	27.04	0.83
SA	7.95	30.40	0.65
H	6.73	11.94	1.56
Oulu PA	3.96	8.07	0.61
Oulu B	3.13	7.53	0.87
Oulu C	3.34	12.52	0.41

It also provides the standard deviation, maximum and minimum values of those color differences. Table 3-11 also provides the results of mean color difference, but with different approach. The color differences of each different pair of skin spectral reflectances of each subject are first calculated. Then the mean of those color differences within individual races are calculated. It also provides the maximum and minimum values of those color differences. The results of table 3-10 show that the deviations of color perception between the skin spectral reflectances and their mean spectra within

individual races are very large, over unit 5 in our data and over 3 in Oulu data. The relatively small mean values of Oulu data sets are probably due to their fewer sampling points. It can also indicate that the variation of skin color perception of Pacific-Asian is the smallest. Table 3-11 shows that the deviation of facial skin color perception is very large even within a single subject, which may be one of the reason that people can be distinguished easily one another from their facial skin features. Oulu data sets show the relatively small values with the same reason as discussed for table 3-10. Considering the large variation of facial skin color in tables 3-9 and 3-10, it, in other hand, proved that color reproductions of skin (see results in table 5) using three basis functions derived from all spectral reflectances measured are accurate enough in practical application.

3.4.4 Summary

The PCA results showed that the first three basis functions will provide quite accurate color and spectral reproduction for spectra of all races and individual races and individual facial parts as well. Considering color reproduction of spectral reconstruction using three basis functions in each race, the set of basis functions based on spectra of Pacific-Asian will provide the best overall results. However, from spectral matching point of view, three basis functions based on all spectra will provide the best spectral reproduction with minimum overall mean value of indices of metamerism. Further observation indicates that more basis functions may be necessary to improve the color and spectral reproduction of facial spectral reflectances of heavy- pigmented races and hair in facial part. Therefore, in the following research we will apply first three and first six basis functions based on all spectra.

Spectral reflectances of skin measured from remote-type of this research and contact-type of the Oulu data show very similar statistical characterizations though there are some differences in absolute values due to different measurement geometries and selection of measurement location involved. Considering the colors of facial skin, the deviations are very large either in the same race or the same subject with different facial parts.

The results of color and spectral reproduction using different sets of basis functions discussed above may suggest that a universal set of basis functions of human facial spectral reflectances of various ethnic races is possible, especially for the spectra of human facial skin.

Those results will provide us practical suggestion for imaging or spectral imaging system design, especially imaging system for human portraiture. It may also have potential application to designing digital camera system, i.e., optimizing the selection of spectral sensitivities of digital camera to provide best color reproduction of human face images. Based on our results it may help us to choose optimized sets of inks to print images of human faces with better color and spectral reproduction. It may also provide some practical data for the cosmetic industry.

3.5 Estimating Spectral Image

The flow chart of a typical method to estimate the tristimulus values from camera signals is shown in Fig. 3-20. Details of the procedures are given in the following sections.

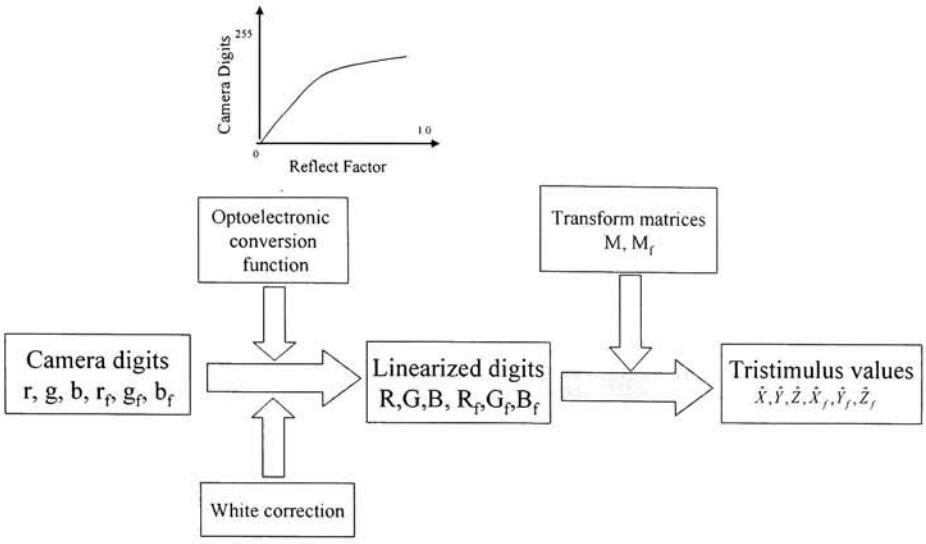

***Figure 3-20**. Flow chart of estimating the tristimulus values from camera signals*

3.5.1 Linearization and White Correction

As mentioned in Chapter 2, to connect camera digits to the tristimulus values, the digits should be first linearized based on the optoelectronic conversion function (OECF). The method of one-dimensional look-up table involving interpolation was employed in this research.

The original images, both without and with external filter, were first transformed to the reflectance factor space, pixel by pixel, based on the OECF. White correction was then required to be performed due to non-uniform illumination fallen on the subjects. Compared to the depth dimensions of the subjects, the distance from subject to the camera could be regarded as infinity. Therefore, it was reasonable to assume here that the subjects could be treated as flat objects. Thus, normal flat field procedure could be applied. The equation for white correction is given in Eq. 3-1.

$$Image_{wc}=(W_{mean}-D_{mean})\cdot(Image_{lin}-Dark_{lin})/(White_{lin}-Dark_{lin}), \qquad (3\text{-}1)$$

where $Image_{lin}$ is input linearized image, $Image_{wc}$ is image after white correction, $White_{lin}$ and $Dark_{lin}$ are linearized white image and dark image respectively, W_{mean} and D_{mean} are mean values of $White_{lin}$ and $Dark_{lin}$ respectively.

Then the pixels that contributed to the spectral measurement were truncated from the linearized image. The mean digital counts of those truncated pixels of red, green and blue channels were linearized R, G and B digital counts. For simple purpose, in the following sections we will use R, G and B notations to represent the linearized digital counts of red, green, and blue channel images, without using extra external filter, respectively. The linearized digital counts from images using external filter will be represented as R_f, G_f and B_f corresponding to red , green and blue channels respectively. The linearized digital counts were values within [0, 1]. The next step was to determine the transform matrix that could transfer the linearized digital counts to the eigvenvalues. Using the eigvenvalues and basis functions, the spectral reflectance could be constructed.

3.5.2 Transform Matrix

To transform linearized digital counts to tristimulus values, a transform matrix is required. Determining the transform matrix is an important procedure in whole spectral imaging system calibration. Since most digital cameras do not have spectral sensitivities that are linearly related to color-matching functions, a simple 3x3 transformation will yield considerable error. A common empirical technique recommended by Berns[63] is to include relative cumbersome square and covariance terms, or even higher order terms. The possible transform equation then could be written as in Eq. (3-2):

$$\begin{bmatrix} \hat{X} \\ \hat{Y} \\ \hat{Z} \end{bmatrix} = \mathbf{M} \cdot \begin{bmatrix} R \\ G \\ B \\ R^2 \\ G^2 \\ B^2 \\ R \cdot G \\ R \cdot B \\ G \cdot B \end{bmatrix}, \qquad (3-2)$$

where R, G and B are linearized digital counts of camera, $\hat{X}, \hat{Y}$ and $\hat{Z}$ are estimated tristimulus values , **M** is the transform matrix. The transform matrix M can be calculated from least square regression known as pseudoinverse method based on calibrated targets. The author call this procedure as 2-step method that it first relates the digits to the tristimulus values using Eq. (3-2), then determine the eigenvalues using Eq. (2-21). However, least square regression of **M** only minimizes the sum of square tristimulus errors; it has no guarantee to either provide minimum color difference or most accurate spectral fit. Therefore, to achieve the best accuracy of the final results, some necessary optimization should be performed to minimize the goal object which is of most important or interest. For example, the **M** matrix can be determined with the minimum of maximum color difference or, in spectral image research, with the minimum root mean square error between estimated and measured spectra. It is worth noting that it works best to use a different transform matrix for each different sets of filters.

An alternative method is to establish the relationship between linearized digital counts and eigenvalues directly. This method is called a direct method. The form of digits chosen can be based on the Eqs. (2-21) and (3-2). The accuracy of 2-step method and

direct method depends on certain situations; no one always works better than the other. In the following we will only provide the results using direct method. For simple demonstration, we here define matrix **D** as follows:

$$\begin{aligned} \mathbf{D} &= [\mathbf{D1} \quad \mathbf{D2} \quad \mathbf{D3} \quad \mathbf{I}], \\ \mathbf{D1} &= [\mathbf{R} \quad \mathbf{G} \quad \mathbf{B}], \quad \mathbf{D2} = [\mathbf{R}\cdot\mathbf{G} \quad \mathbf{R}\cdot\mathbf{B} \quad \mathbf{G}\cdot\mathbf{B} \quad \mathbf{R}^2 \quad \mathbf{G}^2 \quad \mathbf{B}^2], \\ \mathbf{D3} &= [\mathbf{R}\cdot\mathbf{G}\cdot\mathbf{B} \quad \mathbf{R}^2\cdot\mathbf{G} \quad \mathbf{G}\cdot\mathbf{B} \quad \mathbf{B}^2\cdot\mathbf{R} \quad \mathbf{R}^3 \quad \mathbf{G}^3 \quad \mathbf{B}^3] \end{aligned} \qquad (3-3)$$

where, **R**, **G**, and **B** are linearized digital count matrices without external filter, **I** is the unit matrix for offset. Similar expressions can be written for matrix $\mathbf{D_f}$ as the case using filter. Therefore, **D** and $\mathbf{D_f}$ both contain 17 terms. We will use the expression **Q=[D**(n1:n2)] to represent the new matrix **Q,** a sub-matrix of **D,** containing column n1 to n2 of **D**. When using three basis functions, two different digital count matrices were used to determine corresponding different transform matrices:

$$\begin{aligned} &\textit{7 terms}: \quad \boldsymbol{Q} = [\boldsymbol{D}(1{:}6) \quad \boldsymbol{D}(17)], \\ &\textit{17 terms}: \quad \boldsymbol{Q} = \boldsymbol{D}. \end{aligned}$$

When using 6 basis functions, due to noise issue involved in final spectral image reproduction, only low order of digital count matrix was considered. The new digital count matrix here had 7 terms as followings

$$\textit{7 terms}: \quad \mathbf{Q} = [\boldsymbol{R} \quad \boldsymbol{G} \quad \boldsymbol{B} \quad \boldsymbol{R_f} \quad \boldsymbol{G_f} \quad \boldsymbol{B_f} \quad \boldsymbol{I}],$$

where $\mathbf{R_f}$, $\mathbf{G_f}$, and $\mathbf{B_f}$ are linearized digital count matrices with external filter.

After digital count matrices were determined, the corresponding transform matrices could be obtained using Eq. (3-4) and Eq. (3-5).

$$\boldsymbol{\alpha} = \boldsymbol{Q}\cdot\boldsymbol{M}, \qquad (3\text{-}4)$$

$$\boldsymbol{M} = (\boldsymbol{Q}\cdot\boldsymbol{Q}^T)^{-1}\cdot\boldsymbol{Q}^T\cdot\boldsymbol{\alpha}, \qquad (3\text{-}5)$$

where α was an n×p eigenvalue matrix obtained from PCA method using p basis functions for whole n spectra, $\boldsymbol{Q}$ was an n×m matrix of linearized digital counts with m terms, and $\boldsymbol{M}$ was an m×3 transform matrix. Here, n is 544 for all spectral data sets. Once the transform matrix was determined, the digital counts in each pixel of the linearized image could then be transformed to eigenvalues using Eq. (3-4), hence, construct the spectral reflectance at this pixel by using Eq. (2-5). The spectral image, therefore, was obtained.

As indicated in previous section, the least square regression using Eq. (3-2) may not give optimal spectral fit. Therefore, to determine the optimized transform matrix, we first, in 2-step method, applied Eq. (3-2) to obtain the least square result of transform matrix, **M**. Then using this M as an initial matrix, we performed optimization procedure to minimize the error of spectral estimation. The optimization criterion here is to minimize the root mean square of error between measured and estimated spectral reflectance. On the other hand, in direct method, the transform matrix is based on the spectra directly; matrix obtained from least square regression in direct method has already satisfied the minimizing of root mean square error between spectra, measured and estimated.

3.5.3 Modeling Accuracy

To demonstrate the spectral fit, the indices of metamerism were calculated using illuminations D50 and A. This calculation employed Fairman's [78] metameric correction using parameric decomposition. The results of color and spectral reproductions using different terms of transform matrices and different number of basis functions for all spectral reflectances measured are given in Table 3-12 where 3P7T and 3P17T represent

the using of 3 basis functions with 7 terms (including covariance terms) and 17 terms (with higher order terms) of digital counts involved in calibration regression respectively and similar definition for 6P7T using 6 basis functions. It should be noted that six gray scale targets were added into the data sets to determine the transform matrices though the basis functions were still only based on spectral reflectances of the human faces. The reason to do this was to improve the color and spectral reproduction in gray scales while unchanging the quality of color and spectral reproduction for the face.

Table 3-12. *Results of color and spectral reproductions using different transform matrices in system calibration.*

Method	DeltEab	Meta_Index	RMS
3P7T	2.68	0.73	0.012
3P17T	2.32	0.66	0.011
6P7T	1.76	0.48	0.010

The results in Table 3-12 indicate that three basis functions will provide acceptable color and spectral reproduction after the calibration. More terms involved in regression of transform matrices or more basis functions used will provide more accurate color and spectral reproduction. For test purpose 16 trial sets of spectral data and corresponding camera digits measured from a subject whose data were not involved in the system calibration were used. Table 3-13 provides the modeling results for the trial sets of data. Table 3-13 shows that for these particular sets of data, when using 3 basis functions, more terms of transform matrix did not provide more accurate color or spectral reproduction though overall color and spectral reproduction did have been improved. However, it was still true that using more basis functions improved the accuracy of color and spectral reproduction.

Table 3-13. *Results of color and spectral reproductions for the trial sets of data using different transform matrices in system calibration.*

Method	DeltEab	Meta_Index	RMS
3P7T	2.01	0.49	0.013
3P17T	2.02	0.58	0.014
6P7T	1.58	0.43	0.012

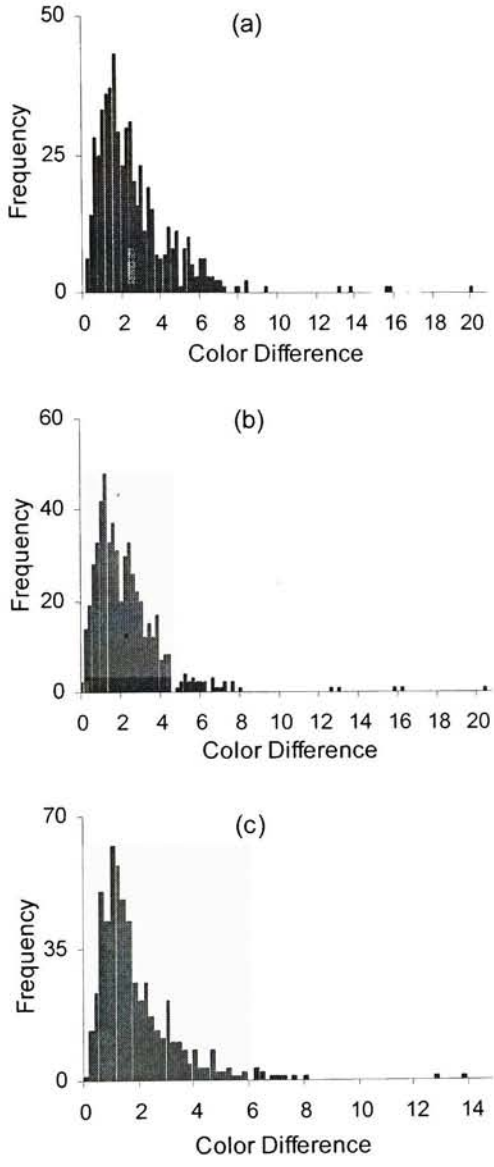

Figure 3-21. *Histograms of color differences in modeling. (a) for 3P7T; ((b) for 3P17T; (c) for 6P7T.*

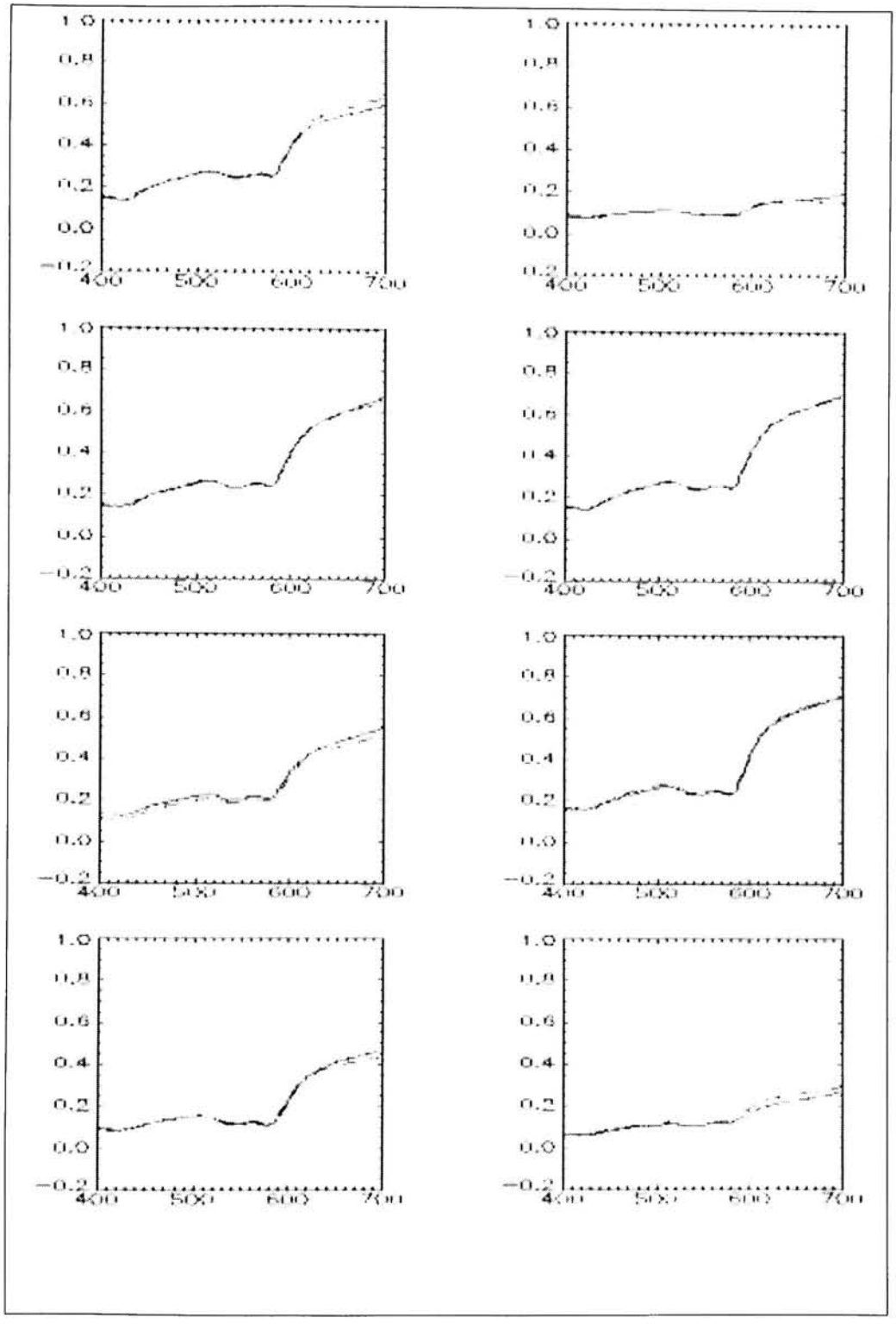
1.0
0.8
0.6
0.4
0.2
0.0
−0.2
400
500
600
700

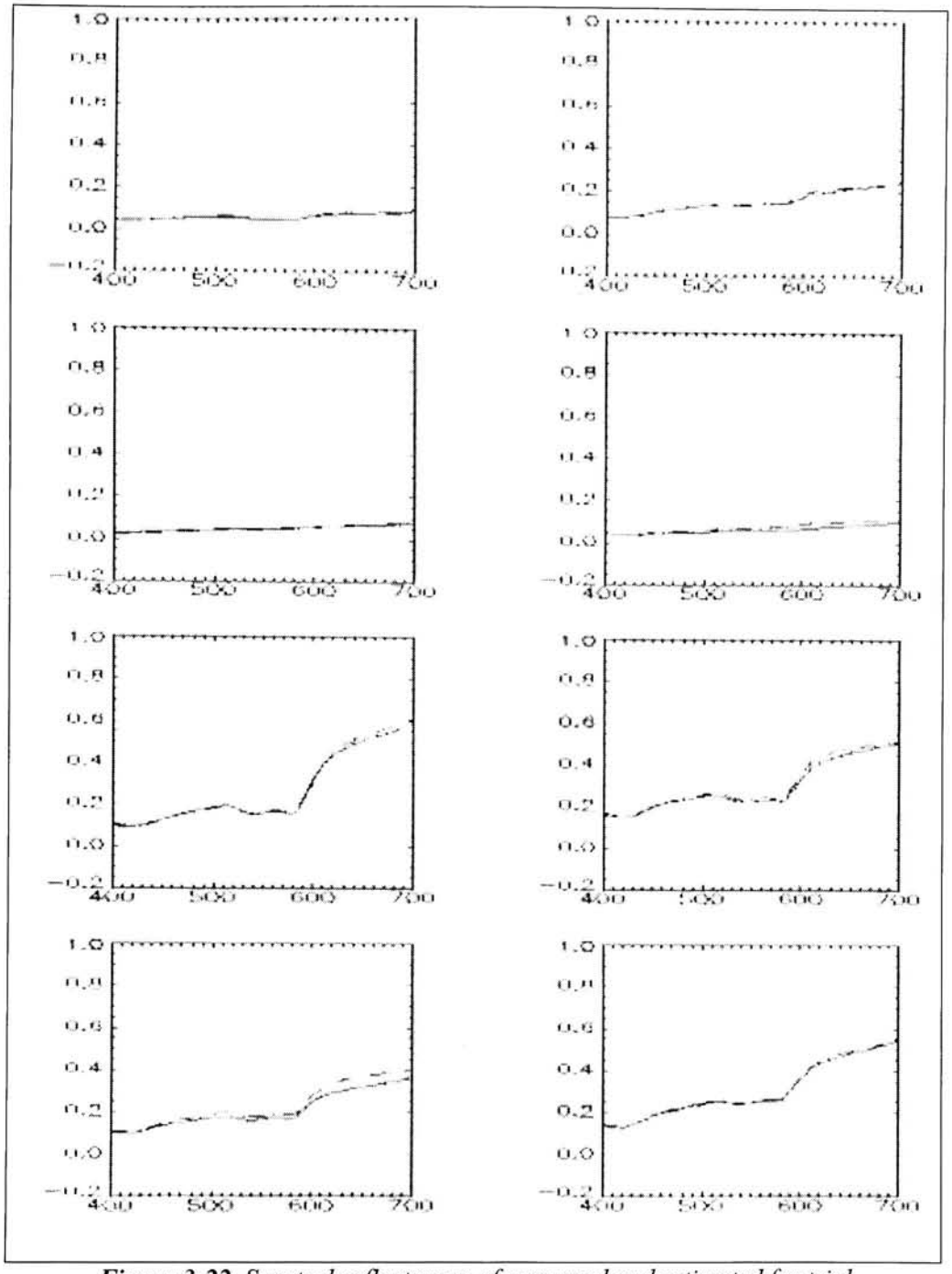

***Figure 3-22**. Spectral reflectances of measured and estimated for trial sets of data using 3 basis functions with 7 terms of transform matrix. The abscissa is the wavelength in the unit of nm, the ordinate is the spectral reflectance factor.*

To demonstrate the distribution of color differences in system calibration, histograms of color differences are shown in Figure 3-21. Histograms show that most color differences fell around ΔE^*ab of 2, especially using higher order of terms or more basis functions. However, some color differences did fall away from acceptable range and are more than 10 unit of ΔE^*ab. Treatment of those large errors of reproduction is in the image quality section.

To demonstrate the spectral match between the measured and reproduction, Fig. 3-22 shows the measured and estimated spectral reflectances for 16 trial sets of data.

Once transform matrices were determined, the spectral reflectances could be estimated, pixel by pixel, from the original images, hence, obtained the spectral images. For display, the spectral reflectance of each pixel in those spectral images estimated was converted to CRT digits for display.

3.5.4 Spectral Image Display

Applying the transform matrices obtained above, the spectral images, using either 3 or 6 basis functions, can be estimated, pixel by pixel, from the original R, G and B channel images. Each pixel of spectral image contains the eigenvalues which can be used to reconstruct the whole spectral reflectance, of this pixel, using Eq. (2-5). Therefore, once the illuminant spectra and observer are given, the tristimulus values of each pixel can be determined. Applying some color models, those tristimulus values will be transferred to digital counts of display device, i. e., monitor, for display. More complete and complex models can be found in the book written by Fairchild.[47] Relatively simple color models and straightforward procedure were selected to achieve this. The procedure will be

described briefly as follows. All those transforms were processed pixel by pixel. When using 6 basis functions, the image registration procedure was required to be performed on the two images obtained with and without using the external filter before any transform could be performed.

It was assumed that subject was illuminated by illuminant D50 and the observer was CIE 1931 standard observer. It was also assumed that the display had a white point equal to the chromaticities of illuminant D65. The display environment had illumination close to D65. Therefore, the Bradford[80] chromatic adaptation transform was first applied to transfer the tristimulus values from illuminant D50 to illuminant D65. Then the sRGB[67] model was used to convert the tristimulus values, in illuminant D65, to display R, G and B values. Finally, we applied CRT characterization model [68] to transform the R, G and B values to digital counts which are values of 0~255. Those digital counts are final, reconstructed image values for display. Some mapping process may need to keep the transferred values within the device profiles. For more accurate display of reconstructed spectral image, the CRT need to be calibrated based on its colorimetric characterization.[69] Detail procedure and mathematical equations will be given in Appendix B. By making a comparison between images displayed and real subjects, we found the results as follows:

(1) When using three basis functions, the transform matrix with 17 terms was more flexible and would provide more accurate color reproduction than low order transform matrix did, especially the highlight in the eyes, dark background and hairs. The matrix also predicted the colors in details very well. Moreover, the matrix could also interpolate colors of other materials, such as glasses, clothes, very well though no such spectra

involved in system modeling. It was not obvious that the transform matrix with 17 terms, would yield the least color shift, to blue, in the highlight of eyes. Meanwhile, transform matrix with 7 terms could not extrapolate colors very well; it failed to predict the highlight in the eyes. Compared to the reproduced image using transform matrix with 17 terms, reproduced images with 7 term transform matrix were little bit blurred. Considering the image noise, it was shown, though not obviously, that higher order transform matrix would yield slightly more image noise. This effect was also reported by Burns.[9]

(2) When using 6 basis functions, the displayed image showed, obviously, that there was more prevalent image noise, especially in the image using a higher order transform matrix. The image noise came mainly from the original image using the external filter causing relative low signal-noise ratio. This also implied that the image quality of this camera was not good enough for accurate multi-spectral image research. In addition, when using 6 basis functions, the noise effect was very obviously impacted by high order transform matrices. However, it also showed that transform matrix with 7 terms could predict the color very well, either the highlight in the eyes, dark background, or color details in the face. Some samples of original captured RGB images and their reconstructed rendering spectral images are shown in the following figures. For simple notation, Fig. 3-23 to Fig. 3-27 will use the same arrangement as shown in the followings:

Original image without filter		Original image with filter
Spectral image 3P7T for rendering	Spectral image 3P17T for rendering	Spectral image 6P7T for rendering
3P7T enlarged image region for noise detail	3P17T enlarged image region for noise detail	6P7T enlarged image region for noise detail

The samples of original RGB images and corresponding estimated rendering spectral images from a Pacific-Asian subject, a Caucasian, a Black, a Subcontinental-Asian and a Hispanic are shown in Fig. 3-23 to Fig. 3-27 respectively. The rendering spectral images given in Fig. 3-23 to Fig. 3-27 show that, spectral images of 3P7T are little blurred and have small color shift. Spectral images of 6P7T have more image noise. This is partly due to the fact that the camera we used had more noise, especially in blue channel image. Spectral images of 3P17T would be the best with more accurate color and spectral reproduction compared to spectral images of 3P7T, and less image noise compared to spectral images of 6P7T.

***Figure 3-23**. Original RGB images, estimated rendering spectral images and enlarged image details of eye region from a Pacific-Asian subject.*

Figure 3-24. *Original RGB images, estimated rendering spectral images and enlarged image details of nose region from a Caucasian subject.*

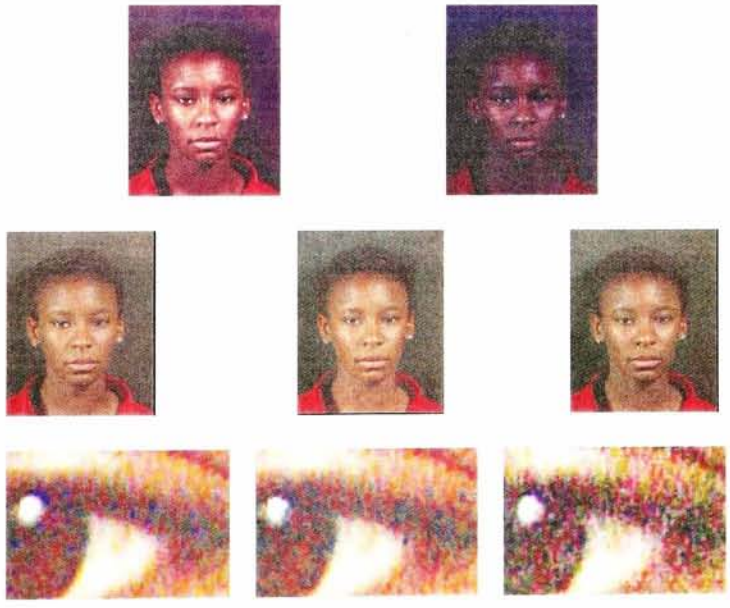

Figure 3-25. *Original RGB images, estimated rendering spectral images and enlarged image details of eye region from a Black subject.*

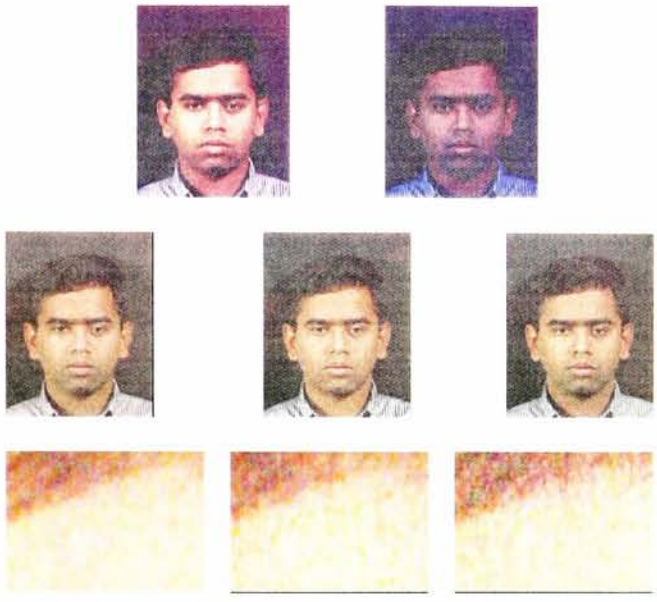

***Figure 3-26**. Original RGB images, estimated rendering spectral images and enlarged image details near nose region from a Subcontinental-Asian subject.*

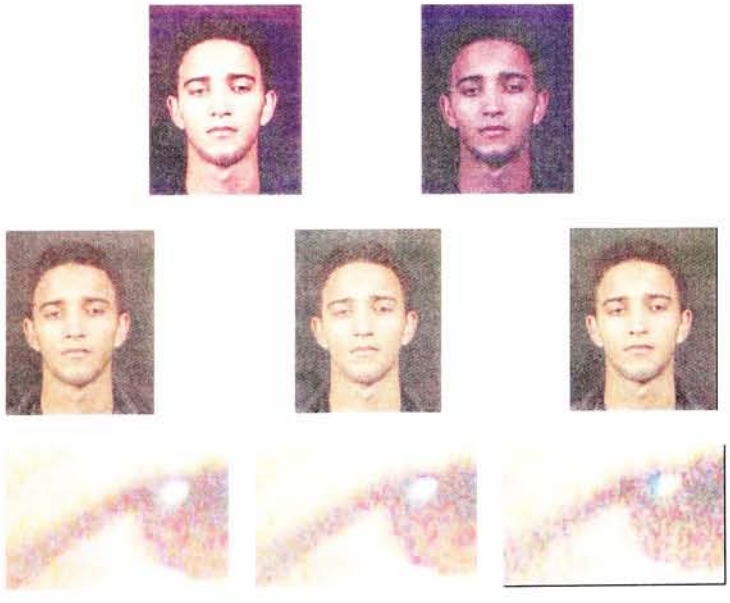

***Figure 3-27**. Original RGB images, estimated rendering spectral images and enlarged image details of eye region from a Hispanic subject.*

To check the flexibility of the system calibration, the author took his own spectral image when wearing the glasses. The original images, with and without filter, and corresponding estimated spectral images using 3P7T, 3P17T and 6P7T are shown in Fig. 3-28. Fig. 3-28 proves that this imaging system was quite flexible and could interpolate or extrapolate the color of glasses and clothes very well.

***Figure 3-28**. Original RGB images and estimated spectral images for display from author wearing glasses.*

3.5.5 Noise Discussion

Image noise is a main issue that impacts the final image quality of the spectral images. At this experiment, the main noise came from the thermal and electronic noise of the CCD camera. The lighting system made the signal-noise ratio in blue channel even worse. Due to the noise propagation in color transformation,[9] generally speaking, more basis

functions or more terms of transform matrices involved in spectral estimation will cause more noise in the final spectral images, hence impact the image quality. Therefore, one should balance between the color and spectral accuracy in system calibration and image quality of final spectral image due to the existing of image noise and error involved in the imaging system. We will discuss more detail about the image quality of spectral imaging system in the image quality chapter.

3.6 Summary

A new procedure for capturing spectral image of human portraiture has been proposed. The facial spectral reflectances obtained were analyzed by PCA method. The PCA results indicate that three basis functions will provide quite accurate color and spectral reproduction for facial spectral reflectances from various races and different parts. Three band and six band spectral images of human portraits have been successfully obtained. High order transform matrices will provide more accurate, three-band, spectral images with acceptable image noise. However, for six-band spectral images, transform matrix with low order of 7 terms will give most acceptable results. Due to the limit of image quality of the camera used, the 6-band spectral image did not meet the quality we originally expected. To obtain more accurate, multi-spectral image, a camera with high quality in terms of noise is required. The obtained spectral image can be applied to color-imaging system design and analysis.

4 IMAGE QUALITY ANALYSIS OF SPECTRAL IMAGE

The procedure to capture spectral images of human portraits was described in the previous chapter. Different algorithms and transform matrices for estimating the spectral images were also described. So far, all those considerations are based on the color or spectral accuracy at the stage of system calibration. Little has been discussed on the quality of final spectral images. However, a spectral image, sooner or later, needs to be finally displayed for people to see. Therefore, image quality has to be considered when designing a spectral imaging system. In the following sections of this chapter we will investigate the image quality of spectral imaging system. The digital cameras and their responses to outside scenes were simulated based on real camera systems. A visual image quality experiment was performed to judge the image quality of spectral images with different distortions. Efforts were made to relate the results of visual experiment and objective measures of image quality and determine an image quality metric. Based on this image quality metric some further analysis of the spectral imaging system was performed.

4.1 Simulation of Spectral Imaging System

Computer simulation was applied to investigate the image quality of spectral imaging systems. The spectral imaging systems were simulated based on their real characteristics. Two real digital camera systems were used in this research. One is the SONY DKC-ST5 digital camera used in the previous experiment mentioned in chapter 2. Another one is IBM Research Pro/3000 Digital Camera System[70, 71] that researchers in MCSL applied

for spectral imaging of artwork.[72] The SONY DKC-ST5 camera system has been described in chapter 2. The IBM Research Pro/3000 camera system is described here.

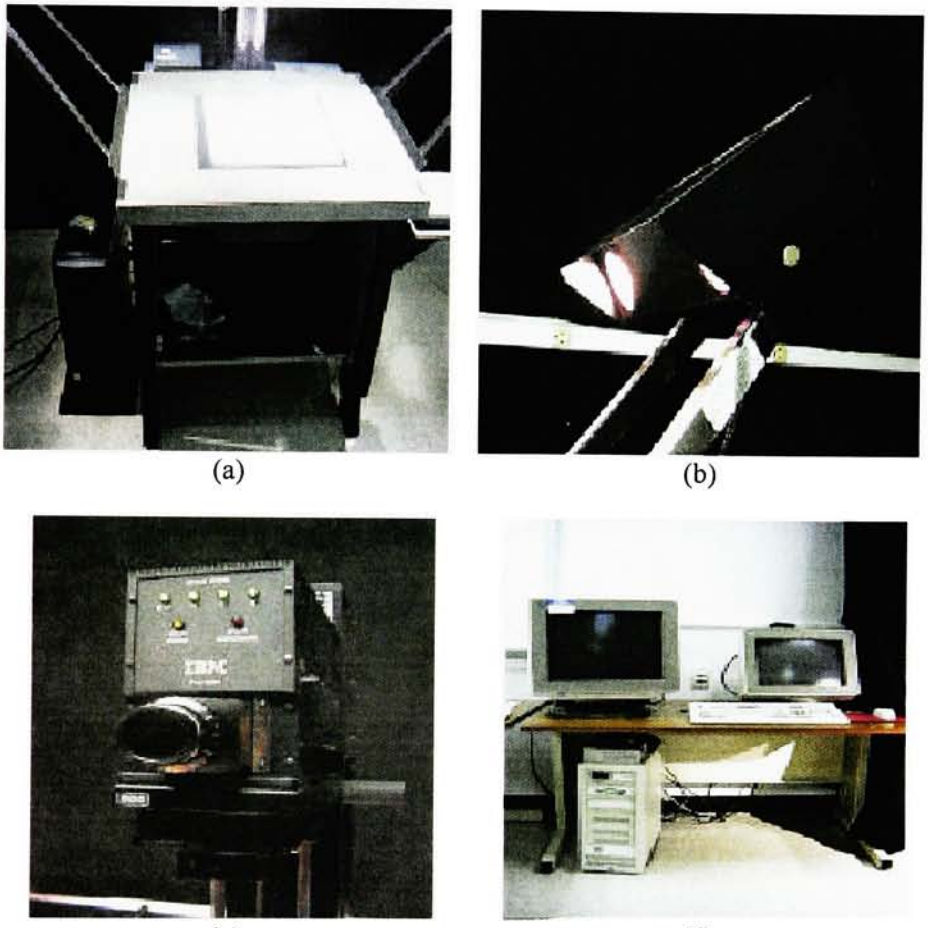

Figure 4-1. *IBM Research Pro/3000 system. (a) copy stand and controller; (b) side lamps; (c) scanner head and column; (d) PC and color monitor.*

4.1.1 IBM Research Pro/3000 Camera System

The IBM Research Pro/3000 is composed by copy stand, side lightings, scanner head, column and a controller that connected to a PC and a high resolution color monitor. The whole system is shown in Fig. 4-1.

The IBM Research Pro/3000 provides 3,072×4,096 or 2,048×3,072 pixels by a camera mounted on a variable height copy stand with both reflective and transmissive illumination. A CCD image sensor is mounted on a moving slide located inside the scanner head. A color filter wheel with 5 positions of dark, clear, red, green and blue is used to filter the incoming imaging light. With proper setting, it can produce raw color images with 12 bit for each red, green and blue channel. With 12 bit quantization, the IBM DCS Pro/3000 displays very good linear characteristics in OECF. Fig. 4-2 shows an example of the relationship between digital counts of gray patches of GretagMacbeth ColorChecker and luminance, Y, at red channel when using 12 bit quantization.

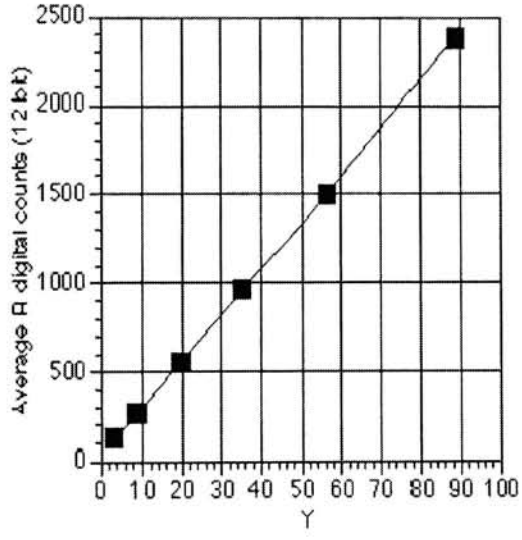

Figure 4-2. *Optoelectronic conversion curve for 12 bit quantization at red channel.*[72]

The IBM Pro/3000 uses four halogen light bulbs (Sylvania J688 ENH, 350W/120V, color temperature of 3,200K) as side lamps as shown in Fig. 4-1(b) giving imaging illumination configuration of 45/0. The absolute spectral radiant power of the illuminant is shown in Fig. 4-3.

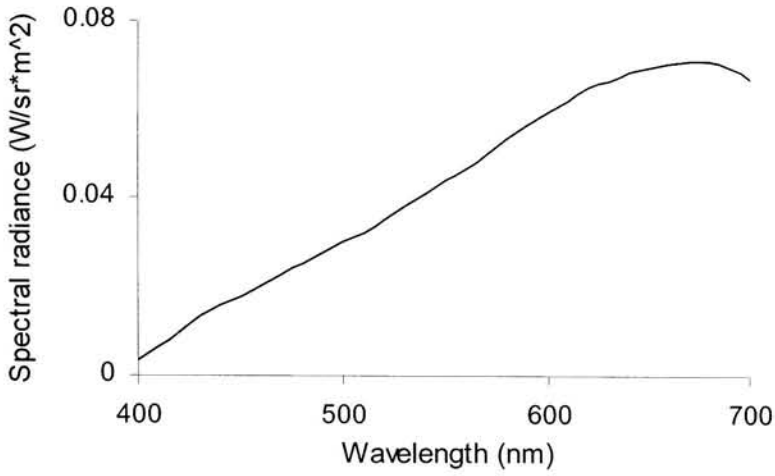

Figure 4-3. *Absolute spectral radiant power of IBM Research Pro/3000 side lamps.*

The normalized spectral sensitivities of R, G, and B channels[72] measured by double monochromator method are shown in Fig. 4-4.

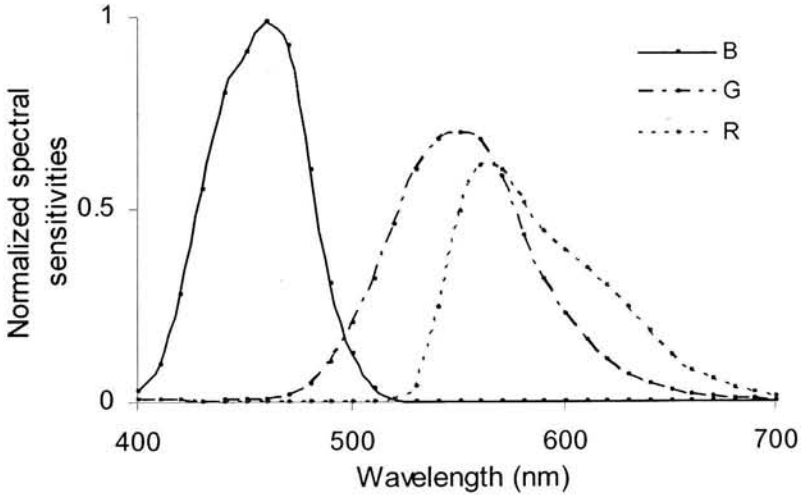

Figure 4-4. *Normalized spectral sensitivity of IBM Research Pro/3000 camera*

It should be noted here that the measured spectral data in Figs. 4-3 and 4-4 were provided as a courtesy by Dr. Imai. The details of measurement can be found in the reference 72. According to author's personal discussion with Dr. Imai and the results

shown in the reference 62, the simulation of the camera responses using the camera spectral sensitivities as shown in Fig 4-4 agreed with the real responses very well. Also, a simple 3×3 transform matrix can convert digital counts to tristimulus values very accurately. Therefore, in the following several sub-sections we will mostly concentrate on describing simulation for digital camera DKS-ST5 in human facial spectral imaging.

4.1.2 Simulation of Gray Scale Response

To perform a better computer simulation for spectral imaging systems and based on the results we previously obtained, some modifications were applied into image processing procedures. The first one was adding one more interpolation to obtain better linearization after flatting field procedure. The linearization was performed based on CECF curves. As described in section 3.2.3, the CECF was calculated without white correction since white correction, theoretically, can only be applied in the linear space. Therefore, some small difference between reflectance factors and linearized digits of gray scales which contributed to the CECF would be produced. To verify this, we performed linearization for the gray scale targets, Kodak Gray Scale Q14, in the same center, 31×41 pixels, as in calculating CECF at section 3.2.3 and obtained the mean linearized digits which, by definition, should be the same values of reflectance factors. The reflectance factors of gray scale Q14 (adding a high quality white as in section 3.2.3) and the corresponding calculated mean linearized digits for RGB channels are given in table 4-1. In table 4-1, *Ref. factors* represent the reflectance factors, *R_lin*, *G_lin*, and *B_lin* are linearized digits of corresponding gray scales in RGB channels respectively, *ErrorR*, *ErrorG*, and *ErrorB* are percentage errors between reflectance factors and corresponding linearized digits at

RGB channel respectively. The mean percentage errors are 3.54%, 2.72% and 3.06% for RGB channels respectively. Table 4-1 indicates that there are very large errors when estimating the dark targets though the overall mean errors for whole gray scale range are within practical tolerances.

***Table 4-1**. Linearized digits of Gray Scale Q14 and corresponding percentage errors to the reflectance factors.*

Ref. factors	R_lin	G_lin	B_lin	ErrorR (%)	ErrorG (%)	ErrorB (%)
0.9404	0.9401	0.9398	0.9393	0.03	0.06	0.09
0.8968	0.8940	0.8948	0.8919	0.31	0.22	0.24
0.6917	0.6914	0.6904	0.6903	0.04	0.18	0.15
0.5358	0.5371	0.5340	0.5357	0.24	0.34	0.26
0.4349	0.4358	0.4370	0.4415	0.21	0.48	1.31
0.3422	0.3395	0.3410	0.3398	0.81	0.36	0.10
0.2696	0.2692	0.2709	0.2751	0.13	0.51	2.18
0.2109	0.2107	0.2107	0.2089	0.13	0.12	0.83
0.1712	0.1691	0.1700	0.1698	1.24	0.67	0.41
0.1347	0.1333	0.1346	0.1330	1.05	0.13	0.27
0.1056	0.1043	0.1057	0.1051	1.19	0.10	0.76
0.0847	0.0837	0.0845	0.0834	1.16	0.24	0.32
0.0692	0.0677	0.0688	0.0677	2.08	0.58	0.09
0.0537	0.0529	0.0526	0.0520	1.49	2.07	1.65
0.0434	0.0420	0.0430	0.0406	3.33	0.87	3.31
0.0340	0.0330	0.0336	0.0318	2.76	1.01	3.71
0.0298	0.0279	0.0296	0.0286	6.52	0.59	2.65
0.0217	0.0203	0.0208	0.0199	6.37	4.11	2.07
0.0170	0.0151	0.0157	0.0153	11.12	8.07	0.81
0.0135	0.0117	0.0119	0.0135	13.80	12.06	15.69
0.0115	0.0092	0.0087	0.0101	20.35	24.25	9.45
Mean				**3.54**	**2.72**	**2.21**

The interpolation to improve the accuracy of gray scale linearization is based on a simple one-order linear regression as the form of y=a + b·x. The resulted interpolation equations after least square regression for RGB channels are shown in Eq. 4-1 to Eq. 4-3 respectively.

$$R_{\text{int}} = 0.00127 + 0.99919 \cdot R_{lin}, \qquad (4-1)$$

$$G_{\text{int}} = 0.00055 + 1.00033 \cdot G_{lin}, \qquad (4-2)$$

$$B_{\text{int}} = 0.00078 + 1.00010 \cdot B_{lin}, \qquad (4-3)$$

where R_{lin}, G_{lin}, and B_{lin} are linearized digits for RGB channels respectively, R_{int}, G_{int}, and B_{int} are corresponding interpolated digits in reflectance space for RGB channels respectively. The improved results of gray scale after applying Eq. 4-1 to 4-3 are shown in Table 4-2 where R_int, G_int and B_int are interpolated digits of corresponding gray scales in RGB channels respectively, ErrorRint, ErrorGint, and ErrorBint are percentage errors between reflectance factors and corresponding interpolated digits at RGB channel respectively.

Table 4-2. *.Interpolated digits of Gray Scale Q14 and corresponding percentage errors to the reflectance factors.*

Ref. factors	R_int	G_int	B_int	ErrorRint (%)	ErrorGint (%)	ErrorBint (%)
0.9404	0.9406	0.9407	0.9402	0.03	0.03	0.02
0.8968	0.8945	0.8956	0.8927	0.25	0.13	0.45
0.6917	0.6921	0.6912	0.6912	0.06	0.07	0.07
0.5358	0.5379	0.5347	0.5365	0.40	0.21	0.14
0.4349	0.4367	0.4377	0.4424	0.42	0.64	1.71
0.3422	0.3404	0.3417	0.3406	0.52	0.16	0.48
0.2696	0.2703	0.2716	0.2759	0.26	0.74	2.35
0.2109	0.2118	0.2113	0.2097	0.39	0.18	0.58
0.1712	0.1702	0.1707	0.1705	0.58	0.31	0.37
0.1347	0.1345	0.1352	0.1338	0.19	0.31	0.73
0.1056	0.1055	0.1063	0.1059	0.07	0.66	0.31
0.0847	0.0849	0.0851	0.0842	0.26	0.45	0.55
0.0692	0.0690	0.0693	0.0685	0.32	0.25	1.03
0.0537	0.0541	0.0531	0.0528	0.80	1.00	1.65
0.0434	0.0432	0.0436	0.0413	0.48	0.44	4.72
0.0340	0.0343	0.0342	0.0326	0.91	0.65	4.06
0.0298	0.0291	0.0302	0.0294	2.33	1.30	1.41
0.0217	0.0216	0.0214	0.0207	0.60	1.54	4.71
0.0170	0.0164	0.0162	0.0160	3.73	4.79	5.80
0.0135	0.0129	0.0125	0.0143	4.49	7.95	5.50
0.0115	0.0105	0.0093	0.0108	9.40	19.43	6.05
Mean				**1.26**	**1.96**	**2.03**

Compared to the results at Table 4-1, the results after interpolation in Table 4-2 have been improved significantly, especially for red and green channels. This improvement will impact the accuracy and image quality of final spectral images, especially for low spectral reflectance ranges. For simplicity, these interpolated digits are called final linearized digits in the following sections. Consequently, the camera spectral sensitivities

and linearized RGB digits for system calibration as mentioned in Chapter 3 are required to be recalculated by adding one more interpolation procedure. We call the whole procedure as double linearization procedure. The re-calculated spectral sensitivities of the DKC-ST5 camera are shown in Fig. 4-5. These results were used for computer simulation in the image quality research. Fig. 4-6 plots the re-calculated camera spectral sensitivities as shown in Fig 4-5 and the previously calculated results without using the second interpolation after flatting field as shown in Fig. 3-7(a) together. Fig 4-6 indicates that the difference between the results using double interpolation and the results using conventional method is very small. The correlations between them are 0.999988, 0.999995 and 0.999990 for R, G and B channels respectively. It should be emphasized here that the camera spectral sensitivities shown here are defined in the reflectance space.

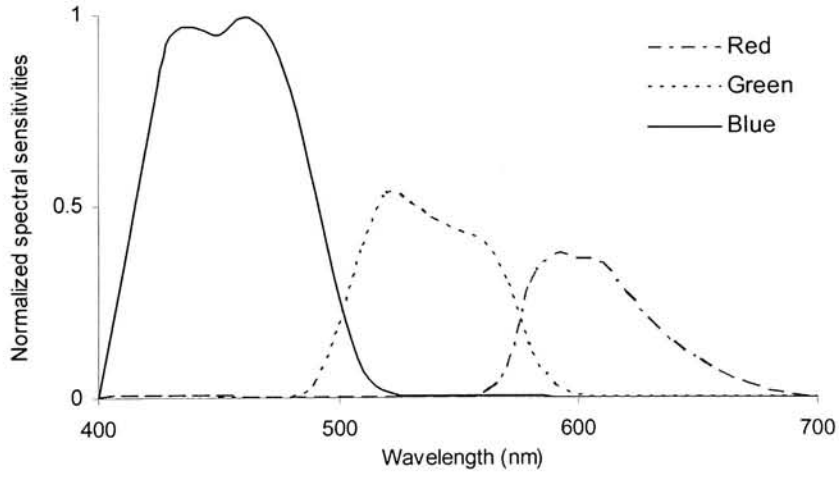

Figure 4-5. *Recalculated spectral sensitivities of DKC-ST5 Camera by using double interpolation procedure*

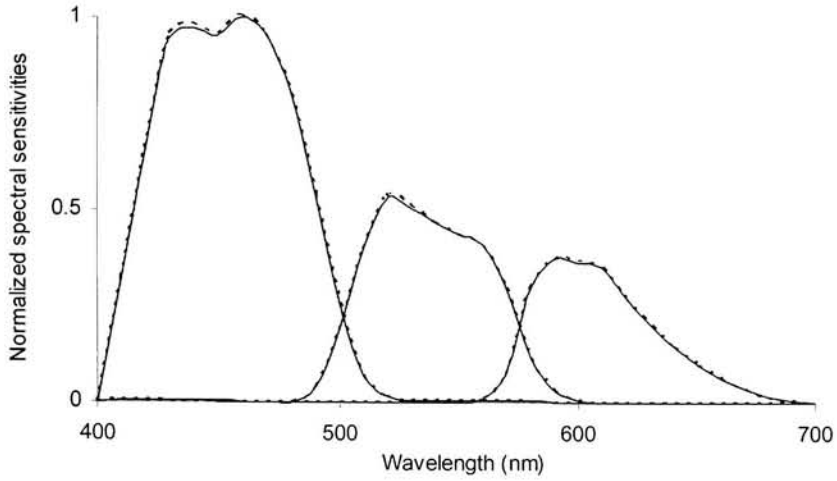

Figure 4-6. *Spectral sensitivities of DKC-ST5 Camera by using and without using double interpolation procedure. The solid lines are for results using double interpolation while the doted lines are for conventional method.*

The next step was to simulate the gray scale responses based on Eq. 2-1 to Eq. 2-4. For demonstration, we estimated the responses of perfect white first. The responses of perfect white were 0.2979, 0.3100 and 0.3500 for R, G and B channels respectively. The correct responses should be normalized based on the responses of perfect white since the spectral sensitivities of the camera were normalized with relative meanings. An alternative way is to perform regression by using the spectral reflectances of gray scales to determine the normalized ratio or, using one-order linear regression, the coefficients. First-order linear regression method was chosen in this research. The results are given in Eq. 4-4 to Eq. 4-6.

$$R_s = 8.1263E\text{-}5 + 3.3193 \cdot R_D, \quad (4\text{-}4)$$
$$G_s = 7.0744E\text{-}4 + 3.2128 \cdot G_D, \quad (4\text{-}5)$$
$$B_s = 5.1862E\text{-}4 + 2.8866 \cdot B_D, \quad (4\text{-}6)$$

where R_D, G_D, and B_D are camera responses calculated from Eq. 2-4 for RGB channels respectively, R_s, G_s, and B_s are corresponding final simulated responses. R_s, G_s, and B_s

have values at [0, 1]. In practice, clipping is required for simulated response less than 0 or larger than 1. In the following simulation, the camera responses for any spectra were determined by first using Eq. 2-4 then applying Eq. 4-4 to Eq. 4-6. The simulated results and corresponding percentage differences to the reflectance factors for gray scales are given in Table 4-3 where the first two gray scales are perfect white and high quality white paper, the last one is the perfect dark and the rest are Kodak Gray Scale Q14. For demonstration, the results in Table 4-3 were not clipped into [0, 1]. The results shows that the simulation for gray scales was quite successful.

***Table 4-3**. The simulated results for gray scales*

Gray Scale #	Ref. factors	Rd	Gd	Bd	Rs	Gs	Bs
1	1.0000	0.2979	0.3100	0.3500	0.9889	0.9967	1.0099
2	0.9404	0.2814	0.2924	0.3280	0.9342	0.9403	0.9462
3	0.8968	0.2702	0.2806	0.3118	0.8969	0.9021	0.8994
4	0.6917	0.2098	0.2144	0.2366	0.6966	0.6897	0.6826
5	0.5358	0.1625	0.1656	0.1839	0.5393	0.5328	0.5303
6	0.4349	0.1313	0.1346	0.1511	0.4359	0.4331	0.4356
7	0.3422	0.1035	0.1056	0.1185	0.3435	0.3401	0.3414
8	0.2696	0.0808	0.0835	0.0945	0.2683	0.2690	0.2723
9	0.2109	0.0636	0.0653	0.0735	0.2111	0.2104	0.2115
10	0.1712	0.0512	0.0530	0.0602	0.1701	0.1711	0.1732
11	0.1347	0.0408	0.0417	0.0467	0.1354	0.1347	0.1342
12	0.1056	0.0317	0.0325	0.0369	0.1054	0.1053	0.1059
13	0.0847	0.0255	0.0263	0.0295	0.0849	0.0851	0.0847
14	0.0692	0.0207	0.0213	0.0242	0.0688	0.0690	0.0693
15	0.0537	0.0159	0.0165	0.0190	0.0529	0.0538	0.0545
16	0.0434	0.0129	0.0135	0.0155	0.0428	0.0442	0.0443
17	0.0340	0.0101	0.0104	0.0120	0.0335	0.0343	0.0341
18	0.0298	0.0089	0.0093	0.0106	0.0296	0.0306	0.0300
19	0.0217	0.0064	0.0067	0.0077	0.0214	0.0223	0.0217
20	0.0170	0.0050	0.0052	0.0060	0.0168	0.0176	0.0169
21	0.0135	0.0040	0.0042	0.0048	0.0134	0.0141	0.0134
22	0.0115	0.0034	0.0036	0.0041	0.0114	0.0122	0.0114
23	0.0000	0.0000	0.0000	0.0000	0.0001	0.0007	-0.0005
Mean error (%)					**0.74**	**1.20**	**0.70**
Max error (%)					**1.49**	**5.75**	**1.99**

4.1.3 Error Correction for Measured Data

During the imaging experiment error could not be avoided. One of those errors could be due to the movement of the subjects during imaging and spectral measurement.

Consequently, it may cause discrepancy between spectral measurement and corresponding RGB digits. An obvious evidence was the relatively larger errors for the reproduction of dark spectra in Chapter 3 and displayed relatively larger image noise in the dark area of the spectral images. Therefore, before simulation of the real face spectral reflectances and their corresponding camera responses, camera digits, some error and accuracy investigation to the whole measured data sets was necessary. Based on this investigation, some necessary procedures may need to be applied to improve the accuracy of simulation.

The procedures of simulation of the camera responses of real face spectral reflectances are described as follows:

1. Recalculate the 544 sets of final linearized digits of face targets which contributed the corresponding spectral measurements using double interpolation procedure as mentioned above.

2. Simulate the camera responses of the 544 face spectral reflectances by applying the Eqs. 2-1 to 2-4 and Eqs. 4-4 to 4-6.

3. To improve the gray scale response, 6 gray scale targets from GretagMacbeth Color Checker were added into 544 sets of face data in simulation.

It should be noted here that all those calculation and simulation involved imaging system with and without using external filter. We then compared the percentage errors between the linearized digits from procedure 1 and simulated digits from procedure 2. The mean percentage error was very large with the value of 10.63%. The correlation coefficient between the calculated linearized digits and simulated digits was 0.9935.

Table 4-4 gives the number of targets that their percentage errors in simulation were above 5%, 10%, 20% for each RGB channels simultaneously.

Table 4-4. *Number of targets that their percentage errors in simulation were above 10%, 20%, and 30% for any RGB channels.*

	percentage error for all channels		
	>5%	>10%	>20%
Number of targets	109	71	31

Table 4-4 indicates that there were 20%, 13% and 6% data sets that their percentage errors were above 5%, 10% and 20% for all RGB channels simultaneously in simulation respectively. This could be due to the experimental errors during imaging and spectral measurement as mention previously. It could be also due to the inaccuracy in simulation itself. Either case, it was necessary to investigate the errors in further detail. Therefore, we performed a kicking-away processing for those data sets that their simulated results had large errors as indicated in Table 4-4. In kicking-away processing, those data sets with simulated results in all channels having percentage errors above 5%, 10%, and 20% would be kicked out of the data sets. The percentage errors of the remaining data sets were then recalculated. The results are shown in Table 4-5.

Table 4-5. *The percentage errors of simulation for remain data sets after kicking-away game .*

	percentage error for all channels		
	>5%	>10%	>20%
Mean errors (%)	3.21	5.63	8.00

Table 4-5 shows that after 109 data sets, that their simulated errors were above 5% for all channels simultaneously, kicked away the percentage errors in simulation for the remained 441 data sets were improved significantly. Therefore, the 5% criterion was

selected to kick away some bad data sets in the following simulation except for specific cases. Before leaving this issue, we will provide some details of the kicked-away data sets. Table 4-6 gives the mean linearized digit values of kicked-away data sets for different criteria. Table 4-6 indicates that the kicked-away data sets are, on average, the dark samples. This may be due to fact that during the imaging and spectral measurement, it took more integration time for spectroradiometer PR-704 to measure the dark spectra. Therefore, there would be more risk of subjects moving their faces. Consequently, those spectral measurements would not be consistent with the imaging signals, hence large error in calibration as well as in simulation.

Table 4-6. *Mean linearized digit values of the kicked-away data sets.*

	percentage error for all channels		
Percentage error (%)	>5%	>10%	>20%
Mean	0.083	0.077	0.067

4.1.4 Simulation of Face Spectral Reflectance Response

After kicking-away the bad data sets, the simulation for spectral images was performed. As the same way performed in Chapter 3, the transfer matrices were required to be determined. We assumed that there were no errors involved in spectral measurements since the spectroradiometer always captured the spectral reflectances. Therefore, the basis functions didn't change. For 3 and 6 basis functions, different terms of transfer matrices had been tested. We also recalculated the spectral images using double linearization procedure and new calibration based on data sets without kicked-away bad data sets just described. The details are described in the following sub-sections.

4.1.4.1 Using 3 Basis Functions

In addition to the 7-term and 17-term transfer matrices as described in Eqs. 3-3 to 3-5 in Chapter 3, 3 terms and 4 terms had also been tested. In 3 terms, only linearized R, G, and B digits with one-order were involved in regression; no high-order or cross terms were involved. In 4-terms, an offset term was added to 3 terms in regression. The mean color differences of calibration in simulation were given in Table 4-7.

Table 4-7. *Color differences of calibration in simulation using 3 basis functions with different transform matrices.*

	Color Difference		
Method	Mean	Maximum	Stdv
3P3T	0.97	4.68	0.69
3P4T	1.43	7.37	1.60
3P7T	1.24	6.39	0.74
3P17T	1.19	6.36	0.76

Table 4-7 indicates that the 3P3T provided the most accurate calibration in simulation. It is interesting to note that more terms used in transform matrices did not always provide more accurate color reproduction when the transform matrices were optimized in terms of spectral matches. By comparing the reconstructed spectral images and rendered using those four different transfer matrices, 3P3T transfer matrix was selected for future application due to its best image results. To provide more experience of error correction described above, the color differences from calibration in simulation by using kicking-away bad data sets in 10% and 20% error criteria are shown in Table 4-8 and Table 4-9 respectively.

Tables 4-7, 4-8 and 4-9 show that the simulated results using the good data sets based on 5% error criterion are the best, which is not surprising due to the fact that more bad

***Table 4-8**. Color differences of calibration in simulation using 3 basis functions with different transform matrices, based on good data sets from 10% error criterion .*

Method	Color Difference Mean	Maximum	Stdv
3P3T	1.10	4.71	0.78
3P4T	1.53	6.31	1.54
3P7T	1.33	6.46	0.74
3P17T	1.27	6.36	0.77

***Table 4-9**. Color differences of calibration in simulation using 3 basis functions with different transform matrices, based on good data sets from 20% error criterion .*

Method	Color Difference Mean	Maximum	Stdv
3P3T	1.33	6.47	0.70
3P4T	1.55	5.99	1.51
3P7T	1.33	6.47	0.70
3P17T	1.27	6.36	0.74

data sets were kicked away. It also indicates that there was no significant error difference using different data sets when high-order transfer matrix was employed. However, because of several modifications applied as described in previous sections, the transfer matrix with the simplest format of 3P3T could now provide the best results. This had significant practical meaning in terms of image quality for reconstructed spectral images.

4.1.4.2 Using 6 Basis Functions

When using 6 basis functions, four different terms of transfer matrices, 6P6T, 6P7T, 6P13T and 6P27T, were tested. The different matrices of linearized digits applied to estimate these four transfer matrices are defined as following (using the same definitions in Eq. 3-3):

$$
\begin{aligned}
&\textit{6 terms}: && \boldsymbol{Q} = [\boldsymbol{D}(1{:}3) \quad \boldsymbol{D}_f(1{:}3)] \\
&\textit{7 terms}: && \boldsymbol{Q} = [\boldsymbol{D}(1{:}3) \quad \boldsymbol{D}_f(1{:}3) \quad \boldsymbol{I}] \\
&\textit{13 terms}: && \boldsymbol{Q} = [\boldsymbol{D}(1{:}6) \quad \boldsymbol{D}_f(1{:}6) \quad \boldsymbol{I}] \\
&\textit{27 terms}: && \boldsymbol{Q} = [\boldsymbol{D}(1{:}10) \; \boldsymbol{D}(14{:}16) \; \boldsymbol{D}_f(1{:}10) \; \boldsymbol{D}_f(14{:}16) \; \boldsymbol{I}]
\end{aligned}
$$

The mean color differences of calibration in simulation are given in Table 4-10.

Table 4-10. *Color differences of calibration in simulation using 6 basis functions with different transform matrices.*

Method	Color Difference Mean	Maximum	Stdv
6P6T	0.30	3.68	0.29
6P7T	0.25	3.86	0.27
6P13T	0.15	4.41	0.24
6P27T	0.15	4.42	0.24

Compared to the case of 3 basis functions, the errors were significantly lessened when 6 basis functions were employed in spectral reconstruction. Due to the similar reason as in 3 basis-functions case, 6P6T was selected for future application. As in the previous section for 3 basis functions, the mean color differences from calibration in simulation by using kicking-away bad data sets in 10% are shown in Table 4-11.

Table 4-11. *Color differences of calibration in simulation using 6 basis functions with different transform matrices, based on good data sets from 10% error criterion .*

Method	Color Difference Mean	Maximum	Stdv
6P6T	0.32	3.02	0.35
6P7T	0.25	3.59	0.30
6P13T	0.14	4.40	0.26
6P27T	0.15	4.41	0.26

4.1.5 Recalibration for Spectral Imaging System

We had improved the image processing algorithms and modified the data sets applied for the system simulation. In this section we will recalibrate the spectral imaging system and deal with the impact of those modifications to the system calibration as described in the Chapter 3. The remaining 441 data samples were involved in system calibration. The double linearization procedure was employed to calculate the final linearized digits.

Based on 3 and 6 basis functions, different transfer matrices were tested for spectral and color reproduction.

4.1.5.1 Using 3 Basis Functions

When using 3 basis functions, the same four different terms of transfer matrices as in sub-section 4.1.4.1 were tested based on Eq. 3-3 to Eq. 3-5. The resulted mean color differences are shown in Table 4-12.

Table 4-12. *Color differences of calibration for imaging system using 3 basis functions, 441 data sets, and with different transform matrices.*

	Color Difference		
Method	Mean	Maximum	Stdv
3P3T	1.98	6.19	0.87
3P4T	2.68	14.07	2.77
3P7T	2.10	8.10	1.50
3P17T	1.75	6.36	1.05

Compared to Table 3-12, it shows that the accuracy of calibration had been significantly improved. This, on the other hand, proved that the kicking-away game was a good procedure to correct the measured data sets when some errors were involved. An interesting phenomenon is that 3P4T transfer matrix generated much larger color difference than that using 3P3T. It is important to emphasize here that the 3P3T transfer matrix would generate very large error, large beyond practical tolerances, if the original data sets were applied for calibration. For comparison, the color accuracy of calibration for remaining data sets using other criteria of 10% and 20% are given in Table 4-13 and Table 4-14 respectively. Not surprisingly, the remaining data sets with error kicking-away criteria of 10% and 20% generated larger color difference in calibration for color reproduction.

***Table 4-13**. Color differences of calibration for imaging system using 3 basis functions, remained data sets using 10% criterion, and with different transform matrices*

	Color Difference		
Method	Mean	Maximum	Stdv
3P3T	2.14	5.51	0.99
3P4T	2.90	12.70	2.68
3P7T	2.23	6.99	1.41
3P17T	1.89	6.83	1.10

***Table 4-14**. Color differences of calibration for imaging system using 3 basis functions, remained data sets using 20% criterion, and with different transform matrices*

	Color Difference		
Method	Mean	Maximum	Stdv
3P3T	2.28	6.49	1.09
3P4T	3.06	12.21	2.70
3P7T	2.36	7.35	1.48
3P17T	2.00	6.96	1.19

4.1.5.2 Using 6 Basis Functions

As similar to the previous section, the imaging system was recalibrated based on the remaining 441 data sets and 6 basis functions. The resulting color differences for four different terms of transfer matrices are shown in Table 4-15.

***Table 4-15**. Color differences of calibration for imaging system using 6 basis functions, 441 data sets, and with different transform matrices.*

	Color Difference		
Method	Mean	Maximum	Stdv
6P6T	1.61	7.44	1.10
6P7T	1.38	6.48	0.82
6P13T	1.16	6.37	0.78
6P27T	1.08	5.93	0.70

Compared to Table 3-12, the accuracy of calibration here is significantly improved. To test further, spectral images were reconstructed by using these four different transfer matrices and they were rendered using sRGB model as mentioned in the Chapter 3. The rendered images showed that the image quality had been improved, especially in the dark

area. It also showed that image quality of displayed images from using 6P6T and 6P7T transfer matrices were almost the same. The rendered spectral images using high-order transfer matrices of 6P13T and 6P27 showed relatively large noise. rendered spectral images using 3 basis functions were also judged. Considering the accuracy of spectral reproduction and in terms of image quality, 6P6T transfer matrix was finally selected for spectral image reconstruction. Those reconstructed spectral images would be treated as the original objects for the spectral imaging system to simulate in the following image quality analysis.

For comparison purpose, the color accuracy of system calibration using the remaining data sets with the 10% error criterion is given in Table 4-16. Not surprising, compared to the system calibration using 441 data sets, larger color differences were generated here.

Table 4-16. *Color differences of calibration for imaging system using 6 basis functions, remained data sets using 10% criterion, and with different transform matrices.*

	Color Difference		
Method	Mean	Maximum	Stdv
6P6T	1.71	6.95	1.18
6P7T	1.57	6.18	0.93
6P13T	1.27	6.64	0.87
6P27T	1.19	6.59	0.79

The first three basis functions based on face spectra of all races have already shown in the Chapter 3. The 4th to 6th basis functions are shown in the Fig. 4-7. The Fig. 4-7 shows that the 4th to 6th basis functions vary more frequently over the wavelength range compared to that of the first three basis functions in Fig. 3-12. This suggests that the 4th to 6th basis functions will contribute more fine shape details in spectral reconstruction.

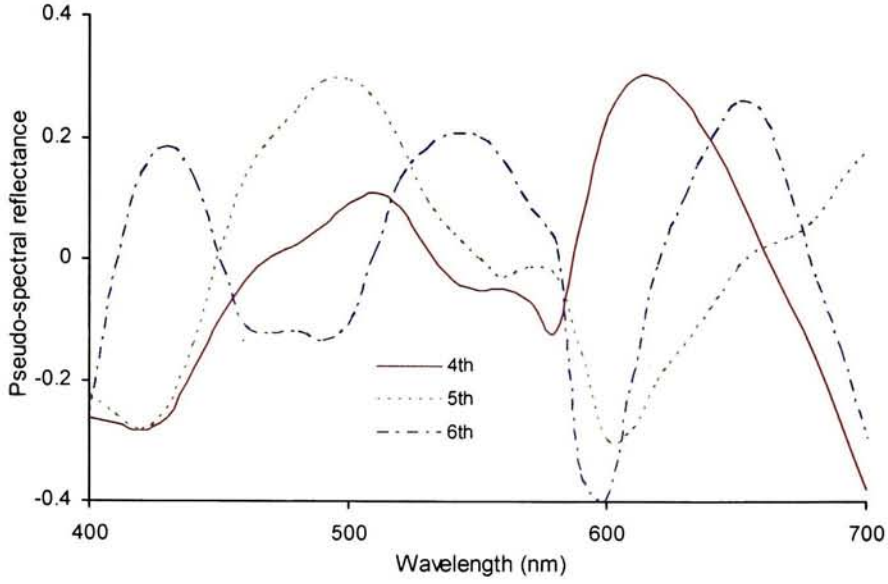

Figure 4-7. *The 4th to 6th basis functions based on all spectral from all races*

4.1.6 Color Accuracy of PCA Method Using Different Wavelength Steps and Different Number of Basis Functions

In simulation, spectral images were reconstructed using different wavelength steps and different number of basis functions. For the human face spectral imaging system, 3 and 6 basis functions were employed. For IMB camera system, 3, 6 and 9 basis functions were applied. Wavelength steps of 2nm, 5nm, 10nm, 15nm and 20nm were selected for simulation. Since the wavelength steps were changed, the basis functions for corresponding spectra were required to be recalculated. The accuracy of calibration in system simulation, therefore, was necessary to be reinvestigated.

To apply PCA for the spectral data, the first step was to interpolate the measured spectral reflectances into 2nm, 5nm, 10nm, 15nm, and 20nm steps. The wavelength range

in this research was selected to be 400nm to 700nm. As recommended by researchers in MCSL, Vrhel's[73] spectral data set was selected for IBM Pro/3000 camera simulation. Vrhel's spectral data set contains 170 natural and man-made object spectra with the wavelength range from 390nm to 730nm in 2nm increments. We will discuss the PCA results for face spectral data and Vrhel's data separately in the following sub-sections. The accuracy of PCA applications, and spectral reproduction by simulation using different wavelength steps and different basis functions will also be described in detail.

4.1.6.1 PCA Results for Face Spectra

PCA was applied to 544 data sets of face spectra with different wavelength steps. The results in Table 4-17 show the cumulative contribution percentages of the first one to six principal components for all 544 face spectral reflectances with different wavelength steps. The results in Table 4-17 indicate that the first three principal components will cover over 99.88% of the variance for all spectral data with each wavelength step used. For the same number of basis functions, the differences of cumulative contribution percentages using different wavelength steps are very small and have no practical meanings. Of course, mathematically, the smaller the wavelength steps used, the larger the cumulative contribution percentages when using the same number of basis functions. This may be due to the fact that small wavelength steps will make the spectra smoother and the dimensions of variation will be smaller, hence larger coverage when using the same number of basis function compared to that using larger wavelength steps.

Based on Eq. 2-5 and the basis functions obtained above for different wavelength steps, the spectral reflectances could be estimated. The results of color differences are shown in Table 4-18 where 3P and 6P represent using 3 and 6 basis functions respectively. Other results in terms of different races and different face parts are not shown here.

Table 4-17. *Cumulative contribution percentage of principal components calculated from spectra of all race with different wavelength steps.*

	Number of basis functions					
Steps	1	2	3	4	5	6
2nm	97.89	99.57	99.89	99.97	99.99	99.99
5nm	97.89	99.56	99.89	99.97	99.99	99.99
10nm	97.88	99.56	99.89	99.97	99.99	99.99
15nm	97.87	99.56	99.88	99.97	99.98	99.99
20nm	97.86	99.56	99.88	99.97	99.98	99.99

Table 4-18. *Color differences of face spectral reproduction based on 3 and 6 basis functions using different wavelength steps.*

	Color Differences (3P)			Color Difference (6P)		
Steps	Mean	Maximum	Stdev	Mean	Maximum	Stdev
2nm	1.10	4.95	1.06	0.14	1.64	0.13
5nm	1.12	5.06	1.08	0.14	1.73	0.14
10nm	1.15	5.24	1.13	0.16	1.95	0.15
15nm	1.17	5.36	1.16	0.18	2.26	0.17
20nm	1.22	5.64	1.21	0.20	2.36	0.18

The results in Table 4-18 indicates that the color reproduction would be more accurate when smaller wavelength steps are used. The results also show that there are no significant color differences in spectral reproduction when using different wavelength steps. It should be emphasized here that the above results were calculated between the measured spectra and their corresponding estimation with the same wavelength steps. Since the original spectra were measured with 2nm step it is practically required to

compare the colors of the estimated spectra with different wavelength steps to the original spectra obtained using the 2nm step. The results are shown in Table 4-19. The results in Table 4-19 indicates that, using 3 basis functions, different wavelength steps caused significant color difference for color and spectral reproduction except for that using 20nm increments. When using 6 basis functions, large wavelength steps, 15nm and 20nm, generated significant larger color difference compared to that using 2nm step. This may give us practical suggestion that large wavelength steps, such as 15nm and 20nm, should be avoided if possible. However, the impact on the final image quality still needs to be further investigated.

Table 4-19. *Color differences between measured face spectra with 2nm step and estimated spectral based on 3 and 6 basis functions using different wavelength steps.*

	Color Differences (3P)			Color Difference (6P)		
Steps	Mean	Maximum	Stdev	Mean	Maximum	Stdev
5nm	1.12	5.06	1.08	0.14	1.71	0.13
10nm	1.15	5.24	1.13	0.16	1.96	0.15
15nm	1.19	5.30	1.14	0.31	2.35	0.17
20nm	1.45	5.66	1.10	0.61	1.88	0.26

4.1.6.2 Simulation Results for Face Spectral Data

After determining the basis functions of face spectra using different wavelength steps the camera responses for those spectra could then be simulated and the simulation of spectral reproduction could be performed as well. The procedures are described as follows:

1. Interpolate the spectral sensitivities of camera, spectral transmittance of filter, spectral power radiation of lighting and spectral reflectances of gray scale, Kodak Gray Scale Q14, into different wavelength steps as mentioned above based on 2nm step spectra.

2. Determine the coefficients of equations of the second linearization procedure, as shown in Eq. 4-4 to Eq. 4-6, for each wavelength steps.

3. Calculate the 441 sets of final linearized digits of face targets which contributed the corresponding spectral reflectances for each wavelength steps based their own optimized equations.

4. Determine the transfer matrices of 3P3T and 6P6T to convert the final linearized digits to eigenvalues for spectral data sets with different wavelength steps.

5. Using the Eq. 2-5 to reconstruct the spectra and calculate the color difference for verification purpose.

There were several ways to check the accuracy in color and spectral reproduction. The first one was to calculate the mean color differences between the simulated and measured 441 sets of face spectra that using the same wavelength steps. The results of color differences are given in Table 4-20. The results in Table 4-20 indicates that,

Table 4-20. *Color differences between the simulated and measured 441 sets of face spectra that using the same wavelength steps.*

	Color Differences (3P3T)			Color Difference (6P6T)		
Steps	Mean	Maximum	Stdev	Mean	Maximum	Stdev
2nm	0.97	4.68	0.69	0.30	3.68	0.29
5nm	1.04	4.95	0.77	0.35	3.53	0.39
10nm	1.07	5.28	0.82	0.41	4.33	0.46
15nm	1.11	5.66	0.87	0.47	5.05	0.55
20nm	1.18	6.36	0.96	0.54	5.72	0.63

between the simulated and measured spectra using the same wavelength steps, there were no significant differences in accuracy of color reproduction when using 3P3T transfer matrices. However, when using 6P6T transfer matrices, the mean color difference

between the estimated and measured using 2nm step was significantly smaller than that using larger wavelength steps.

The second way was to calculate the color differences between the 441 sets of simulated spectra, using different wavelength steps, and corresponding measured spectra with the wavelength step of 2nm. This method provides us a more accurate picture of the accuracy in simulation modeling since it demonstrated the errors caused by using larger wavelength steps other than 2nm. The results are given in Table 4-21.

Table 4-21. *Color differences between the 441 measured face spectra using 2nm step and the corresponding simulated spectra using different wavelength steps.*

	Color Differences (3P3T)			Color Difference (6P6T)		
Steps	Mean	Maximum	Stdev	Mean	Maximum	Stdev
2nm	0.97	4.68	0.69	0.30	3.68	0.29
5nm	1.36	5.92	1.27	0.36	3.56	0.40
10nm	1.92	10.48	2.18	0.42	4.38	0.49
15nm	2.40	14.46	2.98	0.48	5.09	0.56
20nm	2.87	17.58	3.66	0.54	5.73	0.63

The results in Table 4-21 show the different, but more precise, picture of the accuracy in simulation. The results indicate that, compared to the colors of the original measured spectra, the smaller the wavelength steps used the more accurate the simulations would be, especially when using 3P3T transfer matrices. It should be noted that the color calculation was applied the normalization using the perfect white for each wavelength steps. Therefore, the colors of the perfect whites, using different wavelength steps, should be the same. An emphasis here is that those large color differences were also partly contributed from the inaccurate color matching functions and over-averaged in color integration when using large wavelength steps. In other words, those large color differences, partly, only had mathematical meaning. It can be improved by interpolating

either the measured spectra, if using large wavelength steps due to device limit, or simulated spectra into wavelength step of 2nm when computing the colors. However, just for the purpose of simulating the normal procedure of calculating the color using different wavelength steps, the author did not try to perform any means of improvement for those color differences. Therefore, when the simulated spectral images were sent for rendering, these mathematical 'errors' would be transferred into practical meanings, hence image quality problems.

The next step was to test the accuracy of color reproduction for all 550 sets of spectra, 544 sets of face spectra and 6 gray scales. The Table 4-22 shows the results of color differences between 550 sets of spectra with wavelength step of 2nm and corresponding simulated spectra with different wavelength steps. Not surprisingly, the color differences of simulation for all spectra were larger than that in simulation modeling.

Table 4-22. *Color differences between all 550 sets of measured spectra using 2nm step and the corresponding simulated spectra using different wavelength steps.*

	Color Differences (3P3T)			Color Difference (6P6T)		
Steps	Mean	Maximum	Stdev	Mean	Maximum	Stdev
2nm	1.14	4.73	0.81	0.36	3.04	0.40
5nm	1.66	5.92	1.52	0.42	3.54	0.49
10nm	2.49	10.59	2.73	0.50	4.43	0.58
15nm	3.34	14.57	3.71	0.64	5.44	0.62
20nm	3.84	17.54	4.43	0.93	7.82	0.73

Once the transfer matrices in simulation were determined, the spectral images could then be simulated. The original spectral images were estimated from the procedure described in the section 4.1.5.2 using 6P6T transfer matrix based on linearized digits and corresponding spectra. This transfer matrix was different from the transfer matrix in

simulation as described in this section. The original spectral images were then treated as the imaging objects for spectral imaging system simulation. The procedure is as follows:

1. Interpolate the spectra of spectral imaging targets, spectral images created in section 4.1.5.2 using wavelength step of 2nm, into different wavelength steps, pixel by pixel.

2. Calculate the camera responses of the spectral imaging targets with different wavelength steps, pixel by pixel.

3. Convert the camera responses to eigenvalues based on either 3P3T or 6P6T simulation transfer matrices for different wavelength steps, pixel by pixel.

4. Reconstruct the spectra with different wavelength steps based on 3 or 6 basis functions, pixel by pixel, hence getting the simulated spectral images that using different wavelength steps.

Actually, in practice, the simulated spectral images were stored in the format of eigenvalues for each pixel.

So far, we dealt with simulation of spectral imaging for human face using SONY DKC-ST5 digital camera. In the next two sections the simulation of spectral imaging for IBM Pro\3000 digital camera will be discussed. The procedure of simulation for spectral imaging system using IBM camera was very similar to that for the face spectral imaging system using SONY DKC-ST5 digital camera. The exception was that the second linearization procedure in simulation was not necessary for IBM camera since its spectral sensitivities are very close to the color matching functions and the OECFs are well linearized.

In the next two sections we will discuss the Vrhel's spectral data in PCA and simulation of the spectral imaging system using IBM Pro\3000 digital camera.

4.1.6.3 PCA Results for Vrhel's Spectra

The Vrhel's spectral data are shown in the Fig. 4-8.

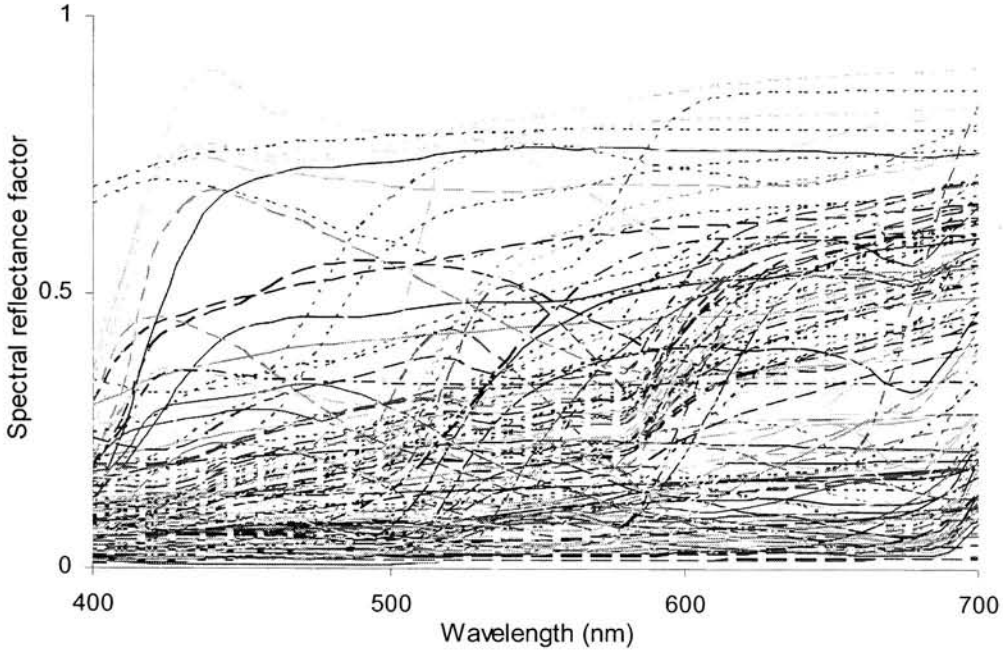

Figure 4-8. *Vrhel's spectral data*

As we did in the previous sections, PCA was applied to Vrhel's spectral data with different wavelength steps. The cumulative contribution percentages of the first one to nine principal components for Vrhel's spectra with different wavelength steps are given in Table 4-23. The results in Table 4-23 indicate that the first six principal components cover over 99.5% of the variance for all spectral data with each wavelength steps used. For same number of basis functions, the differences of cumulative contribution percentages using different wavelength steps are very small that have no practical meaning.

Table 4-23. *Cumulative contribution percentage of principal components calculated from Vrhel's spectra with different wavelength steps.*

	Number of basis functions								
Steps	1	2	3	4	5	6	7	8	9
2nm	81.28	93.40	97.94	98.78	99.32	99.62	99.75	99.87	99.92
5nm	81.13	93.36	97.87	99.74	99.29	99.60	99.75	99.87	99.92
10nm	81.06	93.30	97.76	98.65	99.23	99.59	99.74	99.87	99.92
15nm	81.00	93.23	97.65	98.56	99.18	99.57	99.73	99.87	99.92
20nm	80.85	93.13	97.51	98.45	99.10	99.54	99.72	99.86	99.91

The first nine basis functions with wavelength step of 10nm are shown in the Fig. 4-9.

Based on those basis functions, the spectra could be estimated. Table 4-24 shows the results of color differences in spectral reproduction using 3, 6 and 9 basis functions

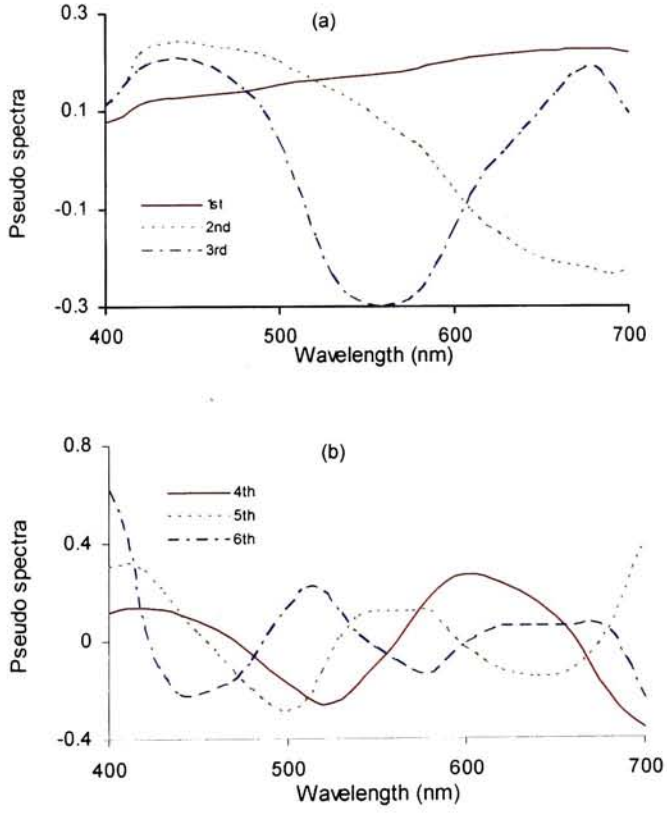

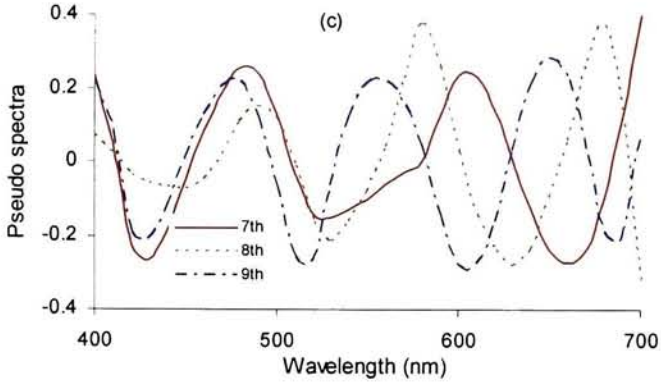

Figure 4-9. *The first nine basis functions. (a) the first 3 basis functions; (b) the 4th to 6th basis functions; (c) the 7th to 9th basis functions.*

respectively. These color differences were calculated between estimated and measured spectra with the same wavelength steps.

Table 4-24. *Color differences of spectral reproduction for Vrhel's spectra based on 3, 6, and 9 basis functions using different wavelength steps.*

	Color Diff. (3P3T)			Color Diff. (6P6T)			Color Diff. (9P9T)		
Steps	Mean	Max	Stdev	Mean	Max	Stdev	Mean	Max	Stdev
2nm	4.27	35.38	5.72	0.74	5.89	0.81	0.24	3.21	0.38
5nm	4.32	35.44	5.76	0.76	5.52	0.81	0.25	3.37	0.39
10nm	4.41	35.32	5.80	0.81	5.34	0.84	0.27	3.63	0.41
15nm	4.51	35.34	5.87	0.85	5.67	0.88	0.29	3.74	0.41
20nm	4.60	34.99	5.89	0.94	6.17	0.96	0.33	4.20	0.48

The results in Table 4-24 indicate that, for Vrhel's spectra, in practice, at least 6 basis functions are required for better color and spectral reproduction. For accurate evaluation, the color differences were also calculated between the original spectra with wavelength step of 2nm and the reproduced spectra using different wavelength steps. The results are given in Table 4-25. The results show that, when using 6 or 9 basis functions, there are no significant color differences when using small wavelength steps from 2nm to 10nm.

However, there occur significantly larger color differences when large wavelength steps are used, especially when using 20nm step.

Table 4-25. *Color differences between original Vrhel's spectra with 2nm step and estimated spectra based on 3, 6, and 9 basis functions using different wavelength steps*

	Color Diff. (3P3T)			Color Diff. (6P6T)			Color Diff. (9P9T)		
Steps	Mean	Max	Stdev	Mean	Max	Stdev	Mean	Max	Stdev
2nm	4.27	35.38	5.72	0.74	5.89	0.81	0.24	3.21	0.38
5nm	4.33	35.43	5.76	0.76	5.52	0.81	0.26	3.39	0.39
10nm	4.42	35.27	5.81	0.80	5.42	0.85	0.28	3.68	0.41
15nm	4.55	35.46	5.88	0.93	5.84	0.86	0.47	3.59	0.36
20nm	4.64	34.92	5.95	1.44	5.12	1.04	0.80	4.16	0.43

4.1.6.4 Simulation results for Vrhel's spectral data

After determined the basis functions of Vrhel's spectra using different wavelength steps the camera responses for those spectra could then be simulated and the simulation of spectral reproduction could be performed as well. The detail procedure was almost the same as described in section 4.1.6.2. One difference was that a Kodak Wratten filter #66 was applied as the second filter for using of 9 basis functions. The spectral transmittance of Kodak Wratten filter #66 is shown in the Fig. 4-10.

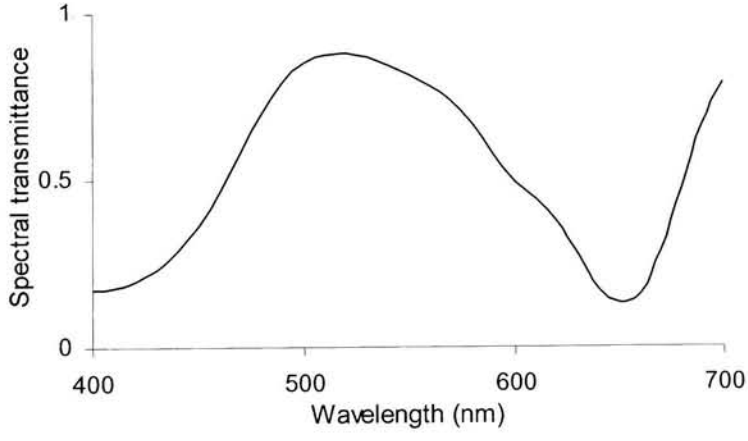

Figure 4-10. *Spectral transmittance of Kodak Wratten No. 66.*

Another difference was that there was no linearization procedure added since the OECFs of IBM Pro\3000, when using raw data of 12 bits, were linear and the spectral sensitivities were very close to the color matching functions. The color differences between the simulated and measured Vrhel's spectral sets using the same wavelength steps are given in Table 4-26.

Table 4-26. *Color differences between the simulated and Measured Vrhel's spectra that using the same wavelength steps.*

	Color Diff. (3P3T)			Color Diff. (6P6T)			Color Diff. (9P9T)		
Steps	Mean	Max	Stdev	Mean	Max	Stdev	Mean	Max	Stdev
2nm	2.04	17.25	2.03	0.88	13.47	1.38	0.26	4.40	0.40
5nm	2.08	17.37	2.04	0.89	13.84	1.39	0.26	4.44	0.41
10nm	2.15	17.56	2.06	0.88	12.69	1.29	0.27	4.55	0.42
15nm	2.21	17.57	2.05	0.90	12.97	1.29	0.26	3.85	0.37
20nm	2.31	17.83	2.08	0.91	10.70	1.17	0.27	3.62	0.37

The results in Table 4-26 indicates that, more basis functions used will provide more accurate simulation results; color accuracy was improved significantly when more basis functions were applied to reproduce the spectra in simulation. A more accurate picture of the accuracy of simulation modeling is given in the Table 4-27 in which the color differences were calculated between the original Vrhel's spectra, with wavelength step of 2nm, and the corresponding simulated spectra using different wavelength steps. The results in Table 4-27 indicate that the simulation based on three basis functions will generate large color differences. Six basis functions will provide good color production in simulation while 9 basis functions will give even more accurate results. Generally speaking, larger color errors will be generated when larger wavelength steps are applied to reproduce the color and spectra in simulation. GretagMacbeth Color Checkers were

employed to test the accuracy of color and spectra reproduction using different transfer matrices for different wavelength steps in spectra.

Table 4-27. *Color differences between measured Vrhel's spectra using 2nm step and the corresponding simulated spectra using different wavelength steps.*

	Color Diff. (3P3T)			Color Diff. (6P6T)			Color Diff. (9P9T)		
Steps	Mean	Max	Stdev	Mean	Max	Stdev	Mean	Max	Stdev
2nm	2.04	17.25	2.03	0.88	13.47	1.38	0.26	4.40	0.40
5nm	2.15	17.56	2.06	0.89	13.85	1.39	0.27	4.45	0.40
10nm	2.17	17.62	2.06	0.88	12.74	1.30	0.29	4.55	0.41
15nm	2.33	17.81	2.05	0.95	12.81	1.31	0.38	3.69	0.36
20nm	2.80	18.68	2.13	0.93	10.60	1.21	0.80	3.56	0.40

Table 4-28 gives the mean color differences between the measured spectra of GretagMacbeth Color Checkers, with wavelength step of 2nm, and their corresponding simulated spectra using different wavelength steps.

Table 4-28. *Color differences between measured spectra of GretagMacbeth Color Checkers using 2nm step and the corresponding simulated spectra using different wavelength steps.*

	Color Diff. (3P3T)			Color Diff. (6P6T)			Color Diff. (9P9T)		
Steps	Mean	Max	Stdev	Mean	Max	Stdev	Mean	Max	Stdev
2nm	3.33	8.17	2.53	1.66	4.97	1.14	0.44	1.56	0.39
5nm	3.37	8.29	2.55	1.68	4.75	1.12	0.44	1.39	0.36
10nm	3.44	8.45	2.56	1.68	5.45	1.17	0.42	1.12	0.34
15nm	3.68	8.72	2.51	1.80	4.82	1.11	0.52	1.05	0.28
20nm	3.76	9.49	2.67	1.47	6.52	1.45	0.69	1.21	0.30

The results in Table 4-28 proves that more than 6 basis functions are required to perform good color and spectral reproduction for painting targets. One important note is that the second external filter, Kodak Wratten filter #66, was used alone, not attached with the first external filter, 202 half C.T blue filter.

Once the transfer matrices in simulation had been determined, the spectral images could then be simulated. The detail of procedure is the same as described in section

4.1.6.2. The spectral imaging targets were spectral images provided in courtesy by researchers in Dr. Miyake's Lab, Chiba University in Japan.

4.1.7 Noise Simulation in Spectral Imaging System.

Any imaging system will include noise, more or less. The noise occurred in the digital camera could be of many independent ways, such as dark noise and shot noise. Dark noise is mainly due to thermal instability of the CCD sensors. Shot noise is due to the variation of photons fallen on CCD sensors and its magnitude is proportional to the square root of light intensity level. It could also be generated during the manufacturing process of CCDs, such as fixed pattern noise caused by the variation of aperture noise. For a whole digital imaging system, the noise could also be due to the instability of the lighting power. Therefore, this research also performed simulation of imaging with noise for spectral imaging system. For simplicity and to limit the total number of target images for visual image quality assessment, simple uniformly distributed and channel independent random noises with 3 different levels were added into imaging capture stage in simulation. They are zero noise, 1 percent noise, and 2 percent noise. The percentage is based on the magnitude range of image in each channel. In reflectance factor space, this range is from 0 to 1.0 for each channel. They were added into the imaging system at the stage that camera integrated the responses for the imaging objects. It was assumed that the one percentage and two percentage noise levels were close to the noise range in reality. The random noise was generated by pseudo-random variable generator in IDL programming environment.

4.2 Calibration for LCD Display

Since the first experimental LCD (liquid crystal display) was made in 1968, LCD manufacturers have steadily developed ingenious variation and improvements on the technology, taking the LCD to amazing levels of technical complexity. LCDs are common because they offer some real advantages over other display technologies. They potentially offer greater luminance, higher contrast ratios, greater sharpness, better spatial uniformity and draw much less power than cathode ray tubes (CRTs).[74, 75] Details of LCD theories and applications are beyond the scope of this research. The author will concentrate on LCD calibration based on its performance with respect to colorimetric characterization. The spectral images simulated in previous sections were rendered on an LCD for the visual experiments. Therefore, the colorimetric characterization of the display was required. The author will also deal with its spatial resolution with respect to its modulation transfer function (MTF) when computing the image sharpness factors and color differences. The colorimetric characterization mainly followed the procedure proposed by Fairchild and Wyble's research.[75] The LCD MTF analysis was based on the theoretical method proposed by Barten.[76]

A 22″ Apple Cinema Display LCD (1600×1024 pixels, 86 pixels-per-inch) was selected as the viewing device for this experiment. The LCD was driven by an Apple Power Macintosh G4 system. In the following sections the spectral and color characteristics of this LCD display are described in detail.

4.2.1 Device Characterization of LCD Display

All the following measurements were performed in a darkened room usually used for visual experiments in MCSL. Before any measurement, all devices for measurement were properly warmed up. The color profile settings of the LCD display were set to maximum in brightness, target gamma of 1.8, target white point of 6,500K with the device indicated chromaticity values(x, y values) of (0.64, 0.34), (0.30, 0.60) and (0.31, 0.33) for red, green, and blue primaries respectively. A Photoresearch Spectrascan 704 (PR 704) spectroradiometer was used for luminance measurements. With the distance of 80cm from the PR704 to the LCD, the luminance of white point was measured as 112.2 cd/m^2 with the correlated color temperature (CCT) of 4,478K. The measured CCT of display white point differed significantly from the value device indicated for D65. The luminance of black point was measured as 0.5618 cd/m^2 with the CCT of 4,422K. Colorimetric measurements were performed using an LMT C1210 colorimeter with viewing field of 1°. The colorimeter was placed as closed to the display screen as possible without contacting with it and was perpendicular to the screen. The measurement was taken place at a centered square color patch (500×500 pixels) generated in an IDL program. The surrounding of the patch on the screen was maintained to medium gray with RGB digital counts of 128 for each channel (luminance of 27.11 cd/m^2 measured by PR704).

Measurement of CIE XYZ tristimulus values were performed for 17 gray patches (digital counts for each RGB channel were the same), 48 RGB ramp patches (digital counts for one channel while keeping digits to zero for other two channels) and 42 random-digit-patches (called RND, digital counts for each channel were randomly

assigned). Gray patches were created by assigning all RGB channels of the display to the same digital counts. Patches of RGB ramps were made by assigning digital counts only to one channel. Random-digit-patches were created by assigning the random digits to RGB channels.

4.2.1.1 Spectral Characteristics

The spectral radiance distributions of the LCD display are given in Fig. 4-11. The spectral radiance in Fig. 4-11 was measured for white (digital count of 255 for all RGB channels) of the display. Fig. 4-12 gives the spectral radiance distributions of the RGB primaries of the display.

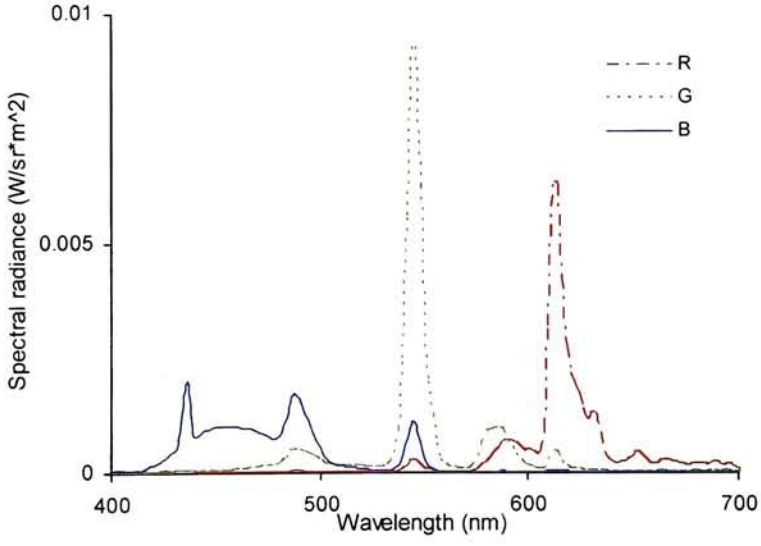

Figure 4-11. *Spectral radiance of the display white.*

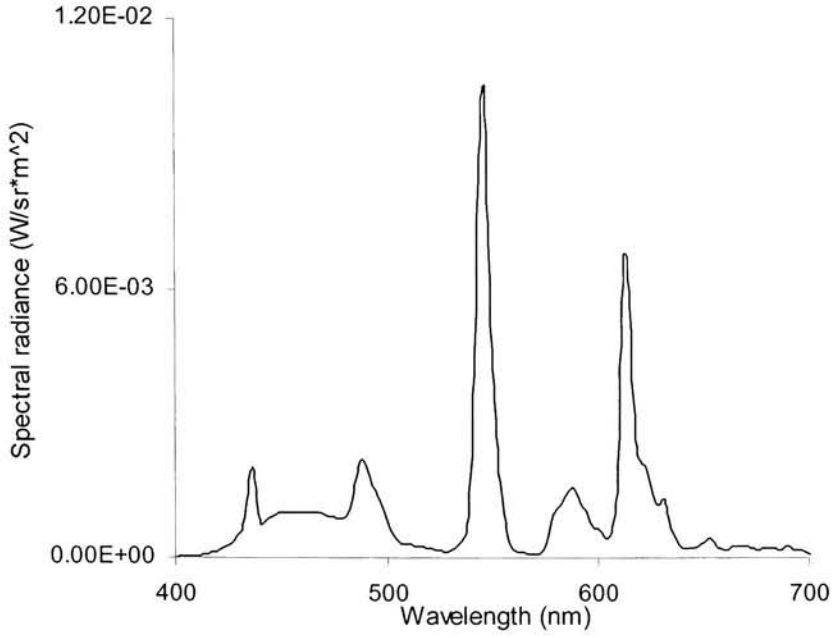

Figure 4-12. *Spectral radiance of the display RGB primaries.*

4.2.1.2 Chromaticity Stability of Primaries

If the chromaticity of the primaries of an LCD display varied with display level, then a simple 3× 3 matrix transform could not be used to convert RGB tristimulus values to CIE XYZ tristimulus values.[75] Measurement of tristimulus values for RGB ramps described above was, therefore, performed to verify the chromaticity stability of the primaries. The measured tristimulus values were then converted to chromaticity coordinates and are plotted on the spectrum locus shown in Fig. 4-13.

It is obvious from Fig. 4-13 that there did occur chromaticity shifting with display level. However, this chromaticity shifting might be from light leakage at the display black point. Thus, the measured tristimulus values of RGB ramps should be corrected by subtracting out the tristimulus values of the black point. After black point correction,

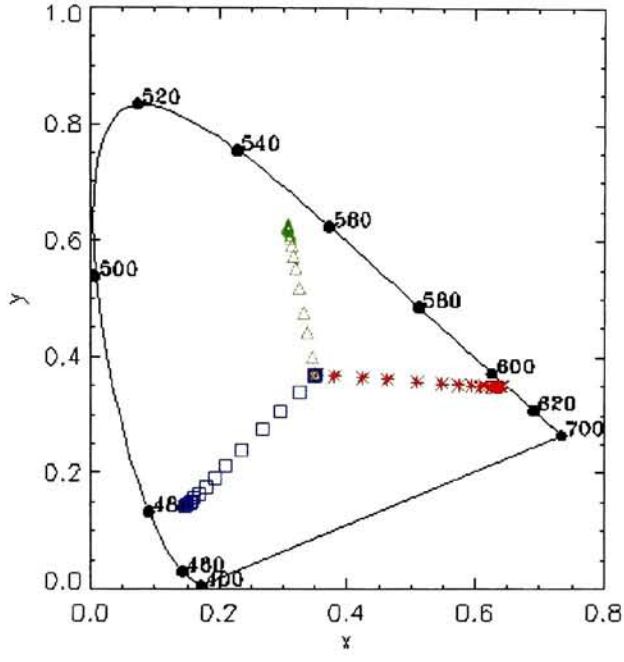

Figure 4-13. *Measured chromaticity coordinates of RGB ramps.*

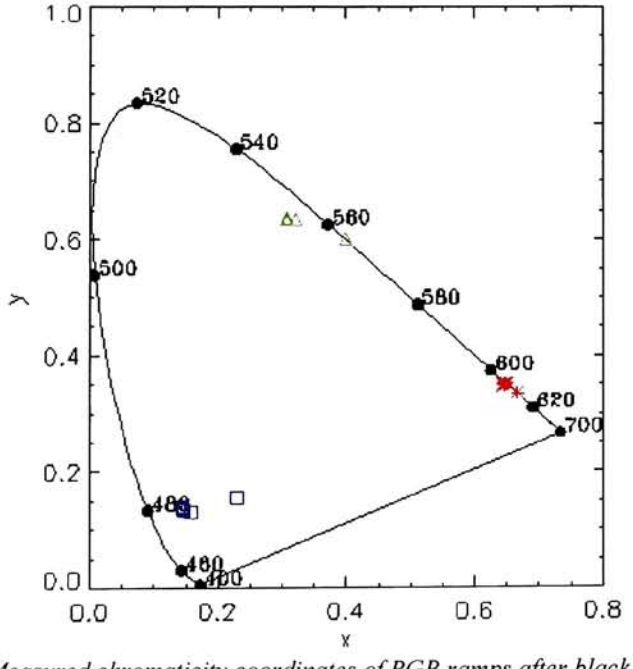

Figure 4-14. *Measured chromaticity coordinates of RGB ramps after black correction.*

the chromaticity coordinates were recalculated. The new results are plotted in Fig. 4-14. It is clear from Fig. 4-14 that the primary stability of the display held very well except for the points in which the digital counts were 5 for each ramp. The small errors may be due to low signal-noise ratio of the colorimeter at dark display levels.

4.2.1.3 Additivity

The tristimulus values for the display white point, black point, and peak RGB primaries are given in Table 4-29. Based on Table 4-29, after black point correction, the additivity of the display could be verified by comparing the tristimulus values for the display white point with the summed tristimulus values of the peak RGB primaries. The results are given in Table 4-30.

Table 4-29. *Measured tristimulus values for display white, black, and peak RGB primaries.*

Digital Counts			Tristimulus Values		
R	G	B	X	Y	Z
0	0	0	0.281	0.298	0.227
255	0	0	34.07	18.50	0.56
0	255	0	21.02	43.03	4.32
0	0	255	8.41	8.12	40.82
255	255	255	63.01	69.12	45.29

Table 4-30. *Measured tristimulus values for display white point and the sum of peak RGB primaries.*

Value	White	R+G+B	Difference (%)
X	62.73	62.66	0.11
Y	68.82	68.76	0.087
Z	45.06	45.02	0.089

The results of less than 0.11% difference for each primary in Table 4-30 indicates that the display additivity held very well. Since the primaries were stable (except for at very

dark display levels) and additive, a simple 3× 3 matrix transform, therefore, could be employed to convert RGB tristimulus values to CIE XYZ tristimulus values.

4.2.2 Characterization of LCD Display

When displaying a spectral image on LCD screen, some transformation models are required to transfer XYZ tristimulus values of spectral images to LCD RGB digital counts, all pixel by pixel applications, for display. Therefore, the LCD display is required to be well modeled, or calibrated. In the following subsections the details of transformation model of LCD display and its color accuracy will be discussed.

4.2.2.1 Primary Transform Matrix

The Matrix transform from RGB scalars (0~1) to XYZ tristimulus values was derived from XYZ measurement of the peak primaries after black point correction. The transform and its inverse are given in Eqs 4-7 and 4-8.

$$\begin{bmatrix} X \\ Y \\ Z \end{bmatrix} = \begin{bmatrix} 33.789 & 20.739 & 8.129 \\ 18.202 & 42.732 & 7.822 \\ 0.333 & 4.093 & 40.593 \end{bmatrix} \cdot \begin{bmatrix} R \\ G \\ B \end{bmatrix}, \tag{4-7}$$

$$\begin{bmatrix} R \\ G \\ B \end{bmatrix} = \begin{bmatrix} 0.03983 & -0.01891 & -0.00433 \\ -0.01722 & 0.03202 & -0.00272 \\ 0.00141 & -0.00307 & 0.02494 \end{bmatrix} \cdot \begin{bmatrix} X \\ Y \\ Z \end{bmatrix}. \tag{4-8}$$

4.2.2.2 Electro-optical Transfer Functions

The electro-optical transfer functions (EOTF) shown in Fig. 4-15 were the relationships between the RGB digital counts used and their corresponding RGB scalars which representing the luminance produced by that digital counts. They were calculated from the measured tristimulus values of RGB ramps using Eq. (4-8) and their corresponding

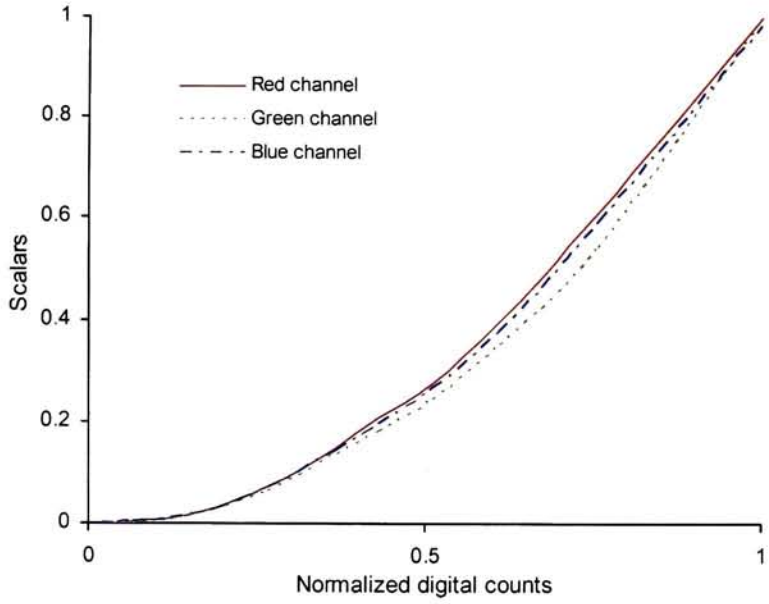

Figure 4-15. *Electro-optical transfer functions for RGB channels.*

RGB digital counts (normalized) for each RGB channel. As recommended in Fairchild and Wyble's work,[75] linear interpolations using three one-dimension lookup tables (LUTs) will perform better than equation fitting method, like GOG model,[68] to describe the electro-optical transfer function for LCD display. Therefore, in this research, cubic-spline interpolation method was employed to interpolate the electro-optical transfer function based on three one-dimension LUTs.

4.2.2.3 Calibration Accuracy and Optimization

There were several paths of transforms in this research. One is so called forward path that LCD display RGB digital counts were transferred to XYZ tristimulus values using electro-optical conversion functions and Eq. 4-7. In this research, spectral images were first converted to XYZ tristimulus values, pixel by pixel. Then those XYZ values were

transferred to XYZ tristimulus values, pixel by pixel, at LCD viewing condition using chromatic adaptation model. Finally, the adapted XYZ values were converted to LCD display RGB digital counts, pixel by pixel, for display based on electro-optical transfer functions and Eq. 4-8. When calculating the color differences for display images, LCD display RGB digital counts should be transferred back to XYZ tristimulus values at LCD viewing condition. The path that transferring from XYZ values to RGB digital counts, and then transferring RGB digital counts back to XYZ values, all at LCD viewing condition, is called loop path. Thus, the colorimetric accuracy of the transform model in both forward and loop paths were required to be investigated. It should be noted here that black correction was required for all tristimulus values involved in transform. However, when calculating the color accuracy of the calibration, the estimated and measured XYZ tristimulus values were required to convert back to their displayed values by adding the XYZ values of the black point. The results of color accuracy for 48 ramps, 17 gray, 42 RND and all 107 data sets are given in Tables 4-31 and 4-32 where Table 4-31 is for forward path and Table 4-32 is for loop path.

The results in Tables 4-31 and 4-32 show that this LCD characterization was very successful in terms of color accuracy, especially in the loop path. However, there was still some space for improvement. As described in previous sections, due to the limit of measurement device and other possible reasons, the XYZ tristimulus values at black point may involve in some errors. Consequently, the transform using black point correction would generate some errors in color reproduction. Thus, an optimization procedure was performed. The objective of this optimization was to minimize the mean

color difference for all 107 data sets at loop path by optimizing the XYZ tristimulus values at the black point and the transfer matrix in Eq. 4-7. The optimized XYZ values for the black point was obtained as [0.278000, 0.294381, 0.224395].

Table 4-31. *Color differences in LCD characterization for forward path.*

	DeltEab			DeltE94		
Samples	Mean	Maximum	Stdev	Mean	Maximum	Stdev
Ramps	0.26	1.30	37.00	0.16	0.79	0.21
Gray	0.14	0.28	0.10	0.12	0.24	0.09
RND	1.11	5.79	1.15	0.70	4.03	0.79
All Data	0.57	5.79	0.87	0.36	4.03	0.58

Table 4-32. *Color differences in LCD characterization for loop path.*

	DeltEab			DeltE94		
Samples	Mean	Maximum	Stdev	Mean	Maximum	Stdev
Ramps	0.27	1.34	0.37	0.16	0.79	0.21
Gray	0.04	0.16	0.05	0.04	0.16	0.05
RND	0.30	1.22	0.23	0.18	1.11	0.19
All Data	0.25	1.34	0.30	0.15	1.11	0.19

The corresponding optimized transform equations are given in Eqs. 4-9 and 4-10.

$$\begin{bmatrix} X \\ Y \\ Z \end{bmatrix} = \begin{bmatrix} 33.780 & 20.737 & 8.241 \\ 18.204 & 42.812 & 7.785 \\ 0.337 & 4.116 & 41.295 \end{bmatrix} \cdot \begin{bmatrix} R \\ G \\ B \end{bmatrix}, \tag{4-9}$$

$$\begin{bmatrix} R \\ G \\ B \end{bmatrix} = \begin{bmatrix} 0.03981 & -0.01886 & -0.00439 \\ -0.01718 & 0.03202 & -0.00259 \\ 0.00139 & -0.00303 & 0.02451 \end{bmatrix} \cdot \begin{bmatrix} X \\ Y \\ Z \end{bmatrix}. \tag{4-10}$$

The whole characterization procedures, including the electro-optical transfer functions, were then re-applied using the optimized results. The new electro-optical transfer functions were almost the same as that shown in Fig. 4-17 and are not displayed here. The color accuracy in LCD calibration was re-evaluated based on new electro-

optical transfer functions and optimized transform equations, Eqs. 4-9 and 4-10. The results are given in Tables 4-33 and 4-34.

Table 4-33. *Color differences in LCD* characterization *for forward path after optimization.*

	DeltEab			DeltE94		
Samples	Mean	Maximum	Stdev	Mean	Maximum	Stdev
Ramps	0.14	1.64	0.24	0.09	0.71	0.11
Gray	0.09	0.32	0.07	0.08	0.32	0.07
RND	1.03	5.65	1.16	0.61	3.80	0.78
All Data	0.48	5.65	0.86	0.29	3.80	0.55

Table 4-34. *Color differences in LCD* characterization *for loop path after optimization.*

	DeltEab			DeltE94		
Samples	Mean	Maximum	Stdev	Mean	Maximum	Stdev
Ramps	0.11	0.50	0.08	0.07	0.25	0.05
Gray	0.04	0.32	0.08	0.04	0.32	0.08
RND	0.21	0.66	0.02	0.13	0.59	0.14
All Data	0.14	0.66	0.14	0.09	0.59	0.10

The results in Table 4-34 show the color accuracy in loop path had been significantly improved. This accuracy in color characterization of the LCD display would provide sufficient confidence in success for accurately displaying the spectral images for the visual assessment experiment.

4.2.3 Chromatic Adaptation Transform

Before leaving the section of LCD calibration, we will discuss the chromatic adaptation transform applied in this research. As we described above, to render the spectral images on LCD display, the spectral images were first converted to XYZ tristimulus values using illuminant D_{65} and CIE 2° observer, pixel by pixel. Then the XYZ images were required to transfer to the XYZ values at LCD viewing condition for rendering. This was an issue of color reproduction in cross-media. As described in Chapter 2, chromatic-adaptation

transform is required to apply when dealing with color reproduction in cross-media. The chromatic-adaptation transform applied in this research was based on Fairchild's revision model of CIECAM97s.[49] Also, the transform application was performed for each pixel of XYZ images that were converted from spectral images.

Assuming the adapting field luminance (at D_{65} illuminant viewing condition) is 318.31 cd/m^2. The luminance of LCD white point was measured as 112.2 cd/m^2. Then the luminance values used for adaptation transform would be La_1 = 0.2×318.31 cd/m^2 and La_2 = 0.2× 112.2 cd/m^2. The tristimulus values for both the sample and white were transformed to spectrally-sharpened cone responses using Eqs. 4-11 and 4-12 respectively.

$$\begin{bmatrix} R_1 \\ G_1 \\ B_1 \end{bmatrix} = M \cdot \begin{bmatrix} X_1 \\ Y_1 \\ Z_1 \end{bmatrix}, \tag{4-11}$$

$$\begin{bmatrix} R_{w1} \\ G_{w1} \\ B_{w1} \end{bmatrix} = M \cdot \begin{bmatrix} X_{w1} \\ Y_{w1} \\ Z_{w1} \end{bmatrix}, \tag{4-12}$$

where the subscript indices *1* and *w1* represent the sample and white respectively, *R*, *G*, *B* here represent the cone responses, and the transformation matrix *M* is defined in Eq. 4-13.

$$M = \begin{bmatrix} 0.8562 & 0.3372 & -0.1934 \\ -0.8360 & 1.8327 & 0.0033 \\ 0.0357 & -0.0469 & 1.0122 \end{bmatrix}. \tag{4-13}$$

A von Kries-type chromatic-adaptation transformation was applied to calculate corresponding colors. The equations are given in Eqs. 4-14 to 4-17.

$$R_{c1} = [D_1 \cdot (100/R_{w1}) + 1 - D_1] \cdot R_1, \quad (4-14)$$

$$G_{c1} = [D_1 \cdot (100/G_{w1}) + 1 - D_1] \cdot G_1, \quad (4-15)$$

$$B_{c1} = [D_1 \cdot (100/B_{w1}) + 1 - D_1] \cdot B_1, \quad (4-16)$$

$$D_1 = F_1 - F_1/[1 + 2 \cdot La_1^{1/4} + La_1^2/300], \quad (4-17)$$

where the subscript index *c1* represents the corresponding colors, D_1 is used to specify the degree of adaptation, F_1 is factor of adaptation degree and was selected 1.0 for average surround in this research. Similar transformations were also made for the XYZ tristimulus values in LCD conditions as given in Eqs. 4-18 to 4-23.

$$\begin{bmatrix} R_2 \\ G_2 \\ B_2 \end{bmatrix} = M \cdot \begin{bmatrix} X_2 \\ Y_2 \\ Z_2 \end{bmatrix}, \quad (4-18)$$

$$\begin{bmatrix} R_{w2} \\ G_{w2} \\ B_{w2} \end{bmatrix} = M \cdot \begin{bmatrix} X_{w2} \\ Y_{w2} \\ Z_{w2} \end{bmatrix}, \quad (4-19)$$

$$R_{c2} = [D_2 \cdot (100/R_{w2}) + 1 - D_2] \cdot R_2, \quad (4-20)$$

$$G_{c2} = [D_2 \cdot (100/G_{w2}) + 1 - D_2] \cdot G_2, \quad (4-21)$$

$$B_{c2} = [D_2 \cdot (100/B_{w2}) + 1 - D_2] \cdot B_2, \quad (4-22)$$

$$D_2 = F_2 - F_2/[1 + 2 \cdot La_2^{1/4} + La_2^2/300], \quad (4-23)$$

where the subscript indices *2, w2 and c2* represent the sample, white and corresponding colors on LCD condition respectively, F_2 was selected as 0.9 for dim surround. Since the corresponding colors should be the same for the same samples, by combining Eqs. 4-14 to 4-16 and Eqs 4-20 to 4-22, we then have

$$R_2 = R_1 \cdot [D_1 \cdot (100/R_{w1}) + 1 - D_1]/[D_2 \cdot (100/R_{w2}) + 1 - D_2], \quad (4-24)$$

$$G_2 = G_1 \cdot [D_1 \cdot (100/G_{w1}) + 1 - D_1]/[D_2 \cdot (100/G_{w2}) + 1 - D_2], \quad (4-25)$$

$$B_2 = B_1 \cdot [D_1 \cdot (100/B_{w1}) + 1 - D_1]/[D_2 \cdot (100/B_{w2}) + 1 - D_2]. \quad (4-26)$$

The cone responses R_2, G_2, and B_2 were then transferred back to XYZ tristimulus values at LCD viewing condition given in Eq. 4-27 where M^{-1} is matrix inverse of M. Those XYZ values could then be converted to LCD digital counts for rendering using LCD matrix transform model and electro-optical transfer function described in previous sections.

$$\begin{bmatrix} X_2 \\ Y_2 \\ Z_2 \end{bmatrix} = M^{-1} \begin{bmatrix} R_2 \\ G_2 \\ B_2 \end{bmatrix}. \quad (4-27)$$

4.3 Visual Experiment for Image Quality

To analyze the image quality of the spectral imaging systems simulated above, the simulated spectral images were used in the visual assessment experiment. Due to the time limit for people to participate in the visual assessment, the experiment was carefully designed.

4.3.1 Selection of Target Images

Face spectral images were simulated using five wavelength steps, two different basis function sets and four levels of noise. Therefore, for one imaging object, there would be 30 simulated spectral images when simultaneous variations were included (5 steps × 2basis functions × 3 noise levels = 30 images). When including the original imaging object, there were total of 31 images for image quality comparison. Two imaging objects were selected for quality experiment. They were one Caucasian and one Black. The

Caucasian one was selected to represent the light-pigmented faces while the Black one for the heavy-pigmented faces. Their images for rendering are shown in Fig. 4-16.

Figure 4-16. *Rendered images of two spectral imaging objects for face imaging system.*

For IBM DCS spectral imaging system, 45 spectral images would be simulated for one imaging object when simultaneous variations are included (5 steps × 3 basis function sets × 3 noise levels = 45 images). There was a total 46 images (including the original imaging object) for image quality comparison for one imaging object. Two spectral imaging objects were selected for simulation. One was painting spectral image and another was spectral image of real fruit scene. Their rendered spectral images are shown in Fig. 4-19. Total of 154 different spectral images, therefore, would be used in the image quality assessment experiment.

The size of the original spectral images for human portrait were 2,048×2,560 pixels. For visual experiment, the spectral images for rendering were resized to 512×640 pixels. The resizing procedure was performed at the last stage of processing after the spectral

images had been converted to RGB images for LCD to rendering. The image sizes for fruit and painting images were 550x367 pixels.

Figure 4-17. *Rendered images of two spectral imaging objects for IBM DCS Camera.*

4.3.2 Visual Experiment Design

An interface, written in IDL programming environment, was built to render the images and record the quality scores in the visual experiment. Fig. 4-18 shows the interface screen for visual experiment. Two images were displayed for observers to judge the image quality. The image on the left side was one of the four rendering original spectral imaging objects and the right side was itself or a corresponding simulation using different wavelength steps, noise levels and basis functions. When displaying on the screen in experiment, both the order of four different original images on the left and the order of their corresponding reproductions on the right were randomly selected by the IDL interface program. Once the observer selected the quality score (by clicking the score button as shown in Fig. 4-18) for the image on the right side based on the original image on the left, a new pair of images would show up automatically. This procedure kept going until all image pairs were compared. The quality scores were recorded automatically.

The viewing distance from the observer to LCD was selected as 60cm (23.6inch). With 86 ppi for LCD resolution, the visual resolution was estimated as approximately 35.5 cycles per degree (cpd) using Eq. 4-28. In other words there were 41 digital samples per degree of visual angle.

$$cpd = \frac{\pi}{180 \cdot \tan^{-1}(\frac{ppi}{d})}, \qquad (4-28)$$

where d is the viewing distance in inches.

***Figure 4-18**. Interface for visual experiment.*

4.3.3 Visual Experiment

A total of 32 observers, 18 experts and 14 novices, participated in this visual assessment experiment. Each image was compared to its original and repeated three times with

random order displayed for the observers. The following instructions were provided to the observers:

"This is an image quality visual experiment. We will display two images each time. The image on the left side is the original image, the image on the right side is the reproduction or the original one. Your task is to assign an image quality score to the right side image based on its overall image quality compared to its original on the left side. The quality score definitions are given as the following:

5: Excellent, no distortion is perceptible

4: Good, distortion is perceptible, but not annoying

3: Not good, not bad, slightly annoying

2: Poor, Annoying

1: Very poor, very annoying

0: Bad

You can also assign the score using steps of 0.5.

Thank you for your help and enjoy the experiment."

The experiment was performed in the dark room.

4.4 Comparative Image Quality Analysis

The image quality subjective scores were collected from the image quality assessment experiment. In the following subsections we investigate the relationship between the objective and subjective image quality values.

4.4.1 Basic Analysis of Visual Experiment Data

4.4.1.1 MOS values

The MOS (mean opinion score) was computed from image quality scores from image quality visual assessment experiment using Eq. 4-29. As provided in Eq. 4-29 the

observers were asked to assign a score A(i,k) to each image displayed on the right side on the LCD screen, where A(i,k) was the score given by the *ith* observer to image *k*. For each reproduced image, the scores were averaged to obtain the MOS value for a specific image where *n* donates the number of observers.

$$MOS(k) = \frac{1}{n}\sum_{i=1}^{n} A(i,k). \qquad (4-29)$$

To compare the differences of image quality scores obtained from expert and novice observers, the relationship of MOS from the novice observers versus MOS from the expert observers is plotted in Fig. 4-19.

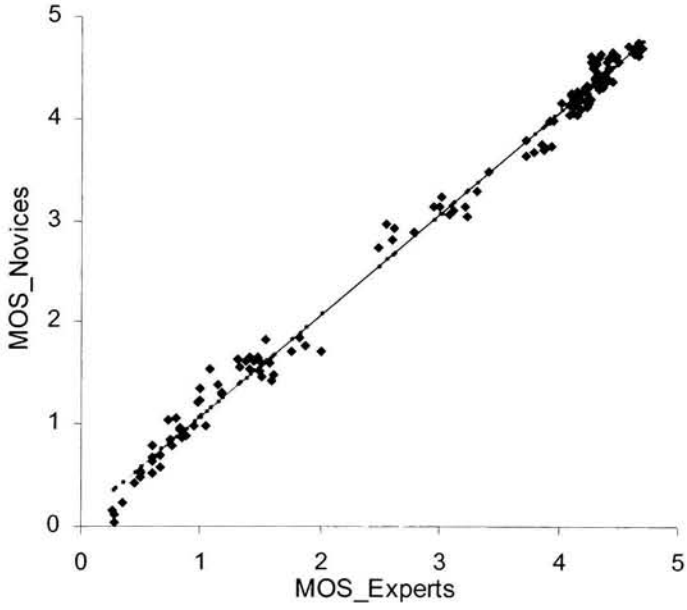

Figure 4-19. *MOS from novice observers vs. MOS from expert observers.*

The correlation coefficient between MOS values from the expert and novice observers is 0.9961. Fig. 4-19 shows that MOS values obtained from experts and novices correlates very well. However, it also indicates some drawbacks of experiment design that the MOS values are not uniformly covered the range of 1~5; there are too few

images whose MOS values fall into the range of 2 ~ 4. The variation of image quality scores was estimated by the standard deviations of MOS values. The relationship between the standard deviations of MOS obtained from novice observers and the corresponding standard deviations of MOS obtained from expert observers is plotted in Fig. 4-20. The corresponding correlation coefficient is 0.9998.

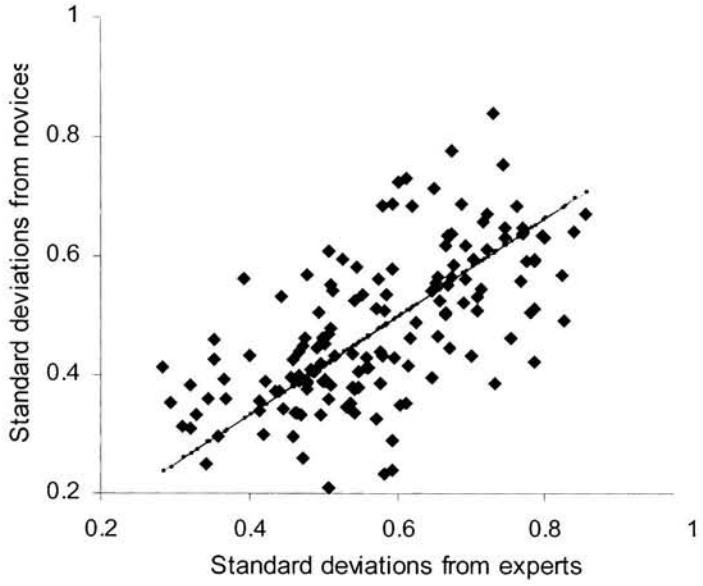

Figure 4-20. *Standard deviations of MOS obtained from novice observers vs. corresponding standard deviations of MOS obtained from expert observers.*

The mean standard deviation of MOS values obtained by experts is 0.57 while this value is 0.48 for novices. This indicates that the image quality scores assigned by the experts have more variation than that assigned by the novices. Since the MOS values obtained from expert and novice observers are highly correlated, as shown in Fig. 4-19 and Fig. 4-20, in the following they will not be discussed separately.

The MOS values for four image sets are shown in Fig. 4-21 where MOS values are plotted in terms of different number of basis functions.

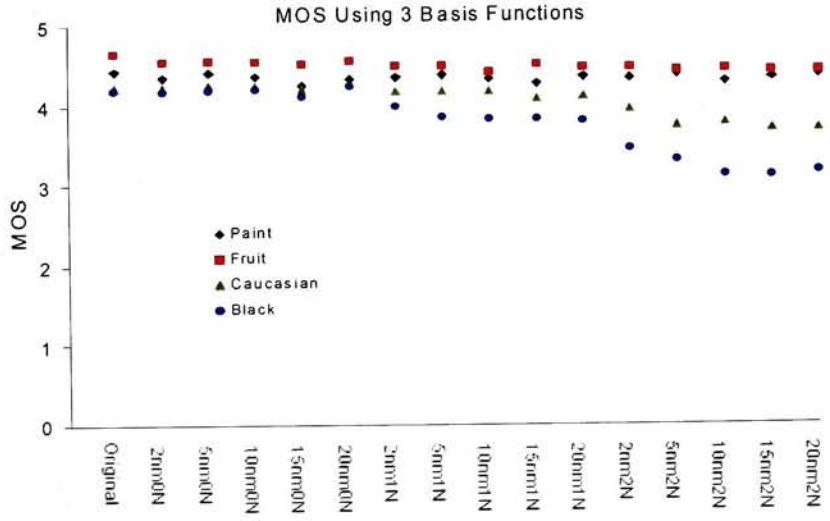
MOS Using 3 Basis Functions
MOS
5
4
3
2
1
0
Paint
Fruit
Caucasian
Black
Original
2nm0N
5nm0N
10nm0N
15nm0N
20nm0N
2nm1N
5nm1N
10nm1N
15nm1N
20nm1N
2nm2N
5nm2N
10nm2N
15nm2N
20nm2N

(a)

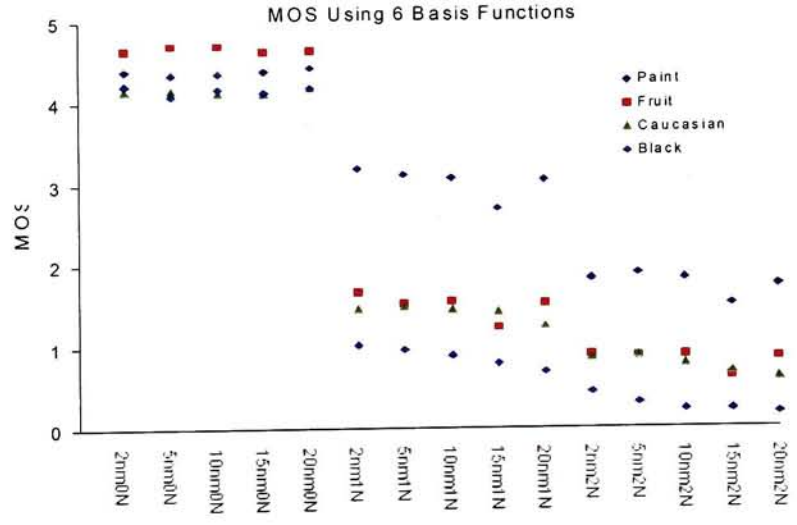
MOS Using 6 Basis Functions
MOS
5
4
3
2
1
0
Paint
Fruit
Caucasian
Black
2nm0N
5nm0N
10nm0N
15nm0N
20nm0N
2nm1N
5nm1N
10nm1N
15nm1N
20nm1N
2nm2N
5nm2N
10nm2N
15nm2N
20nm2N

(b)

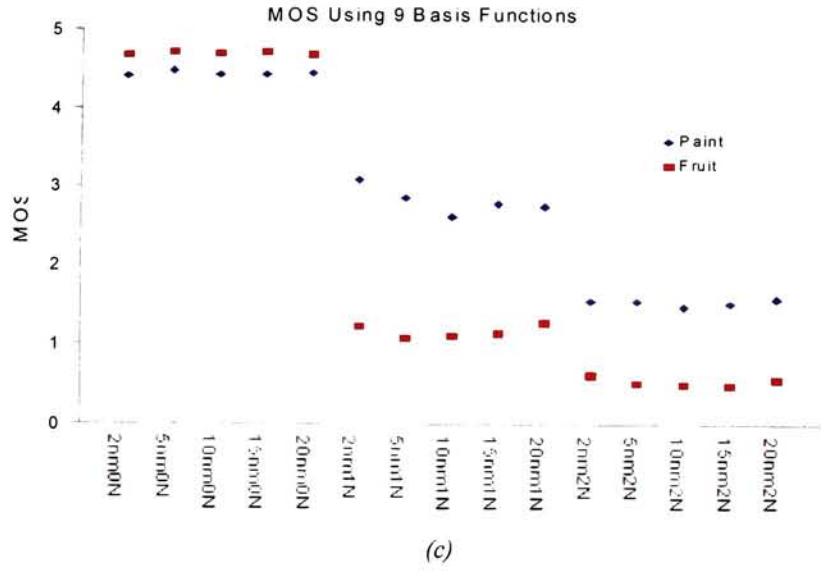

(c)

Figure 4-21. *MOS values from image quality visual experiment.*
(a) Using 3 basis functions; (b) using 6 basis functions; (c) using 9 basis functions

In Fig. 4-21, the notation Original represents the original images, 10nm1N represents the reproduced images using 10nm step in wavelength and 1 percent noise under a certain number of basis functions. The rest of the notations apply similar definitions. The same notation will also be applied from Fig. 4-22 to Fig. 4-25. Fig. 4-21 indicates that image quality, as we expected, does relate to the number of channels or basis functions used in the imaging system when noise is involved. Considering Fig. 4-21(a), when using 3 basis functions image quality was not significantly affected by the noise involved in the capture stage (within the noise range used in this experiment) for the relatively complex paint and fruit image sets. On the other hand, image quality was relatively more sensitive to noise for portrait image sets. This may be due to observers' greater ability to judge the noise appearing on human faces compared to that of more complex scene images of paint and fruit. The human portrait images contain greater regions of low spatial frequency

content. With the same noise levels, generally speaking, wavelength steps had no significant impact on image quality for all four image sets.

When using 6 basis functions as shown in Fig. 4-21(b), the image quality was impacted significantly by different noise levels; more noise provided lower image quality. Image quality of paint image sets was less sensitive to the noise compared to that for other three image sets. This may be due to the fact that paint image sets contained relatively more high frequency information and could mask much of the noise effect compared to that of other three image sets. Generally speaking, with the same noise levels, the wavelength steps played no significant effect to the image quality for all four image sets with the exception of using wavelength step of 15nm for paint and fruit image sets. The reason is unknown at this stage.

When using 9 basis functions for paint and fruit image sets as shown in Fig. 4-21(c), the image quality effects were similar to those discussed for Fig. 4-21(b). Considering image quality using different number of basis functions, the image quality was impacted significantly; more basis functions or channels used, more noise effect shown and poor image quality. This is consistent with the noise propagation theory in multi-spectral imaging system proposed by Burns. [9]

4.4.1.2 Color difference factor values

The color difference factor values for all image sets using different basis functions are plotted in Fig. 6. Caution should be paid for different scales used in Fig. 4-22. Fig. 4-22 indicates that the color difference of all image sets were impacted significantly by noise; more basis functions used and more noise involved, the larger the color difference for the

images. Under the same noise levels, for paint and fruit image sets, the color difference was not significantly sensitive to different wavelength steps used with one exception of using 15nm step while applying 6 basis functions. On the other hand, under the same

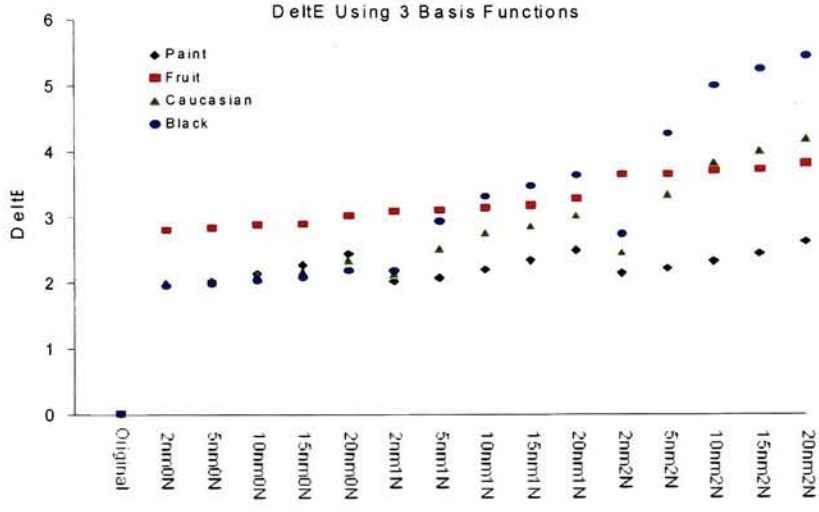

(a)

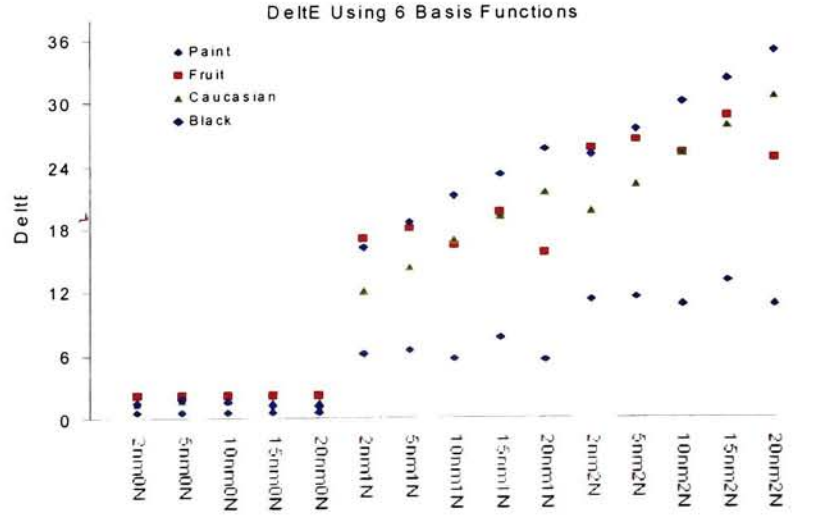

(b)

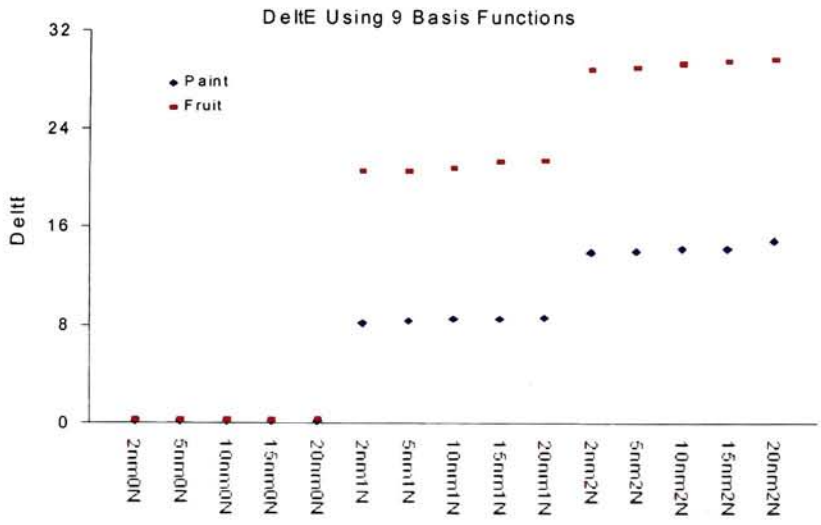

(c)

Figure 4-22. *Color difference factor values from image quality visual experiment. (a) Using 3 basis functions; (b) using 6 basis functions; (c) using 9 basis functions*

noise levels, the color difference was significantly impacted by using different wavelength steps for portrait image sets; the larger the wavelength steps, the larger the image color difference. The reason is because it is more difficult for human observers to detect the color difference in relatively-complex scene images, such as paint, due to the noise masking effect of high frequency image content, than that for the images of relatively lower frequency content, such as human portraits. This also suggests that to get the same quality of images, a higher quality imaging system is required for human portraits than that for other relatively-complex scene images.

4.4.1.3 Graininess factor values

The graininess factor values for all images sets applying different basis functions are calculated and plotted in Fig. 4-23. The situations shown in Fig. 4-23 are very similar to

that of color difference factor values, as shown in Fig. 4-22, since the correlation coefficient between graininess factor and color difference is as high as 0.9027. The relationship between graininess factor and color difference factor is demonstrated in Fig. 4-24. Therefore, we will not discuss in details here.

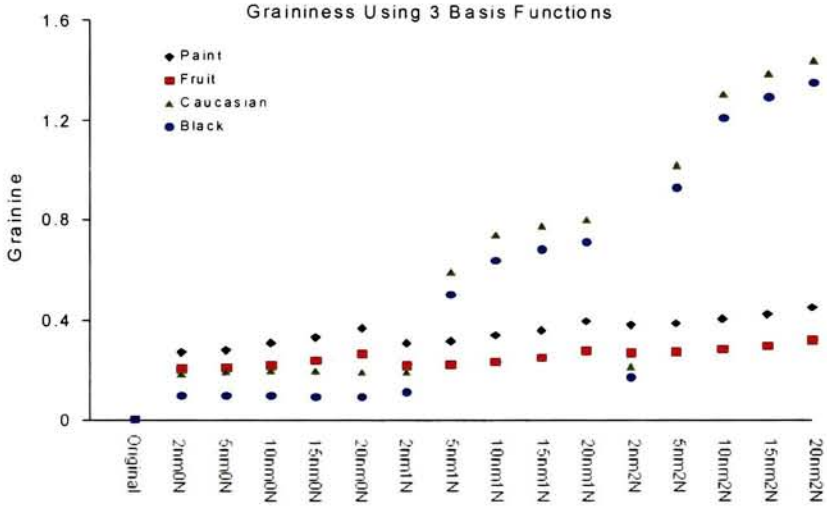

(a)

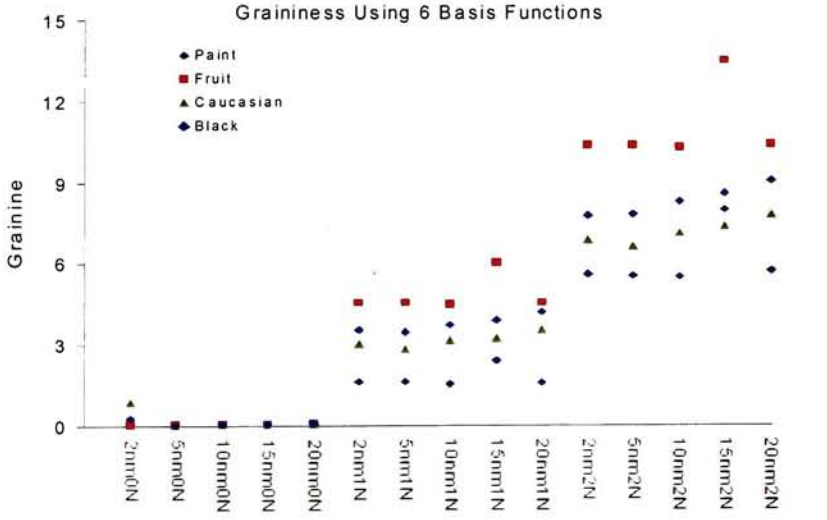

(b)

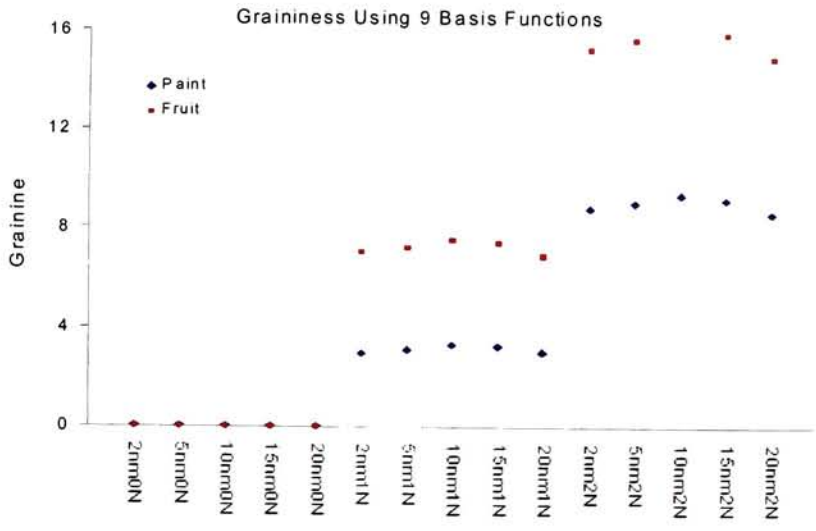

(c)

Figure 4-23. *Graininess factor values from image quality visual experiment. (a) Using 3 basis functions; (b) using 6 basis functions; (c) using 9 basis functions.*

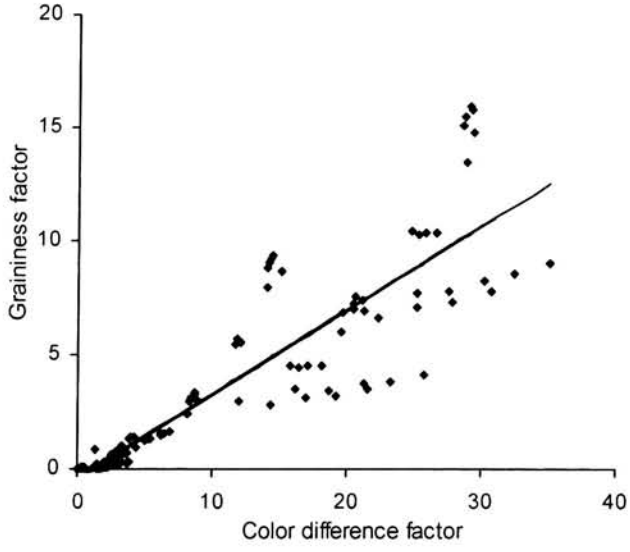

Figure 4-24. *The relationship between graininess factor and color difference factor.*

4.4.1.4 Sharpness factor values

The sharpness factor values of all image sets are plotted in Fig. 4-25. Overall, different noise levels and wavelength steps did not significantly impact the sharpness factor of paint image sets. The sharpness factor was also not significantly impacted by different wavelength steps. Considering the Fig. 4-25(a) and 4-25(b), sharpness factor was more sensitive to the noise for the black image sets. Fig. 4-25 also indicates that, more or less distinct, the sharpness factor of spectral images is more sensitive to noise when more basis functions are employed; the more basis functions employed and the more noise (within the range of this experiment), the sharper of the images. This is a combined phenomenon reported by Johnson & Fairchild[77] and the results in chapter 3 of this research. The results in chapter 3 indicated that the spectral images were sharper when more basis functions were used. This may be probably also partly due to greater noise.

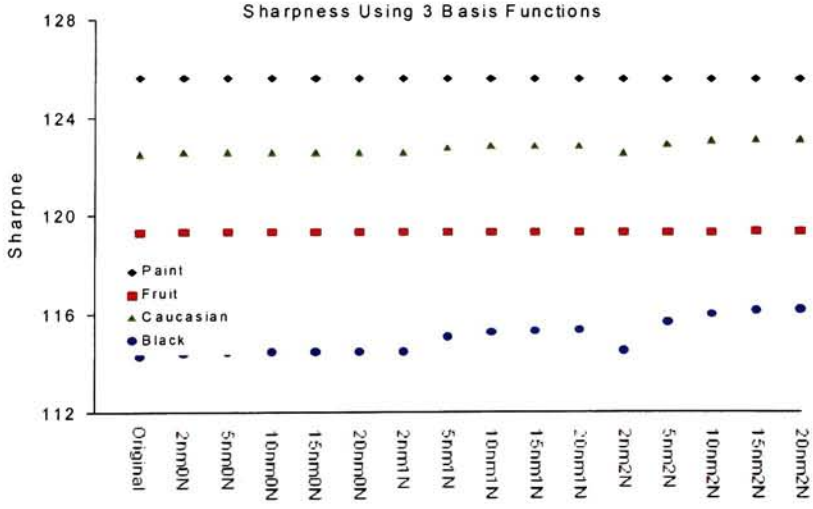

(a)

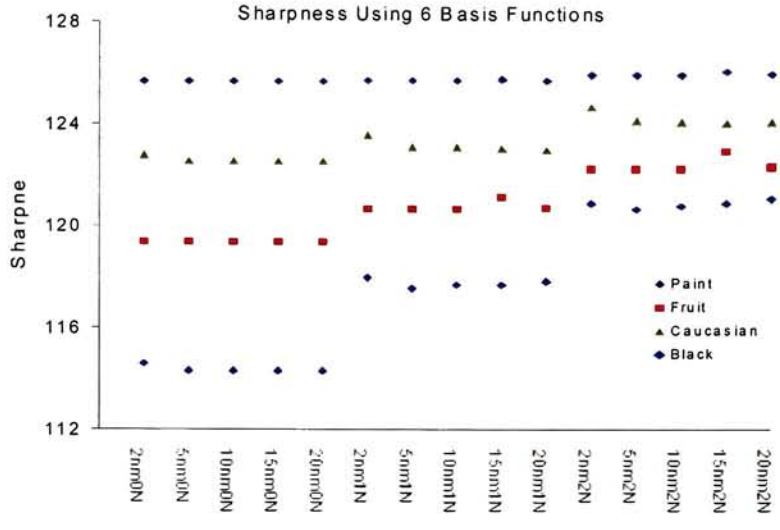

(b)

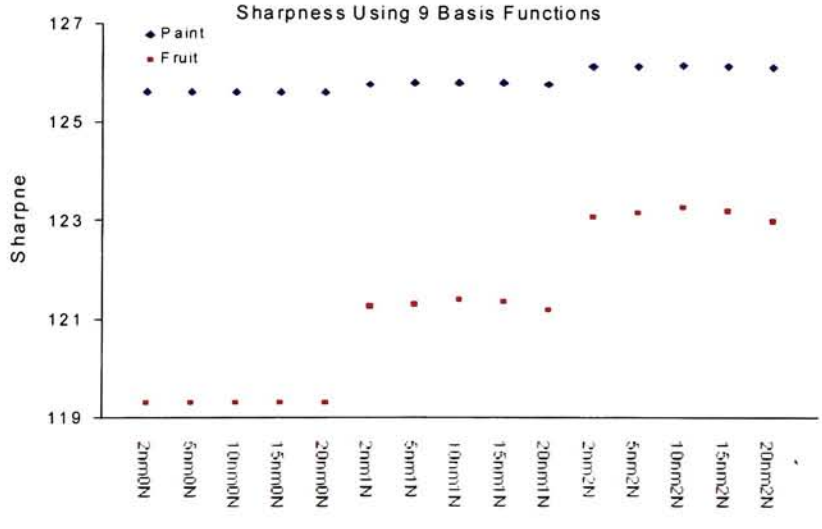

(c)

Figure 4-25. *Sharpness factor values from image quality visual experiment. (a) Using 3 basis functions; (b) using 6 basis functions; (c) using 9 basis functions*

Johnson and Fairchild indicated that additive noise, up to a certain amount, increased perceived sharpness.

4.4.1.5 Contrast factor values

The contrast factor values of all image sets are plotted in Fig. 4-26. Contrast factor was not significantly impacted by different levels of additive noise and different wavelength steps when using three basis functions as shown in Fig. 4-26(a). However, the contrast factor showed three distinct groups when using six basis functions, as shown in Fig. 4-26(b). The contrast of portrait images increased with more additive noise. However, the contrast of paint images displayed just the opposite direction of portrait images. The contrast of fruit image sets, on the other hand, showed their own distinct characteristics. With one percent additive noise, the contrast of fruit images decreased. The contrast of fruit images would then increase when adding two percent noise. When using nine basis

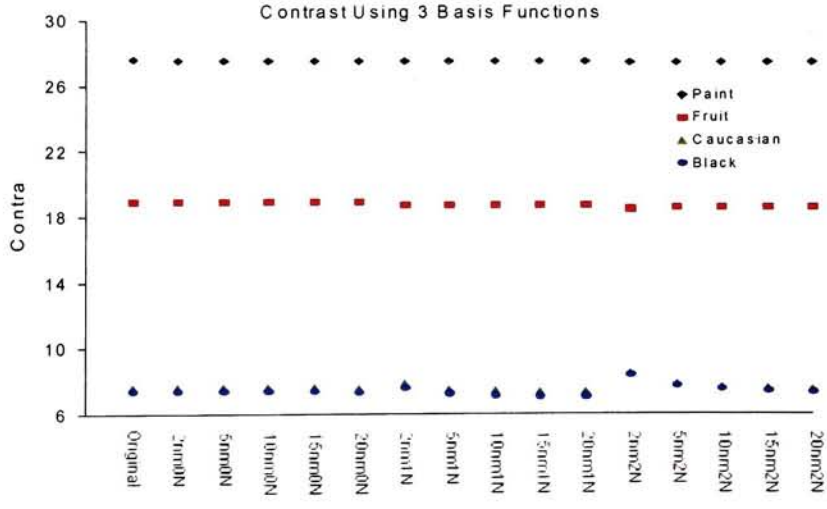

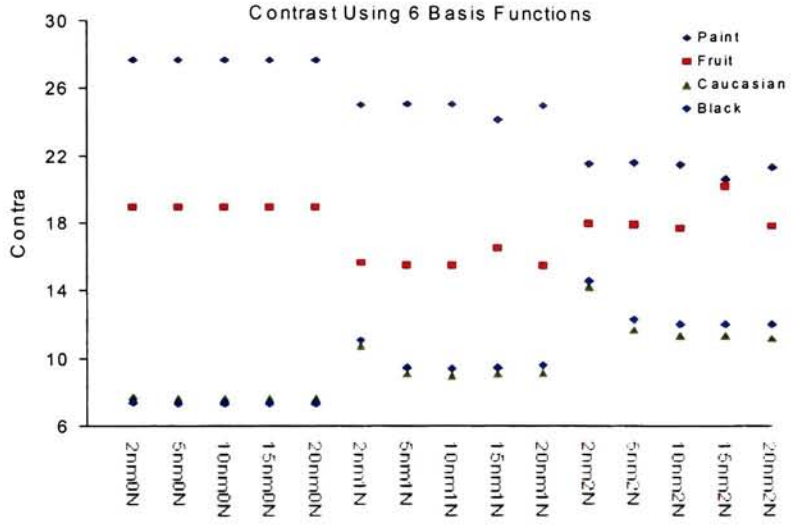

(b)

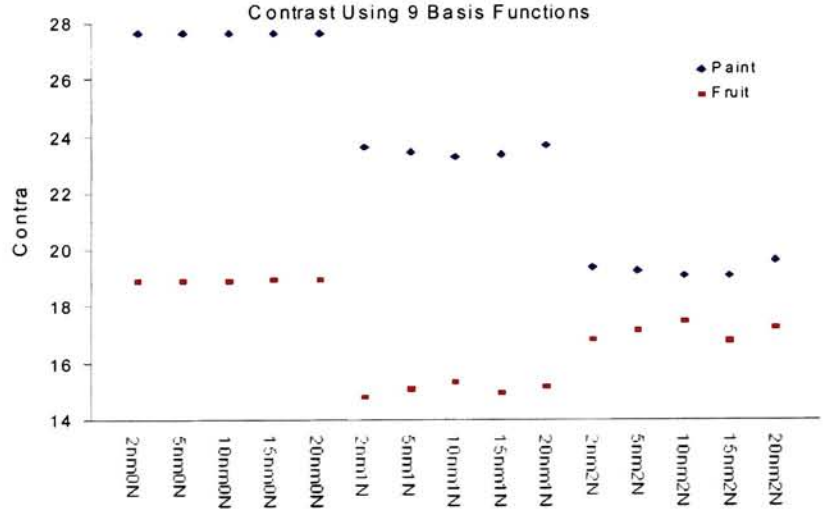

(c)

Figure 4-26. *Contrast factor values from image quality visual experiment. (a)Using 3 basis functions; (b) using 6 basis functions; (c) using 9 basis functions*

functions, as shown in Fig. 4-26(c), the contrast of paint and fruit images displayed the similar characteristics as in Fig. 4-26(b). Overall, the wavelength steps did not significantly impact contrast for all four image sets.

4.4.2 MOS vs. Color Difference Factor

The procedure to calculate the color differences for color images was described in section 2.3.6. In this research an MTF of LCD display would be added after filtering opponent channels before they were transformed back into CIE XYZ space as described in section 2.3.6. The MTF was added to the luminance channel only. The MTF of the LCD display was derived based on Barten's[76] method with some practical modification. The details of derivation are given in the Appendix C. The derived MTF is given in Eq. 4-30

$$MTF(f) = \left| \frac{\sin(1.2k \cdot \pi \cdot f)}{1.2k \cdot \pi \cdot f} \right|, \qquad (4-30)$$

where k is the pixel distance of LCD display in visual angle, f is the frequency. The MTF is plotted in Fig. 4-27.

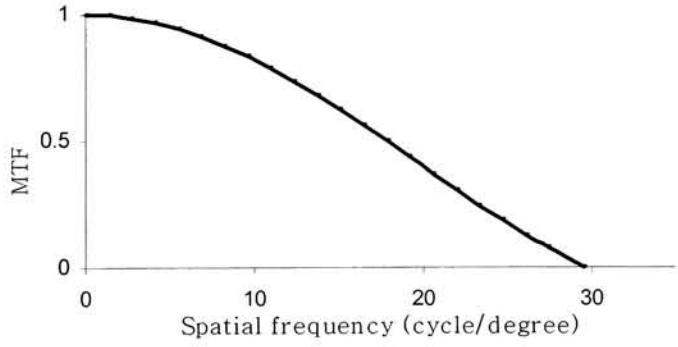

Figure 4-27. *MTF of LCD display.*

The color differences between original spectral imaging objects and their corresponding reproductions were then calculated and their mean values were obtained.

The relationship between the MOS (mean opinion score) values and their corresponding mean color differences obtained above is shown in Fig. 4-28.

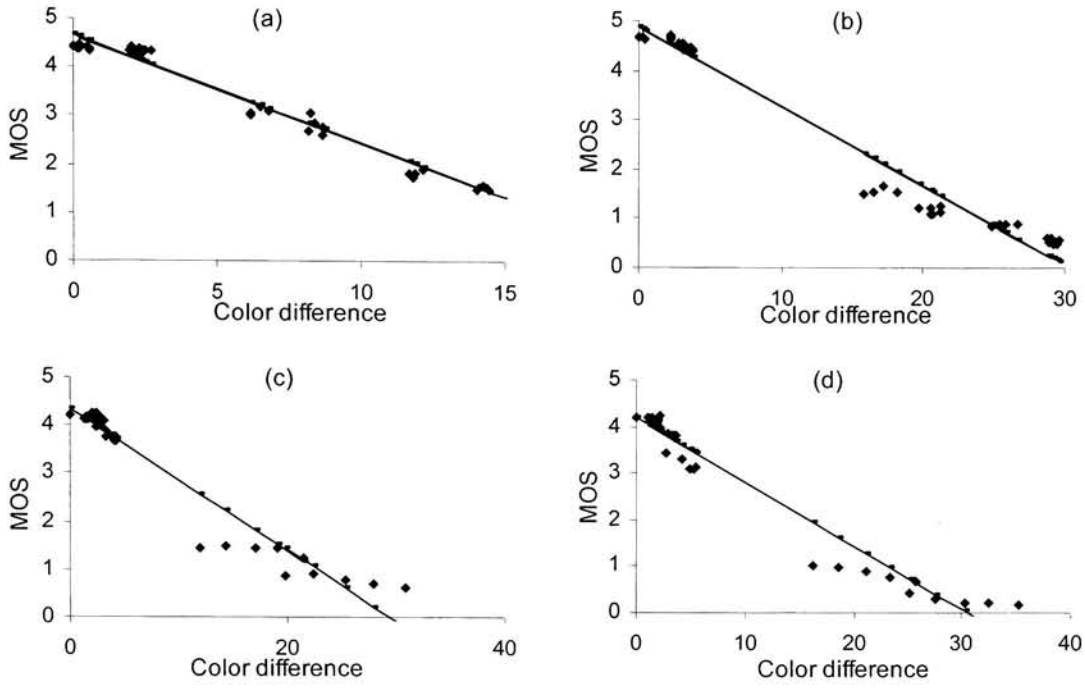

Figure 4-28. *MOS vs. mean image color differences. (a) for painting images; (b) for fruit images; (c) for Caucasian images; (d) for Black images.*

The correlations between MOS values and mean color differences were 0.9876, 0.9865, 0.9706 and 0.9762 with R^2 values of 0.9754, 0.9732, 0.9420 and 0.9529 in linear regression for Figs. 4-28(a) to (d) respectively. However, Fig. 4-28 indicates that the relationship between MOS values and mean color differences is image dependent, which means the same MOS values may have different mean color differences for different images. This suggests that the image quality is not a single function of color difference. Figs. 4-28(a) and (b) show that color differences in the fruit image sets were more noticeable than those in even more complex images of the painting. This might be due to the mechanisms of frequency filtering in the human visual system as described in the

chapter 2. Fig. 4-28 also indicates that larger color differences are proportional to the lower image qualities. In addition, Figs. 4-28(c) and (d) also show, at low image quality around MOS value of 1.0, images with large color difference range will display almost the same in image quality. This might suggest that the definition of image color difference still has space for further improvement in future study.

MOS values and their corresponding standard deviations of image color difference also correlated very well. They are plotted in Fig. 4-29 where the correlation coefficients are 0.984, 0.991, 0.993 and 0.990 for Figs. 4-29(a) to 4-29(d) respectively.

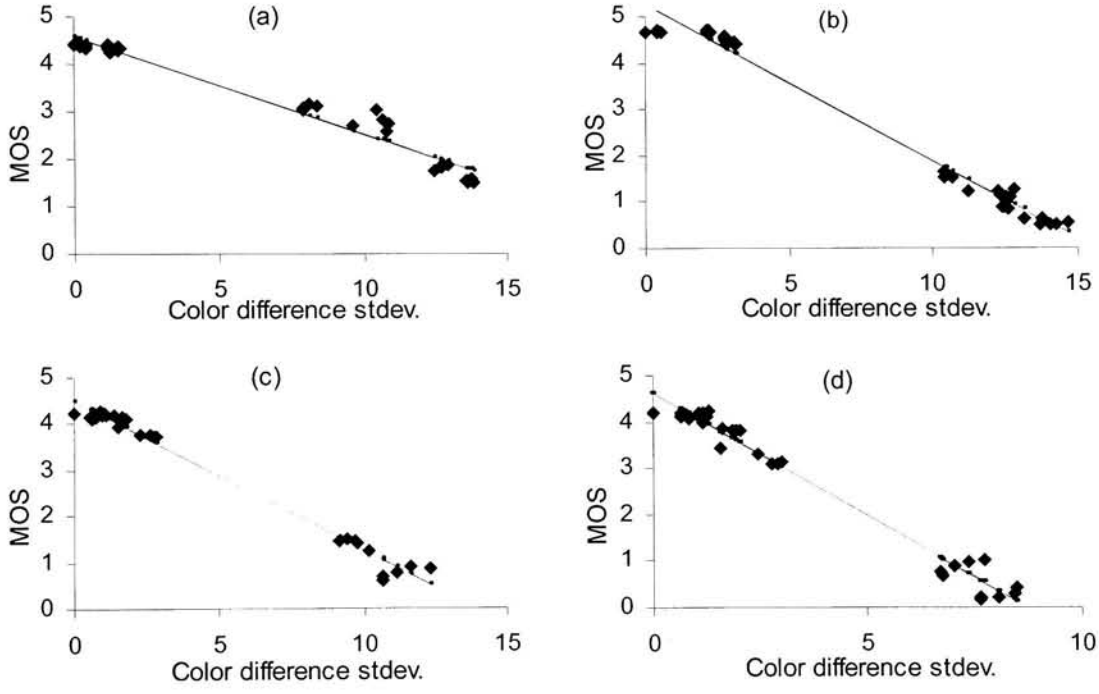

Figure 4-29. *MOS vs standard deviation of image color difference factor.*
(a) painting images; (b) fruit images; (c) Caucasian images; (d) Black images.

In Fig. 4-29, higher standard deviation of image color difference corresponds to lower image quality. Compared to Fig. 4-28, Fig. 4-29 displays better fit of the data, especially in the low image quality range as shown in Fig. 4-29(c) and (d). This may suggest that, to

represent the image quality, the standard deviation of image color difference could be a better choice than the image color difference factor itself defined in this research.

4.4.3 MOS vs. Sharpness Factor

The sharpness factors were calculated using Eqs. 2-26 and 2-27. Instead of using effective display luminance, L values here were calculated using luminance factors given in Eq. 2-28.

$$L = 2 \cdot L_{LCD} \cdot Y / Y_m \,, \tag{4-28}$$

where L_{LCD} = 112.2 cd/m^2 is the luminance of LCD at white point, Y is mean Y tristimulus values of the image and Y_m is the Y tristimulus value of the LCD of the white point. It should be remember that the XYZ tristimulus values were calculated at LCD viewing conditions.

The relationships between MOS (mean opinion score) values and sharpness factors are shown in Fig. 4-30. The sharpness factors correlated with MOS values reasonably well with correlations coefficients of 0.946, 0.9486, 0.8495 and 0.9524 and R^2 values of 0.8955, 0.8998, 0.7217 and 0.9071 in linear regression for Figs. 4-30(a) to (d) respectively. Except for the Caucasian images set, MOS values correlated with sharpness factor values quite well. The reason for Caucasian image set is unknown at this stage and it gives us space for further improvement in future research. As similar to the situation in Fig. 4-28, Fig. 4-30 indicates that the relationship between MOS values and sharpness factor values is image dependent, which means the same MOS values may have different sharpness factor values for different images. This suggests that image quality is also not a single function of sharpness factor. Fig. 4-30(a) indicates that the sharpness factor values

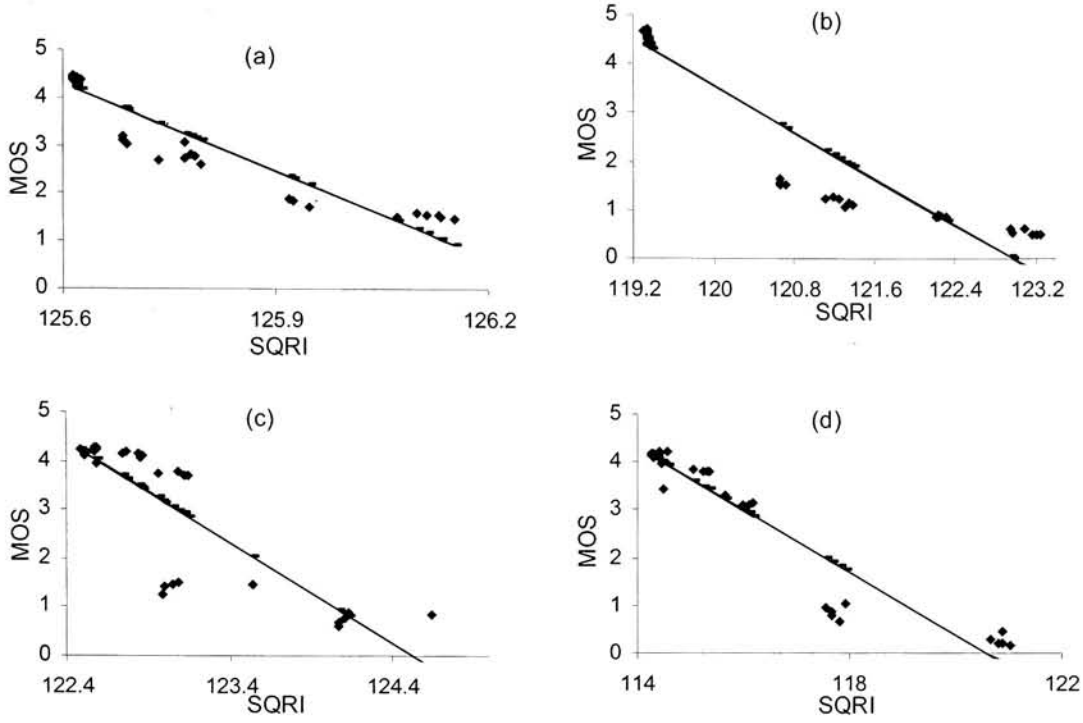

Figure 4-30. *MOS vs. sharpness factor. (a) for painting images; (b) for fruit images; (c) for Caucasian images; (d) for Black images.*

for painting images fell over a very small range compared to other image sets. Fig. 4-30 also shows an interesting phenomenon that the larger sharpness factor values correspond to the lower image qualities in this research. This might be also partly due to the factor that the original images were already sharp enough.

4.4.4 MOS vs. Graininess Factor

Fig. 4-31 shows the relationships between MOS (mean opinion score) values and graininess factor values for painting, fruit, Caucasian and Black image sets respectively. The correlation coefficients between MOS and graininess values for each image set are 0.9506, 0.9254, 0.9350 and 0.9349 with R^2 values of 0.9037, 0.8564, 0.8742, and 0.8741 in linear regression respectively. They correlated reasonably well. Fig. 4-31 indicates that

high graininess value corresponds to low image quality. It also shows that the relationship between MOS and graininess factor is image dependent, hence the image quality cannot be a single function of the graininess factor.

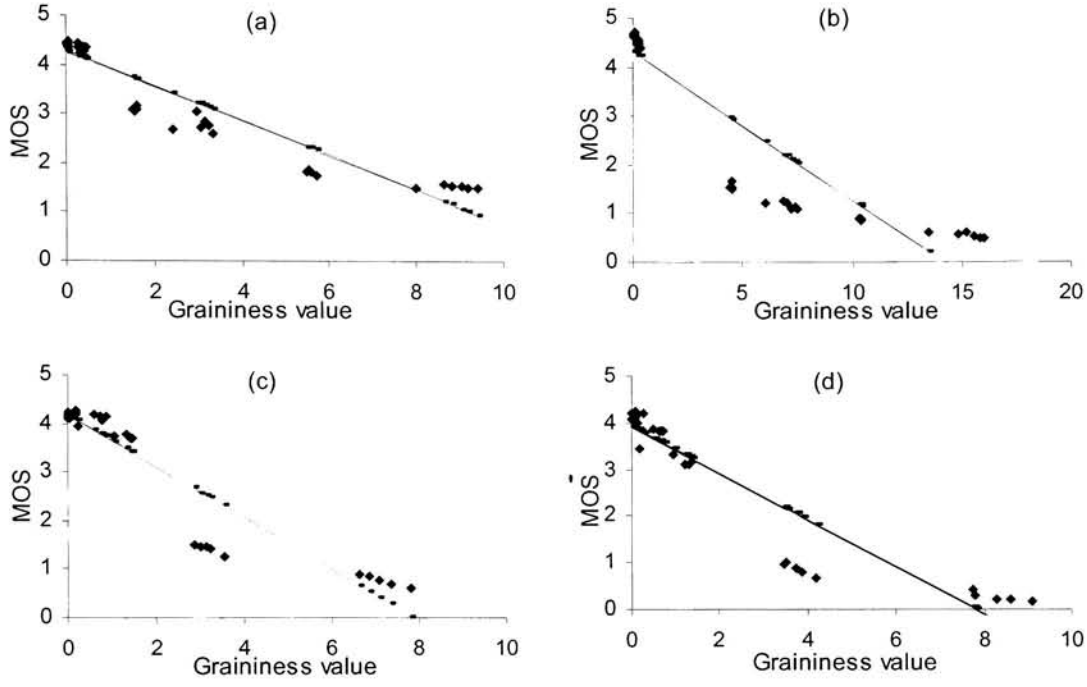

Figure 4-31. *MOS vs. graininess factor. (a) for painting images; (b) for fruit images; (c) for Caucasian images; (d) for Black images.*

4.4.5 MOS vs. Contrast Factor

The relationship between MOS (mean opinion score) values and contrast factor values are shown in Fig. 4-32 where we divided the SIPk values in Eq. 2-29 with 10^3. In the following calculation we will use this new SIPk factor.

The correlation coefficients between MOS values and contrast factor values are 0.988, 0.709, 0.873 and 0.901 with R^2 values of 0.977, 0.503, 0.763 and 0.812 in linear regression for Fig. 4-32. Fig. 4-32 indicates that the relationship between MOS and

contrast factor is image dependent. Figs. 4-32 (a) and (b) show the images with high contrast values display high quality. However, for human portraits, high contrast factor values will display low image quality. The reason is unknown and needs further investigation. Also, the correlations between MOS values and contrast factor values for fruit and Caucasian image sets were not high enough. Those are the issues for future improvement and further investigation.

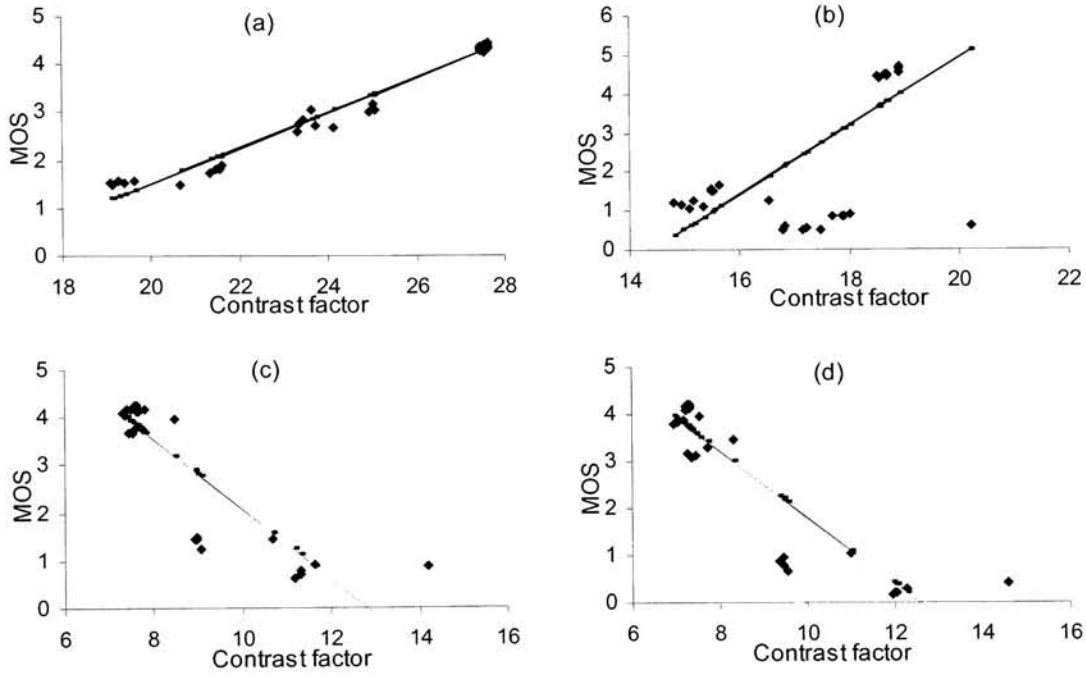

Figure 4-32. *MOS vs. contrast factor. (a) for painting images; (b) for fruit images; (c) for Caucasian images; (d) for Black images.*

4.4.6 Image Quality Metric

To bridge the gap between the physical measures and subjective visual perceptions of the image quality, we proposed to apply Miyahara's[44] objective PQS method. The PQS was calculated from the distortion factors by using the principal components analysis and multiple regression analysis (MRA) with the subjective MOS (mean opinion score)

obtained above. It is hoped that the obtained quality metric, PQS, would have very good correlation with the subjective measure, MOS.

4.4.6.1 Correlations Between the Distortion Factors

The purpose of distortion factors defined in this research was to quantify specific types of impairment in images from spectral imaging systems. Obviously, some of the local image impairment will contribute to several or all distortion factors, and the distortion factors will be correlated. The covariance matrix of distortion factors is given in Table 4-35.

Table 4-35. *Covariance matrix of distortion factors.*

	Color Diff.	Graininess	Sharpness	Contrast
DeltsEab	1.0000	0.9027	0.1182	0.1370
Graininess	0.9027	1.0000	0.2323	0.0119
Sharpness	0.1182	0.2323	1.0000	0.6456
Contrast	0.1370	0.0119	0.6456	1.0000

The covariance matrix indicates that color difference factor is highly correlated with graininess factor. This is probably due to the fact that the graininess factor was defined as the mean RMS error of original and its reproduction images in the luminance channel which is closely related to the color difference. The correlations are low for the rest of the distortion factors.

The PCA is a good tool to quantify these correlations among distortion factors. By performing the PCA to the four distortion factor data sets we computed in previous sections, the cumulative contribution percentages of the first one to four principal components were obtained and are given in Table 4-36.

The results in Table 4-36 indicate that the first three principal components would cover 100% of all variance of four distortion factors. The space spanned by the four

Table 4-36. *Cumulative contribution percentage of principal components for distortion actors*

	Number of principal components			
	1	2	3	4
Cumulative percentage	99.08	99.91	100.00	100.00

distortion factors was essentially three-dimensional. This was consistent with the high correlation between color difference and graininess factors. It suggests that three properly defined distortion factors will describe the impairment of images with the same efficiency as using four distortion factors defined in this research. Furthermore, two properly defined distortion factors will be quite safe to describe most of the coverage of four factors used here since the first two principal components covered as high as 99.91% of the variance as shown in Table 4-35. This provides us some direction for future research.

To investigate the importance of the four distortion factors in describing the image impairment the correlations between the distortion factors and their principal components were calculated. The results are given in Table 4-37.

Table 4-37. *Correlations between distortion factors and their principal components.*

	Principal components		
Factors	1	2	3
DeltE	0.8327	0.8032	0.5358
Graininess	0.7602	0.6633	0.3774
Sharpness	0.3537	0.2892	0.4420
Contrast	0.2090	0.6997	0.6322

Table 4-37 indicates that the first principal component mostly reflected the coverage of color difference and graininess factors since it had high correlations with color difference and graininess factors. Since the first principal component covered most the variance of the distortion factors, it suggests that the color difference and graininess

factors are the most important factors in this research. The correlation between the first principal component and the contrast factor was low that it suggested that the contrast factor contributes very small amount of description in most image distortion. The second principal component still had high correlation with color difference factor. This further proves that the color difference factor was the most important factor in describing the image impairment in this research when using four distortion factors. The second principal component also correlated with graininess and contrast factors over 0.66. Loosely speaking, the order of importance from high to low for the four distortion factors is, color difference, graininess, sharpness and contrast. We will discuss this issue more detail later.

4.4.6.2 Quality Metric PQS

To obtain a numerical distortion measure, or an image quality metric PQS, a multiple regression analysis (MRA) between the principal components and the MOS values was performed. The first three principal components were employed in this task. The detail procedure is described below.

First, we assumed that PQS could be described as a linear combination of principal components of distortion factors. This is a reasonable assumption since it has already shown that the MOS values correlated to the distortion factors very well and the principal components of distortion factors are just linear transformations of distortion factors. Let Z_1, Z_2 and Z_3 be the first three principal components. The PQS could then be given in Eq. 4-29.

$$PQS = \sum_{i=1}^{3} a_i \cdot Z_i , \qquad (4-29)$$

where a_i are the coefficients that need to be determined using least square regression based on MOS values. The results are given in Eq. 4-30 where the correlation between PQS and MOS was 0.9237.

$$PQS = 39.352 \cdot Z_1 + 13.767 \cdot Z_2 - 8.106 \cdot Z_3 . \qquad (4-30)$$

The next step was based on Eq. 4-31 as given below

$$PQS = b_0 + \sum_{i=1}^{3} b_i \cdot Z_i , \qquad (4-31)$$

where b_0 and b_i are the coefficients that need to be determined by minimizing the RMS differences between PQS and MOS. The initial value for b_0 was zero and b_i were assigned the a_i values given in Eq. (4-30). The reason to using two steps with Eqs. 4-29 and 4-31 was to avoid the local minimum in MRA. If Eq. 4-30 was directly performed by assigning arbitrary initial values to b_0 and b_i, the MRA may not be successful due to the local minimum problem. The results for Eq. 4-31 are given in Eq. 4-32 with the new correlation coefficients of 0.9226 between PQS and MOS.

$$PQS = 5.480 - 29.934 \cdot Z_1 + 18.617 \cdot Z_2 - 11.565 \cdot Z_3 . \qquad (4-32)$$

Note that the PQS, which was derived using principal components, could be also expressed in terms of the distortion factors. Let F_1, F_2, F_3 and F_4 be the distortion factors of color difference, graininess, sharpness and contrast respectively. Each principal component could be expressed as a linear combination of the distortion factors as given in Eq. 4-33.

$$Z_j = \sum_{i=1}^{4} s_{ji} F_i, \qquad j = 1,2,3, \qquad (4-33)$$

where s_{ji} are coefficients for the *jth* principal component and need to be determined using least square regression. The results of s_{ji} are given in Table 4-38. The correlations between the principal components and their corresponding estimated values using Eq. 4-33 were all 1.000. This is not surprising since the principal components were calculated from these four distortion factors.

Table 4-38. *Coefficients s_{ji} for Eq. 4-33.*

	Sji			
j	i=1 (1E-2)	i=2 (1E-3)	i=3 (1E-4)	i=4 (1E-3)
1	-0.0243	-0.2908	7.0926	-0.1784
2	-0.5818	0.5067	-5.0540	6.8303
3	1.3631	-21.7076	-17.9214	9.8683

The next step was to perform the MRA for equation as given in Eq. 4-34.

$$Z_j = t_{j0} + \sum_{i=1}^{4} t_{ji} \cdot F_i, \qquad j = 1,2,3, \qquad (4-34)$$

where t_{j0} and t_{ji} are coefficients that need to be determined by minimizing the RMS of the differences between principal components and their corresponding estimated values using Eq. 4-34. The initial values for t_{j0} were zeros. The initial values for t_{ji} were assigned the corresponding s_{ji} values as given in Table 4-38. The reason to play two steps using Eqs. 4-33 and 4-34 was the same as procedures using Eqs. 4-29 and 4-31 to avoid the local minimum in MRA when directly using Eq. 4-34. The results of t_{ji} are given in Table 4-39. The coefficients of t_{ji} ($i \neq 0$) and corresponding s_{ji} were almost the same at limited decimal points. The constant coefficients t_{j0} were of very small values.

Table 4-39. *Coefficients t_{ji} for Eq. 4-34.*

			Tji		
j	i=0 (1E-8)	i=1 (1E-2)	i=2 (1E-3)	i=3 (1E-4)	i=4 (1E-3)
1	2.1512	-0.0243	-0.2908	7.0926	-0.1758
2	2.8455	-0.5818	-0.5067	-5.0540	6.8303
3	1.5125	1.3631	-19.9594	-17.9214	9.8683

The final step was substituting the Eq. 4-34 into 4-32, hence obtaining the PQS expression in terms of distortion factors. The obtained PQS is given in Eq. 4-35.

$$PQS = 5.4797 - 0.2587 \cdot F_1 + 0.2503 \cdot F_2 + 0.0099 \cdot F_3 + 0.0183 F_4. \qquad (4-35)$$

The correlation coefficients between the PQS in Eq. 4-35 and the MOS was 0.9232 that was the same as the results in Eq. 4-32. This was because there was little error involved in the procedure through Eq. 4-32 to Eq. 4-35 due to the fact that principal components could be 100% expressed by the distortion factors. It should be noted that the contrast factor SIPk used here was divided by 10^3 to the SIPk defined in Eq. 2-28.

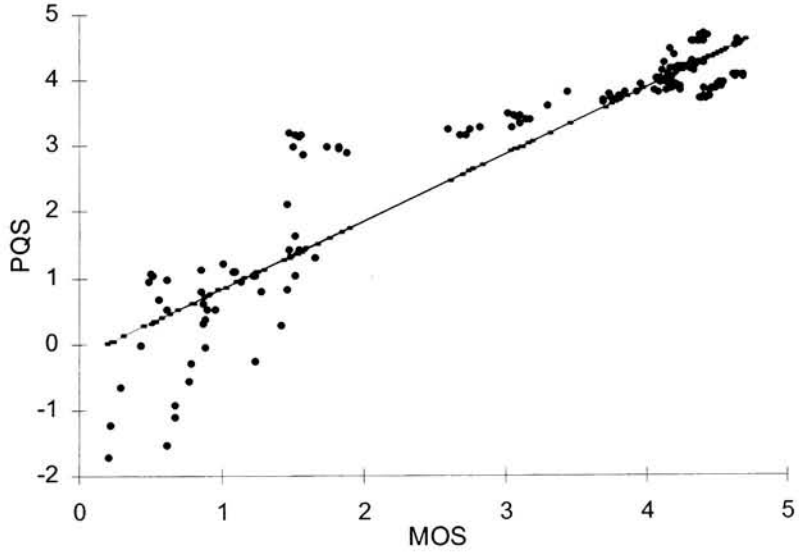

Figure 4-33. *PQS versus MOS*

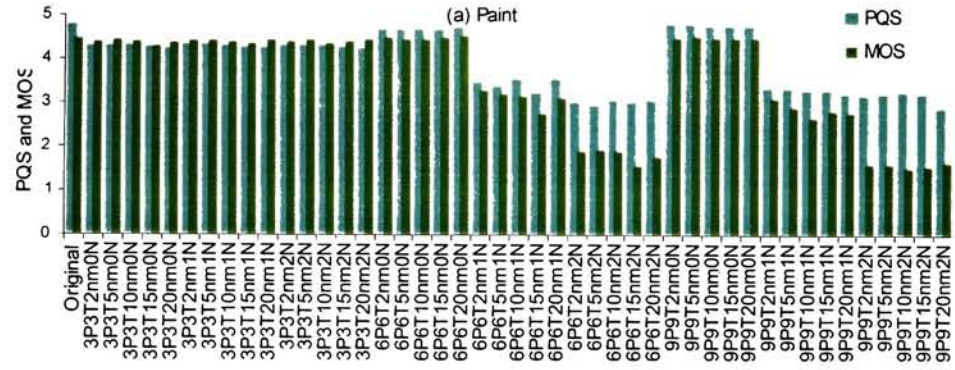
(a) Paint
PQS
MOS
PQS and MOS
0
1
2
3
4
5
Original
3P3T2nm0N
3P3T5nm0N
3P3T10nm0N
3P3T15nm0N
3P3T20nm0N
3P3T2nm1N
3P3T5nm1N
3P3T10nm1N
3P3T15nm1N
3P3T20nm1N
3P3T2nm2N
3P3T5nm2N
3P3T10nm2N
3P3T15nm2N
3P3T20nm2N
6P6T2nm0N
6P6T5nm0N
6P6T10nm0N
6P6T15nm0N
6P6T20nm0N
6P6T2nm1N
6P6T5nm1N
6P6T10nm1N
6P6T15nm1N
6P6T20nm1N
6P6T2nm2N
6P6T5nm2N
6P6T10nm2N
6P6T15nm2N
6P6T20nm2N
9P9T2nm0N
9P9T5nm0N
9P9T10nm0N
9P9T15nm0N
9P9T20nm0N
9P9T2nm1N
9P9T5nm1N
9P9T10nm1N
9P9T15nm1N
9P9T20nm1N
9P9T2nm2N
9P9T5nm2N
9P9T10nm2N
9P9T15nm2N
9P9T20nm2N

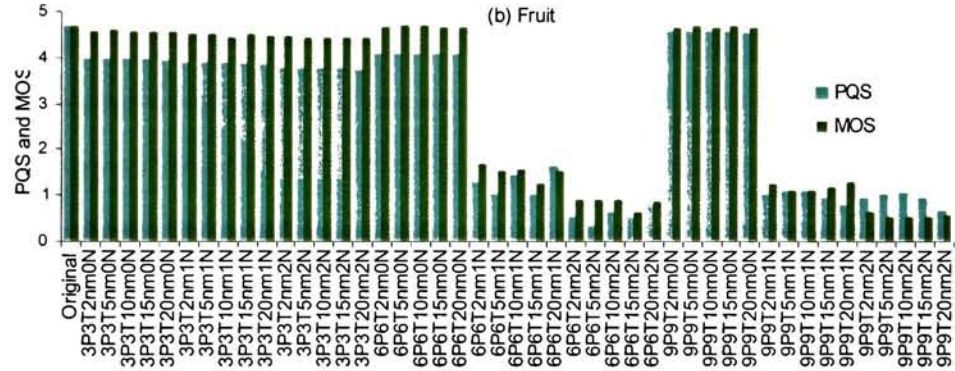
(b) Fruit
PQS
MOS
PQS and MOS
0
1
2
3
4
5
Original
3P3T2nm0N
3P3T5nm0N
3P3T10nm0N
3P3T15nm0N
3P3T20nm0N
3P3T2nm1N
3P3T5nm1N
3P3T10nm1N
3P3T15nm1N
3P3T20nm1N
3P3T2nm2N
3P3T5nm2N
3P3T10nm2N
3P3T15nm2N
3P3T20nm2N
6P6T2nm0N
6P6T5nm0N
6P6T10nm0N
6P6T15nm0N
6P6T20nm0N
6P6T2nm1N
6P6T5nm1N
6P6T10nm1N
6P6T15nm1N
6P6T20nm1N
6P6T2nm2N
6P6T5nm2N
6P6T10nm2N
6P6T15nm2N
6P6T20nm2N
9P9T2nm0N
9P9T5nm0N
9P9T10nm0N
9P9T15nm0N
9P9T20nm0N
9P9T2nm1N
9P9T5nm1N
9P9T10nm1N
9P9T15nm1N
9P9T20nm1N
9P9T2nm2N
9P9T5nm2N
9P9T10nm2N
9P9T15nm2N
9P9T20nm2N

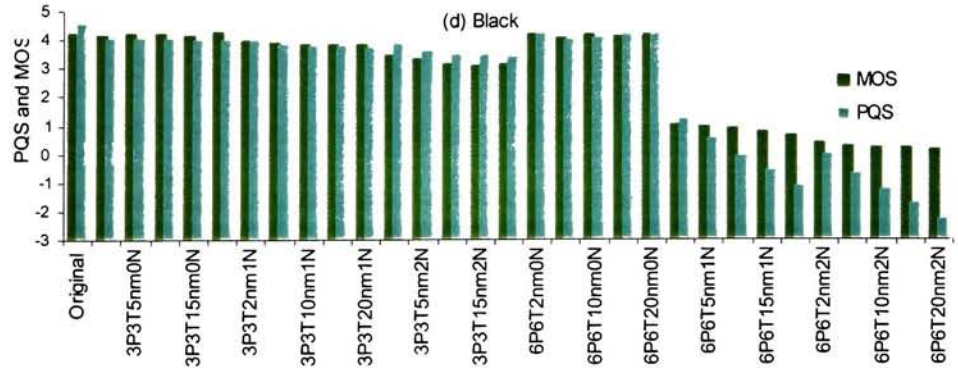
(d) Black
MOS
PQS
PQS and MOS
-3
-2
-1
0
1
2
3
4
5
Original
3P3T5nm0N
3P3T15nm0N
3P3T2nm1N
3P3T10nm1N
3P3T20nm1N
3P3T5nm2N
3P3T15nm2N
6P6T2nm0N
6P6T10nm0N
6P6T20nm0N
6P6T5nm1N
6P6T15nm1N
6P6T2nm2N
6P6T10nm2N
6P6T20nm2N

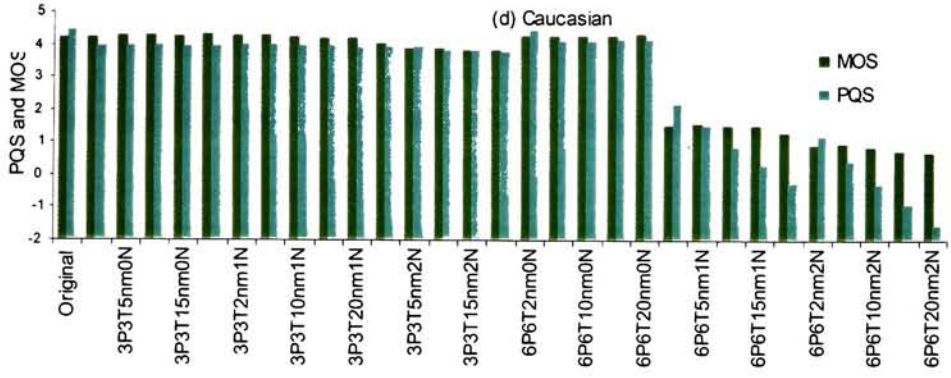

Figure 4-34*. PQS and MOS values for test images.*

The relationship between PQS and MOS is plotted in Fig. 4-33. It shows that there is relatively large errors in extreme low image quality range; some PQS values are negative. It also suggests that a further regression fit, such as quadratic equation fit, may provide a better prediction for overall image quality.

The PQS values for each test images are plotted in Fig. 4-34 for four image sets. For comparison, MOS values are also plotted together. Compared PQS to MOS, the mean absolute error was 0.45 with the maximum of 2.5 occurred at 6P6T20nm2N of Caucasian image. Given that the subjective image quality scores of the test images had at most precision of 0.5, an average absolute error of 0.45 seems adequate. However, the maximum error of 2.5 was far beyond the tolerance. It was found that most of the large absolute errors (absolute error > 1.0) occurred at using 6 and more than 6 channels with noise and large wavelength steps (especially 15nm and 20 nm steps) for painting, Caucasian and Black image sets. However, PQS predicted very well for fruit image sets in the similar situation. The reason is unknown at this stage. We also found that the large

percentage errors occurred for the extreme low end of the image quality range, which may suggest the limitation of application using PQS for extreme low image quality range.

The PQS above was obtained from the principal components, initially. An alternative way was to compute the PQS directly from the distortion factors. To avoid any confusion, the PQS here will be expressed PQS_d. The procedure is given as following. First, let the PQS_d be the linear combination of the distortion factors using equation as given in Eq. 4-36.

$$PQS_d = \sum_{i=1}^{4} c_i \cdot F_i , \qquad (4-36)$$

where c_i are the coefficients that need to be determined using least square regression based on MOS values. The results are given in Eq. 4-37 where the correlation between PQS_d and MOS was 0.9565.

$$PQS_d = -0.1350 \cdot F_1 - 0.0482 \cdot F_2 + 0.0364 \cdot F_3 + 0.00029 \cdot F_4 . \qquad (4-37)$$

The next step was based on Eq. 4-38 as given below

$$PQS_d = d_0 + \sum_{i=1}^{4} d_i \cdot F_i , \qquad (4-38)$$

where d_0 and d_i are the coefficients that need to be determined by minimizing the RMS differences between PQS_d and MOS. The initial value for d_0 was zero and d_i were assigned the c_i values given in Eq. 4-37. The reason to play two steps with Eqs. 4-36 and 4-38 was the same as that in Eqs. 4-29 and 4-31 to avoid the local minimum in MRA if performing Eq. 4-38 directly. The final PQS_d is given in Eq. 4-39. The correlation coefficients between the final PQS_d and MOS was 0.9628. Compared to the correlation value of 0.9226 when using principal components method, conventional PQS_d method,[44,

[78] the PQS_d calculated directly from the distortion factors using Eqs. 4-37 and 4-38 got a better result.

$$PQS_d = 7.0839 - 0.1354 \cdot F_1 - 0.1202 \cdot F_2 - 0.0237 \cdot F_3 + 0.0188 \cdot F_4. \qquad (4-39)$$

The relationship between this new PQS_d and MOS is plotted in Fig. 4-35. It shows that PQS_d did not predict MOS well in the extreme low image quality range; some PQS_d are negative. The graph also shows that a further regression fit, such as a quadratic equation fit, may provide a better quality prediction.

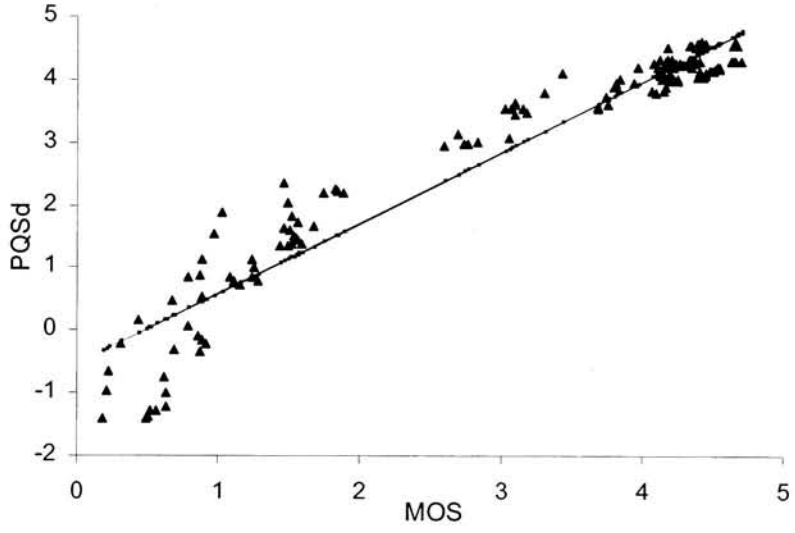

Figure 4-35. *PQS_d versus MOS.*

The PQS_d values are plotted in Fig. 4-36 for all four image sets. For comparison, MOS values are also plotted together. Compared PQS to MOS, the mean absolute error was 0.35 with the maximum of 1.89 occurred at 9P9T15nm2N of fruit image. It is clear that PQS_d was a better quality metric compared to PQS calculated from the principal components. The maximum error of 1.89 occurred at extreme low end of the image quality range. It was also found that most of the large errors occurred at the extreme low

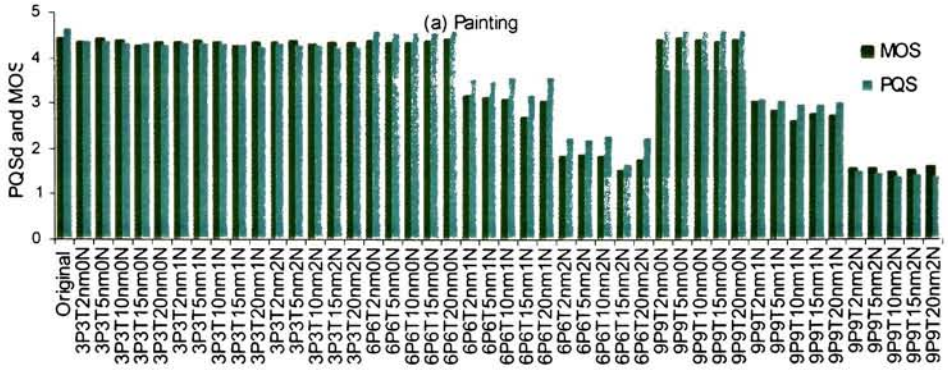
(a) Painting
PQSd and MOS
MOS
PQS
Original
3P3T2nm0N
3P3T5nm0N
3P3T10nm0N
3P3T15nm0N
3P3T20nm0N
3P3T2nm1N
3P3T5nm1N
3P3T10nm1N
3P3T15nm1N
3P3T20nm1N
3P3T2nm2N
3P3T5nm2N
3P3T10nm2N
3P3T15nm2N
3P3T20nm2N
6P6T2nm0N
6P6T5nm0N
6P6T10nm0N
6P6T15nm0N
6P6T20nm0N
6P6T2nm1N
6P6T5nm1N
6P6T10nm1N
6P6T15nm1N
6P6T20nm1N
6P6T2nm2N
6P6T5nm2N
6P6T10nm2N
6P6T15nm2N
6P6T20nm2N
9P9T2nm0N
9P9T5nm0N
9P9T10nm0N
9P9T15nm0N
9P9T20nm0N
9P9T2nm1N
9P9T5nm1N
9P9T10nm1N
9P9T15nm1N
9P9T20nm1N
9P9T2nm2N
9P9T5nm2N
9P9T10nm2N
9P9T15nm2N
9P9T20nm2N

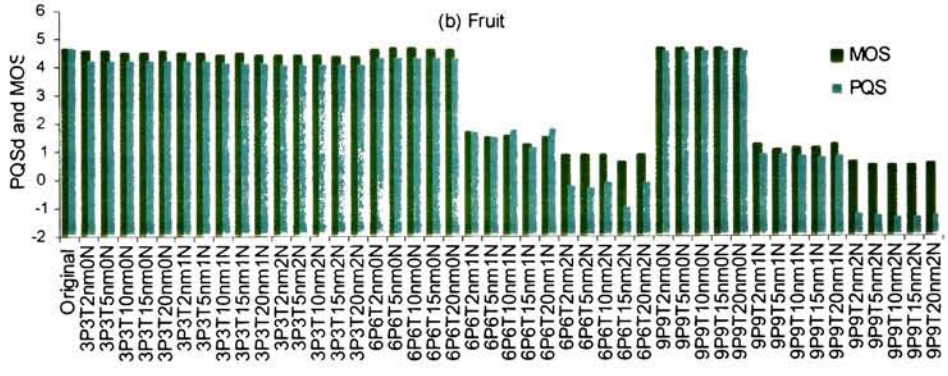
(b) Fruit
PQSd and MOS
MOS
PQS
Original
3P3T2nm0N
3P3T5nm0N
3P3T10nm0N
3P3T15nm0N
3P3T20nm0N
3P3T2nm1N
3P3T5nm1N
3P3T10nm1N
3P3T15nm1N
3P3T20nm1N
3P3T2nm2N
3P3T5nm2N
3P3T10nm2N
3P3T15nm2N
3P3T20nm2N
6P6T2nm0N
6P6T5nm0N
6P6T10nm0N
6P6T15nm0N
6P6T20nm0N
6P6T2nm1N
6P6T5nm1N
6P6T10nm1N
6P6T15nm1N
6P6T20nm1N
6P6T2nm2N
6P6T5nm2N
6P6T10nm2N
6P6T15nm2N
6P6T20nm2N
9P9T2nm0N
9P9T5nm0N
9P9T10nm0N
9P9T15nm0N
9P9T20nm0N
9P9T2nm1N
9P9T5nm1N
9P9T10nm1N
9P9T15nm1N
9P9T20nm1N
9P9T2nm2N
9P9T5nm2N
9P9T10nm2N
9P9T15nm2N
9P9T20nm2N

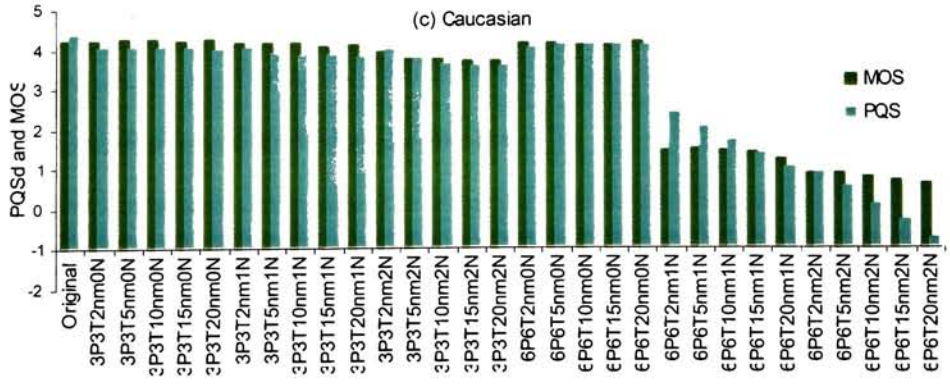
(c) Caucasian
PQSd and MOS
MOS
PQS
Original
3P3T2nm0N
3P3T5nm0N
3P3T10nm0N
3P3T15nm0N
3P3T20nm0N
3P3T2nm1N
3P3T5nm1N
3P3T10nm1N
3P3T15nm1N
3P3T20nm1N
3P3T2nm2N
3P3T5nm2N
3P3T10nm2N
3P3T15nm2N
3P3T20nm2N
6P6T2nm0N
6P6T5nm0N
6P6T10nm0N
6P6T15nm0N
6P6T20nm0N
6P6T2nm1N
6P6T5nm1N
6P6T10nm1N
6P6T15nm1N
6P6T20nm1N
6P6T2nm2N
6P6T5nm2N
6P6T10nm2N
6P6T15nm2N
6P6T20nm2N

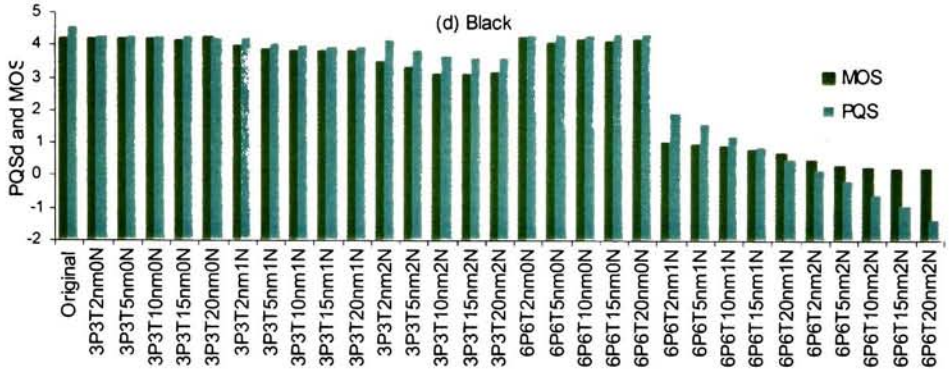

Figure 4-36. *PQS_d and MOS values for test images.*

end of image quality range with large wavelength steps and noise, and using more channels. This may suggest the limitation of application using PQS_d for extreme low quality range.

Mathematically, PQS_d could be improved further by playing one order linear regression for whole PQS_d to MOS. The result could then be defined as the new PQS_d. The mean absolute error would drop to 0.35 with the maximum of 1.34 occurred at the same test image as that for the original PQS_d. The result of regression is given in Eq. 4-40.

$$PQS_{dnew} = 0.6675 + 0.8235 \cdot PQS_d \qquad (4-40)$$

4.4.6.3 Contribution of the Distortion Factors

We now evaluate more detail about the importance of the distortion factors, taken singly and in different combinations. For all sets of combinations of distortion factors, the procedures of PCA and applications using Eqs. 4-29 to 4-39 were performed. The correlation coefficients and the mean absolute errors of the predictions from PQSs and PQS_ds are given in Table 4- 40. The results in Table 4-40 indicate that, using three

Table 4-40. *Correlation coefficients between PQS and MOS, and PQS_d and MOS.*

	PQS		PQSd	
Factors	R	mean |error|	R	mean |error|
1	0.9623*	0.35	0.9623*	0.35
2	0.8803	0.59	0.8803	0.59
3	0.1493	1.33	0.1493	1.33
4	0.1698	1.37	0.1698	1.37
1 2	0.9211*	0.45	0.9591	0.37
1 3	0.8815	0.57	0.9630	0.35
1 4	0.8169	0.80	0.9631*	0.34
2 3	0.6222	0.99	0.8821	0.57
2 4	0.5642	1.13	0.8918	0.52
3 4	0.3139	1.29	0.3792	1.20
1 2 3	0.9228	0.44	0.9589	0.37
1 2 4	0.9232*	0.45	0.9600	0.35
1 3 4	0.8884	0.56	0.9666*	0.33
2 3 4	0.6363	1.05	0.8928	0.50
1 2 3 4	0.9225	0.45	0.9628	0.35

distortion factors, the combination of color difference, graininess and contrast would provide the best prediction for image quality when applying PCA method. However, when playing regression directly to the distortion factors, combination of color difference, sharpness and contrast factors would obtain the best results. Since the PCA method considered the coverage of all data space of participated factors, the results obtained from PCA method may have more feasibility for common application in other situations. On the other hand, PQS_d was calculated directly from MRA based on distortion factors that it did not consider the dimensions of the data space. Therefore, PQS_d may have limits to common application though it might have better results for specific data sets in this research from regression. Thus, we will concentrate on PQS while using PQS_d as a comparison in our discussion. Back to the combinations of three distortion factors, the best combination would be color difference, graininess and contrast factors. The

combinations of color difference, graininess and sharpness would also predict the image quality almost equally well. It is safe to say that the combination without color difference factor would not predict the image quality well, either using PQS or PQS_d. When using two distortion factors, the combination of color difference and graininess would be the best choice while the combination of color difference and sharpness could be a good candidate. The low correlation of MOS and PQS using the combination of color difference and contrast factors, on the other hand, proved that the PCA approach considered the space coverage of the factors involved, not just the fit for the best prediction as the PQS_d's. The PQS_d could keep the color difference factor and remove the impact of other factors to reach the best fit. For single distortion factor, the color difference was the most important factor to predict the color image quality. The correlation coefficient of 0.9623 between MOS and the PQS based only on color difference shows the color difference itself could be a very good image quality metric. This was also the reason why PQS_d could predict the image quality well when color difference factor was involved in any combinations of distortion factors.

4.4.6.4 Limitations of PQS Applications

The distortion factors applied in this research spanned three dimensions. Based on MRA statistical regression techniques, PQS could be reduced to one dimension factor which had a good correlation with image quality MOS. In the statistical regression, the contributions of the distortion factors could be positive or negative. If these contributions were outside the range of which the regression was carried out, the results of PQS may be invalid such as the situation for extreme low quality range. Thus, a meaningful PQS

required meaningful contributions from the distortion factors. As suggested by Miyahara,[44] for the PQS to be meaningful, one requirement is that the weighted contribution of each of the factors as given in Eq. 4-35 be in the range of one to five. The performance of PQS could be improved by performing the piecewise steps to get the best PQS for each range of the image quality.

4.4.6.5 Empirical Image Quality Metric

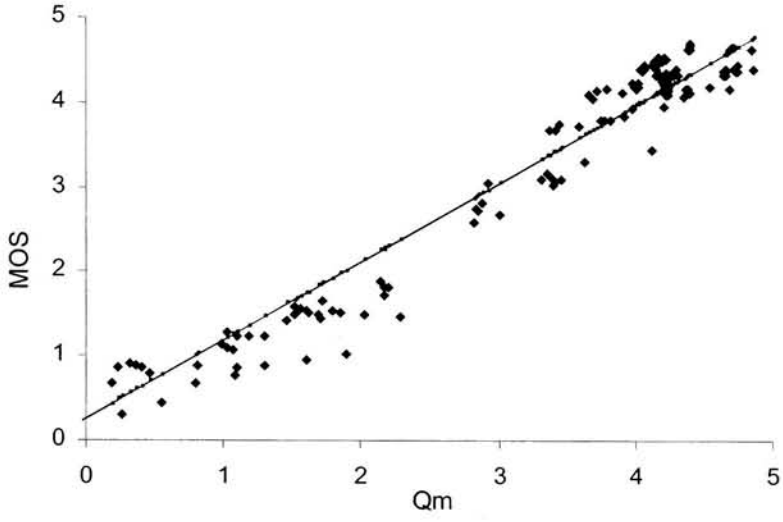

Figure 4-37. *MOS vs. Qm*

Mathematically, we could also perform the MRA for distortion factors without considering the their statistical characteristics to obtain an empirical image quality metric which had very high correlation to MOS. A multiple regression analysis (MRA) was carried out between MOS values and distortion factors to determine one single image quality metric. The result is given in Eq. 4-41, where Qm is the empirical quality metric. The correlation coefficient between MOS and Qm is 0.9770. The mean absolute error is as low as 0.24. Fig. 4.37 shows the relationship between MOS and Qm. Fig 4.37 suggests

that there is still some improvement space in future study; further fit procedure might be necessary to provide a better image quality prediction.

$$Qm = 6.141 - 0.174 \cdot F_1^{0.872} - 0.447 \cdot F_2^{0.515} - 0.008 \cdot F_3^{1.164} + 0.206 \cdot F_4.^{0.439} \quad (4-41)$$

4.5 Summary

An image quality investigation in visible spectral imaging was performed. Spectral images were simulated using different number of imaging channels, wavelength steps, and noise levels based on two practical spectral imaging systems. A mean opinion score (MOS) was determined from, rendered to a three-channel LCD display, subjective visual assessment scale experiment for image quality of spectral images. A set of partial image distortion measures, color difference for color images, graininess, sharpness and contrast, were defined based on possible classified and quantified actual distortions produced by spectral imaging systems. The MOS and distortion measures were highly correlated. The results indicate that the image quality of spectral imaging system was significantly affected by the number of channels used with noise in the image capture stage. The selection of wavelength steps plays no significant effect on final image quality if noise is not involved. However, if noise is involved, the using of large wavelength increments, such as 15nm and 20nm increments, will significantly impact the image quality of spectral images. The results also showed that the contrast factor plays different effect on image quality for human portraits compared to that on other complex-scene images. Principal components analysis was then carried out to quantify the correlation between distortion factors. A multiple regression analysis (MRA) was carried out between the

principal component vectors and the measured MOS values to determine the picture quality scale (PQS). The obtained quality metric, PQS, has a good correlation to the subjective measure, MOS, with the correlation coefficient of 0.9225 and mean absolute error of 0.45. Statistical analysis further indicated that the single color difference factor itself could be a very good image quality metric. It also showed the combinations of color difference, graininess and either sharpness or contrast will be the best choice when using three factors to predict the image quality. When using two distortion factors, the combination of color difference and graininess would be the best choice. For better prediction of the visual image quality experiment data, an alternative method is to perform the MRA directly using distortion factors to obtain PQS_d. When using all four factors, the correlation between PQS_d and MOS can be achieved as high as 0.9628 with mean absolute error of 0.35. Finally, an empirical model of image quality metric was also provided, independent of the scene contents. The correlation between MOS and the empirical image metric was 0.9770. Those results showed that our visual image quality experiment for spectral imaging system was successful though some improvement needed to be performed in future research. To improve the prediction of PQS and PQS_d, further regression fit can be also performed.

5. CONTRIBUTIONS TO LIPPMANN2000

This research contributed to spectral imaging data base, Lippmann2000, in several aspects. First, this research contributed a relatively complete spectral reflectance data base measured from human face with different races and from different face parts. Those spectral reflectances would provide the first hand data for researchers around the world in spectral imaging research, color and spectral reproduction for human face. This research also contributed some spectral images of human face. Second, this research contributed technique reports in the spectral imaging system for human portraits and image quality analysis in spectral imaging system. It provided a thorough statistical analysis for spectral characteristics of human face spectra. This provides practical suggestions for researchers in spectral imaging system design for human portraits. The reports in image quality analysis would help in researchers not only in spectral imaging system design, but also other image quality applications and analysis for color systems as well. The web site of Lippmann200 is http://www.cis.rit.edu/mcsl/online/lippmann2000.shtml.

6 CONCLUSIONS

The purpose of this research was to design a spectral imaging system for human portraits, quantify properties and create meaningful image-quality metrics for spectral images. The experiment results showed that this research is successful. The conclusions will be provided separately in terms of spectral imaging and image quality.

6.1 Conclusions in Spectral Imaging for Human Portraits

This research proposed a new procedure for capturing spectral image of human portraiture. A spectral imaging system based on this procedure was designed and the spectral imaging experiment was performed. The facial spectral reflectances obtained were analyzed by PCA method. The PCA results indicated that three basis functions based on all races will provide accurate enough color and spectral reproduction for facial spectral reflectances from various races and different face parts. Three-band and six-band, visible range, spectral images of human portraits had been successfully obtained. High order transform matrices would provide more accurate, three-band, spectral images with acceptable image noise. However, for six-band spectral images, a transformation matrix with low order of 7 terms would give most acceptable results. Due to the limit of image quality of the camera used, the 6-band spectral images did not meet the quality the author originally expected. To obtain more accurate, multi-spectral image, it was suggested that a camera with high quality in terms of noise is required. The obtained spectral image can be applied to color-imaging system design and analysis.

6.2 Conclusions of Image Quality of Spectral Imaging System

Image quality research for spectral imaging systems was performed. Spectral images were simulated using different number of basis functions, wavelength steps, and noise levels based on two practical spectral imaging systems, SONY DKC-ST5 digital camera in spectral imaging for human face and IBM Research Pro\3000 digital camera in spectral imaging for complex scenes. A visual assessment experiment for image quality was designed and successfully performed. Mean opinion score (MOS) was obtained from this subjective visual assessment scale experiment for image quality of spectral images. A set of partial image distortion measures, color difference for color images, graininess, sharpness and contrast, was defined based on classified and quantified actual distortions produced by spectral imaging systems. The MOS and distortion measures were highly correlated. The MOS results indicated that the image quality of spectral imaging system was significantly affected by the number of channels used with noise in the image capture stage. The selection of wavelength steps played no significant impact on final spectral image quality within the limit in this research. The results also showed that the contrast factor played different impact on spectral image quality for human portraits compared to that on spectral images of complex-scene. Principal components analysis indicated that these four distortion factors spanned three-dimensions. Image quality metric, PQS, was determined based on principal component vectors and MRA fitting to MOS. The obtained quality metric, PQS, as a function of distortion factors, was highly correlated with the subjective measure, MOS. A modified PQS was also obtained based on playing MRA directly using distortion factors. The importance of contributions in image quality

prediction from distortion factors was analyzed. The results showed that a single color difference factor itself could be a very good image quality metric. Finally, an empirical model of image quality was also provided. Those results showed that our visual image quality experiment for spectral imaging system was successful though some improvement needed to be performed in future research.

6.3 Scientific Contributions

The scientific contributions of this thesis research can be summarized as followings:

- Design of a spectral imaging system for human portraits using a new approach that calibrating the imaging system and capturing the spectral imaging simultaneously. Spectral images of human portraits were obtained within the limit of imaging system.
- Complete statistical analysis for spectral characteristics of the spectral reflectances in human face from various races and face parts. Finding the basis spectral functions of spectra of human face with more reliable range that can be applied in spectral imaging for human portraits from various races and face parts.
- Creation of some specific simulation methods for simulating spectral images based on real spectral imaging systems.
- Proposed the application of PQS method in color image quality research for spectral imaging system. Defined distortion factors that describing the impairment of the spectral images from spectral imaging systems.

- Quantifying properties and creating meaningful objective image quality metrics for spectral images. The objective quality metrics were highly correlated to the subjective results. Statistical analysis for the importance of contributions from those distortion factors in predicting image quality.
- The approach of image quality analysis in this research can also provide practical suggestions for other color image quality study.

6.4 Future Work

There are several topics that can be considered in future research. One is the optimization of the spectral imaging system for human portraits. This includes the optimization of the spectral sensitivities of the digital camera system and optimization in selection of external filters for more than over 3 channel applications. Another topic is optimizing the selection of printer inks in spectral image reproduction for human portraits. This can be achieved by applying the basis functions obtained in this research to ink selection. An interesting topic can be the research in the image preference of spectral image using different illuminants and different illuminant geometries. It can also apply the basis functions obtained in this research for illuminant estimation and pattern recognition. Future research should also be performed in the image quality analysis. One challenging topic is to define some image distortion factors with exactly the visual perception meanings and can cover all image quality issues and be valid for wide image applications. The image quality metrics obtained from this research also need to be

evaluated in other image quality experiments, either the quality metrics themselves or the procedures in analysis.

REFERENCES

1. G. M. Johson and M. D. Fairchild, Full-spectral Color Calculations in Realistic Image Synthesis, *IEEE Computer Graphics and Applications*, **19**, 4, 47-53 (1999).

2. R. S. Berns, Change for Color Science in Multimedia Imaging, in Colour Imaging: Vision and Technology, edited by L. MacDonald and M. R. Luo, John Wiley & Sons, Chichester, 99-127 (1998).

3. P. D. Burns and R. S. Berns, Analysis of Multispectral Image Capture: in *Proc. IS&T/SID Fourth Color Imaging Conference: Color Science, Systems and Applications*, IS&T, Springfield, VA, USA, 19-22 (1996).

4. F. H. Imai and R. S. Berns, High-resolution Multi-spectral Image Archives – A Hybrid Approach, in *Proc. IS&T/SID Sixth Color Imaging Conference: Color Science, Systems and Applications*, IS&T, Springfield, 224-227 (1998).

5. R. S. Berns, F. H. Imai, P. D. Burns and Di-Y, Tzeng, Multi-spectral-based Color Reproduction Research at the Munsell Color Science Laboratory, in *Proc. of SPIE,* **3409**, SPIE, Bellingham, WA, USA, 14-25 (1998).

6. F. H. Imai and R. S. Berns, Spectral Estimation Using Trichromatic Digital Cameras, in *Proc. of the International Symposium on Multispectral Imaging and Color Reproduction for Digital Archives*, Chiba, Japan, 42-49 (1999).

7. F. H. Imai, Multi-spectral Image Acquisition and Spectral Reconstruction using a Trichromatic Digital Camera System Associated with Absorption Filters, Munsell Color Science Laboratory Technical Report, http://www.cis.rit.edu/research/mcsl/pubs/PDFs/CameraReport.pdf (1998).

8. F. H. Imai, N. Tsumura, H. Haneishi and Y. Miyake, Principal Component Analysis of Skin Color and Its Application to Colorimetric Color Reproduction on CRT Display and Hardcopy, *J. of Imaging Sci. Technol.* **40**, 5, 422-430 (1996).

9. P. D. Burns, Analysis of Image Noise in Multi-Spectral Color Acquisition, Ph.D. Thesis, Rochester Institute of Technology (1997).

10. P. D. Burns and R. S. Berns, Error Propagation in Color Signal Transformations, *Color Res. Appl.* **22**, 280-289 (1997).

11. B. Hill, Optimization of Total Multispectral Imaging Systems: Best Spectral Match versus least Observer Metamerism, in *9th Congress of the International Colour Association*, Proc. of SPIE Vol. **4421**, 481-486 (2001).

12. Shoji Tominaga, Spectral Imaging by a Multi-Channel Camera, *IS&T/SPIE Conference on Color Imaging: Device-Independent Color, Color Hardcopy and Graphic Arts IV*, San Jose, California, 38-47 (1999).

13. L. A. Brunsting and C. Sheard, The Color of the Skin as Analyzed by Spectr0photometric Method. II. The Role of Pigmentation, *J. of Clinical Investigation*, **7**, 575-592 (1929).

14. L. A. Brunsting and C. Sheard, The Color of the Skin as Analyzed by Spectrophotometric Method. III. The Role of Superficial Blood, *The J. of Clinical Investigation*, **7**, 593-613 (1929).

15. R. C. Cohen, The Color of Man, Rondom House, Inc., New York (1968).

16. E. A. Edwards and S. Q. Duntley, The Pigments and Color of Living Human Skin, *The Amer. J. of Anatomy*, **65**, 1, 1-33 (1939).

17. N. Kollias and A. Baqer, Spectroscopic Characteristics of Human Melanin in Vivo, *J. of Investigative Dermatology*, **85**, 1, 38-42 (1985).

18. W. R. Buck and F. Grum, Reflection Spectrophotometry, *Archives of Dermatology*, **83**, 111-123 (1961).

19. G. B. Buck and H. C. Froelich, Color Characteristics of Human Complexions, *Illuminating Engineering*, **43**, 1, 27-49 (1948).

20. E. Angelopoulou, The Reflectance Spectrum of Human Skin, *Technical Report MS-CIS-99-29*, http://www.cis.upenn.edu/~elli/tech-report.skin.pdf, 1-14 (1999).

21. M. J. C. Van Gemert, S. L. Jacques, H. J. C. M. Sterenborg and W. M. Star, Skin Optics, *IEEE Transactions on Biomedical Engineering*, **36**, 12, 1146-1154 (1989).

22. F. H. Imai, N. Tsumura, H. Haneishi and Y. Miyake, Principal Component Analysis of Skin Color and Its Application to Colorimetric Color Reproduction on CRT Display and Hardcopy, *J. of Imaging Sci. Technol.* **40**, 5, 422-430 (1996).

23. N. Ojima, H. Haneishi, and Y. Miyake, The appearance of Skin with Make-up(III)[Estimation for Spectral Reflectance of Skin with the HDTV Color Image], *J. SPSTJ*, **57**, 78-83 (1994).

24. Shoji Tominaga, Spectral Imaging by a Multi-Channel Camera, *IS&T/SPIE Conference on Color Imaging: Device-Independent Color, Color Hardcopy and Graphic Arts IV,* San Jose, California, 38-47 (1999).

25. Di-Yuan Tzeng, Spectral-Based Color Separation Algorithm Development for Multiple-Ink Color Reproduction, Ph.D. thesis, Rochester Institute of Technology (1999).

26. S. Tominaga, Multi-Channel Cameras and Spectral Image Processing, *Proc. of the International Symposium on Multispectral Imaging and Color Reproduction for Digital Archives*, Chiba, Japan, 18-25 (1999).

27. R. A. Johnson, Applied Multivariate Statistical Analysis, 3rd Ed., Englewood Cliffs, N.J., Prentice Hall (1992).

28. A. C. Rencher, Method of Multivariate Analysis, New York, Wiley (1995).

29. P. D. Burns and R. S. Berns, Image Noise and Colorimetric Precision in Multispectral Image Capture, http://www.cis.rit.edu/people/faculty/berns/PDFs/cic6_Burns.pdf (1998).

30. E. A. Day, R. S. Berns, L. Taplin and F. Imai, A Psychophysical Experiment Evaluating the Color Accuracy of Several Multispectral Images Capture Techniques, *Proc. IS&T PICS Conference*, IS&T, Springfield, VA, USA, 199-204 (2003).

31. S. Quan, et al, Optimal Design of Camera Spectral Sensitivity Functions Based on Practical Filter Components, *Proc. IS&T/SID Ninth Color Imaging Conference: Color Science and Engineering, Systems, Technologies and Applications*, IS&T, Springfield, VA, USA, 326-331 (2001).

32. F. H. Imai, M. R. Rosen and R. S. Berns, Comparative study of metrics for spectral match quality, *Proc. First European Conference on Color in Graphics, CGIV'2002*, Imaging and Vision, IS&T, Springfield, VA, 2002, 492-496 (2002).

33. B. Hill, Optimization of Total Multispectral Imaging Systems: Best Spectral Match versus lease Observer Metamerism, in *9th Congress of the International Colour Association*, Proc. of SPIE Vol. **4421**, 481-486 (2001).

34. P. G. Engeldrum, Image Quality Modeling: Where Are We?, *Proc. IS&T PICS Conference*, IS&T, Springfield, VA, USA, 251-255 (1999).

35. N. Avadhanam and V. R. Algazi, Prediction and Measurement of High Quality in Still Image Coding, *Very High Resolution and Quality Imaging*, SPIE Proc, **2663**, 100-109 (1996).

36. A. M. Eskicioglu and P. S. Fish, Image Quality Measures and Their Performance, *IEEE Transactions on Communications*, **43**, 12, 2959-2965 (1995).

37. Jean-Luc Olives, B. Lamiscarre and M. Gazalet, Optimization of Electro-Optical Imaging System with an Image Quality Measure, *Very High Resolution and Quality Imaging*, SPIE Proc, **3025**, 158-167 (1997).

38. J. A. S. Viggiano, A Perception-Referenced Method for Comparison of Radiance Ratio Spectra and its Application as an Index of Metamerism." in *9th Congress of the International Colour Association*, Proc. of SPIE Vol. **4421**, 701-705 (2001).

39. K. Natale-Hoffman, E. Dalal, R. Rasmussen and M. Sato, Effect of Selected Image Quality Attributes on Overall Preference, *Proc. IS&T PICS Conference*, IS&T, Springfield, VA, USA, 266-269 (1999).

40. H. Koroaki, Quality Measure of Color Scanning Filters, *Proc. IS&T/SID Second Color Imaging Conference: Color Science, Systems and Applications*, IS&T, Springfield, VA, USA, 58-61 (1994).

41. R. Alter-Gartenberg and S. K. Park, Information as a Quality Metric for High-Resolution Imaging, *Very High Resolution and Quality Imaging*, SPIE Proc, **3308**, 16-27 (1998).

42. Y. Horita, Y. Inazumi and K. Kotani, Quality Estimation Model of Monochrome Still Picture Based on Distortion Factors and Texture Features, *IS&T's 1999 PICS Conference*, IS&T, Springfield, VA, USA, 419-424 (1999).

43. K. Miyata, M. Baba, N. Tsumura, H. Haneishi and Yoichi Miyake, Improvement of Sharpness and Graininess for Color Image by Computer Processing and Its Image Quality Measurement, *IS&T's 1999 PICS Conference*, IS&T, Springfield, VA, USA, pp.236-240 (1999).

44. M. Miyahara, K. Kotani and V. R. Algazi, Objective Picture Quality Scale (PQS) for Image Coding, *IEEE Transactions on Communications*, **46**, 9, 1215-1226 (1998).

45. P. D. Burns and R. S. Berns, Image Noise and Colorimetric Precision in Multispectral Image Capture, http://www.cis.rit.edu/people/faculty/berns/PDFs/cic6_Burns.pdf (1998).

46. P. D. Burns and R. S. Berns, Quantization in Multispectral Color Image Acquisition, *Proc. IS&T/SID Seventh Color Imaging Conference: Color Science, Systems, and Applications,* IS&T, Springfield, VA, USA, 32-35 (1999).

47. M. D. Fairchild, *Color Appearance Models*, Addison Wesley Longman, Inc. (1998).

48. M. R. Luo, G. Cui and B. Rigg, The Development of the CIE 2000 Color Difference FormulA, *Color Res. Appl.* **26**, 340-350 (2001).

49. M.D. Fairchild, "Revision of CIECAM97s for Practical Applications," *Color Res. Appl.* **26**, 418-427 (2001).

50. G. M. Johnson and M. D. Fairchild, A Top Down Description of S-CIELAB and CIEDE2000, *Color Res. Appl.* in press. (2003).

51. X. M. Zhang and B. A. Wandell, A Spatial Extension to CIELAB for Digital Color Image Reproduction, *Societ of Information Display Symposium Technical Digest*, **27**, 731-734.(1996).

52. A. B. Poirson and B. A. Vandell, Appearance of colored patterns: Pattern-color separability, *J. Opt. Soc. Am*, **10**, 12, 2458-2470 (1993).

53. T. Movshon and L. Kiorpes,, Analysis of the Development of Spatial Sensitivity in Monkey and Human Infants, J. Opt. Soc. Am., 5, 2166-2172.(1988).

54. J. C. Dainty and R. Shaw, Image Science, Academic Press, INC. New York (1988).

55. P. J. Barten, The SQRI Method: A New Method for the Evaluation of Visible Resolution on a Display, *Proc. Of the SID*, **28**, 3, 253-261. (1987).

56. P. J. Barten, the Effects of Picture Size and Definition on Perceived Image Quality, *IEEE Tran. On Elec.* Dev., **36**, 9, 1865-1869 (1989).

57. P. J. Barten, Evaluation of Subject Image Quality with Square-root Integral Method, *J. Opt. Soc. Am. A*, **7**, 10, 2025-2031. (1990).

58. J. H. D. M. Westerink and J. A. Roufs, Subjective Image Quality as a Function of Viewing Distance, Resolution and Picture Size, *SMPTE J.* **98**, 113-119 (1989).

59. S. Bouzit and L. MacDonald, Colour Difference Metrics and Image Sharpness, *Proc. IS&T/SID Eighth Color Imaging Conference: Color Science and Engineering, Systems, Technologies, Applications*, IS&T, Springfield, VA, USA, 262-267 (2000).

60. A. J. Calabria and Mark D. Fairchild, Compare and Contrast: Perceived Contrast of Color Images, *Proc. IS&T/ SID Tenth Color Imaging Conference: Color Science and Engineering, Systems, Technologies, Applications* , IS&T, Springfield, VA, USA, 17-22 (2002).

61. http://www.cis.rit.edu/mcsl/online/lippmann2000.shtml.

62. F. H. Imai, Multi-spectral Image Acquisition and Spectral Reconstruction using a Trichromatic Digital Camera System Associated with Absorption Filters, *Munsell Color Science Laboratory Technical Report*(1998).

63. R. S. Berns, Billmeyer and Saltzman's Principles of Color Technology, 3rd Edition, John Wiley & Sons (2000).

64. Standards for the Classification of Federal Data on Race and Ethnicity, http://www.whitehouse.gov/omb/fedreg/race-ethnicity.html, Office of Management and Budget, The White House, USA, August (1995).

65. E. Marszalec, B. Martinkauppi, M. Soriano and M. Pietikinen , A physics-based face database for color research, *J. of Electronic Imaging*, **9**, 1, 32-38 (2000).

66. Minolta Spectrophotometer CM-2002, http://www.minoltaeurope.com/minolta/products/industrialmeters/colour/cm-2002.html.

67. IEC 61966-3, Color Measurement and Management in Multimedia System and Equipment, Part 2-1: Colour Management—Default RGB Colour Space—sRGB, *International Electrotechnical Commission,* Geneva, Switzerland (1999).

68. R. S. Berns, R. J. Motta, and M. E. Dorzynski, CRT Colorimetry, Part I: Theory and Practice, *Color Res. Appl.,* **18**, 288-314 (1993).

69. R. S. Berns, Methods for Characterizing CRT Displays, *Displays*, **16**, 173-182 (1996).

70. http://www.research.ibm.com/image-apps/p3000cm.html

71. F. F. Giordano, G. W. Braudaway, J. Christensen. J. Lee, and F. Mintzer, Evaluation of a High-quality digital system, *IS&T/SPIE International Symposium on Elctronic Imaging Science and Technology, Conference on Sensors, Cameras & Applications of Digital Photography*, in Proc. of SPIE **3650**, Bellingham, WA, 110-118 (1999).

72. F. H. Imai, Spectral Reproduction from Scene to Hardcopy, Part I: Multi-spectral Acquisition and Spectral Estimation using a Trichromatic Digital Camera System associated with absorption Filters, http://www.cis.rit.edu/mcsl/research/PDFs/Report.pdf (2000).

73. M. J. Vrhel, R. Gershon and L. S. Iwan, Measurement and Analysis of Object Reflectance Spectra, *Color Res. Appl.* **19**, 4-9 (1994).

74. How LCD Works, http://computer.howstuffworks.com/lcd.htm

75. M. D. Fairchild and D. R. Wyble, Colorimetric Characterization of the Apple Studio Display (Flat Panel LCD), Munsell Color Science Laboratory Technical Report (1998).

76. P. G. Barten, Resolution of Liquid-Crystal Display, *SID 91 DIGEST*, 772-775 (1991).

77. G. M. Johnson and M. D. Fairchild, Sharpness Rules, *Proc. IS&T/SID Eighth Color Imaging Conference: Color Science and Engineering, Systems, Technologies, Applications*, IS&T, Springfield, VA, USA, 24-30.(2000).

78. Y. Horita, Y. Inazumi, K. Kotani, T. Murai and V. R. Algazi, Quality Estimation Model of Monochrome Still Picture Based on Distortion Factors and Texture Features, *Proc. IS&T PICS Conference*, IS&T, Springfield, VA, USA, 419-424 (1999).

79. H. S. Fairman, Metameric, Correction Using Parameric Decomposition, *Color Res. Appl.*, **12**, pg. 261-265 (1987).

80. G. Wyszecki, Valenzmedtrische Undersuchung des Zusammenhanges zwischen normaler und anomaler Trichromasie, Psychophysical investigation of the relationship between normal and abnormal trichromatic vision), Farbe **2,** 39-52 (1953) (German).

81. K. M. Lam, Metamerism and Color Constancy, Ph.D. Thesis, University of Bradford, England (1985).

82. H. Roehrig, J. Fan, T. Furukawa, M. Ohashu, A. Chawla and K. Gandhi, Performance evaluation of LCD Displays, *Proc. CARS 2000*, CARS/Springer, 1-6 (2000).

APPENDICES

Appendix A: Fairman's Metameric Correction Using Parameric Decomposition

The theory is based on Wyszecki's[80] hypothesis that any spectral stimulus can be decomposed into a fundamental stimulus (with tristimulus values equal to those of the stimulus) and a metameric black (with tristimulus values equal to zero). Two stimuli are metameric if their fundamental stimuli are identical, and their metameric blacks are different. Two stimuli are parameric if their fundamental stimuli are different, and their metameric blacks are different. Measures of the degree of metamerism for a pair of stimuli are called indices of metamerism. In order to calculate an index of metamerism for a sample pair of stimuli, it is necessary that the pair exactly match in a reference viewing condition. Unfortunately, however, for most real samples, this limitation is not achieved. Therefore, Fairman[79] proposed metameric correction using parameric decomposition. The purpose is to correct the spectral distribution of one of the samples so that an exact tristimulus match is achieved for the reference condition. The main procedure is to decompose both the standard and the trial of a parameric pair of stimuli into their component fundamental stimuli and metameric blacks. Then the metameric black of the trial is added to the fundamental stimulus of the standard. The result is a corrected spectral distribution. The corrected spectral distribution retains the differences in spectral distribution attributable to metamerism but has been corrected for any degree of mismatch that is attributable to simple color difference. The corrected distribution is

now compared to the standard distribution using conventional formulae for index of metamerism. We will provide the main equations here. The details of derivation can be found in the reference 79.

Suppose matrix **A** is the weight set for tristimulus integration applicable to some illuminant-observer combination utilizing certain point spectrophotometry. Then an **R** matrix is defined as in Eq. A-1:

$$\mathbf{R} = \mathbf{A} \cdot (\mathbf{A}' \cdot \mathbf{A})^{-1} \cdot \mathbf{A}', \tag{A-1}$$

where the prime symbol infers the transpose of matrix, and -1 infers the inverse of matrix. Let $\mathbf{N}_s$ and $\mathbf{N}_t$ be the spectral distributions of the standard and the trial respectively. The corrected spectral distribution, $\mathbf{N}_c$, is given in Eq. A-2.

$$\mathbf{N}_c = \mathbf{R} \cdot \mathbf{N}_s + (\mathbf{I} - \mathbf{R}) \cdot \mathbf{N}_t, \tag{A-2}$$

where **I** is an identity matrix, $\mathbf{R} \cdot \mathbf{N}_s$ is the fundamental stimulus of the standard and $(\mathbf{I} - \mathbf{R}) \cdot \mathbf{N}_t$ is the metameric black of the trial. The corrected distribution is now compared to the $\mathbf{N}_s$ distribution using conventional formulae for index of metamerism for change in illuminant.

Appendix B: Procedure for Spectral Image Display Using sRGB Model

Suppose the spectral image was first taken in illuminant D_{50} and we have interest to compare its display on CRT that the display environment corresponds to complete chromatic adaptation with chromaticities equal to those of illuminant D_{50}. The first step is to calculate the XYZ tristimulus values of the spectral image using illuminant D_{50}, pixel by pixel. The following will follow the procedure described by Berns.[63] The calculation is for pixel basis.

The image tristimulus values should be transformed from illuminant D50 to illuminant D_{65}. The tristimulus values are first transformed to a set of cone responses, R, G, and R given in Eq. A-3:

$$\begin{bmatrix} R \\ G \\ B \end{bmatrix} = \begin{bmatrix} 0.8951 & 0.2664 & -0.1614 \\ -0.7502 & 1.7135 & 0.0367 \\ 0.0389 & -0.0685 & 1.0296 \end{bmatrix} \cdot \begin{bmatrix} X/Y_m \\ Y/Y_m \\ X/Y_m \end{bmatrix}, \qquad (A-3)$$

where Y_m is the Y tristimulus value of illuminant D_{50}. Eq. A-3 is also applied to illuminant D_{65} and illuminant D_{50} and get the RGB cone responses of (R_n, G_n, B_n) and (R_m, G_m, B_m) respectively. The next step is to perform so called Bradford chromatic adaptation transform.[80] The corresponding colors are calculated using Eq. A-4:

$$\begin{aligned} R_c &= \frac{R_m}{R_n} \cdot R, \\ G_c &= \frac{G_m}{G_n} \cdot G, \\ B_c &= \frac{B_m}{B_n^{\,p}} \cdot |B|^p, \end{aligned} \qquad (A-4)$$

where

$$p = (\frac{B_u}{B_m})^{0.0834}. \qquad (A-5)$$

The corresponding colors are then transformed to CIE tristimulus values to complete the chromatic adaptation transform. The equation is given in Eq. A-6:

$$\begin{bmatrix} X_c \\ Y_c \\ Z_c \end{bmatrix} = \begin{bmatrix} 0.98699 & -0.14705 & 0.15996 \\ 0.43231 & 0.51836 & 0.04929 \\ -0.00853 & 0.04004 & 0.96849 \end{bmatrix} \cdot \begin{bmatrix} R_c \cdot Y_m \\ G_c \cdot Y_m \\ B_c \cdot Y_m \end{bmatrix} \qquad (A-6)$$

To display the image on CRT, the tristimulus obtained in Eq. A-6 need to be transformed to display R, G, and B using sRGB[67] model given in Eq. A-7.

$$\begin{bmatrix} R_{display} \\ G_{display} \\ B_{display} \end{bmatrix} = \begin{bmatrix} 3.24E-2 & -1.54E-2 & -4.99E-3 \\ -9.69E-3 & 1.88E-2 & 4.16E-4 \\ 5.56E-4 & -2.04E-3 & 1.06E-2 \end{bmatrix} \cdot \begin{bmatrix} X_c \\ Y_c \\ Z_c \end{bmatrix}. \qquad (A-7)$$

Finally, a GOG[68] model that characterizing the CRT display attribution is applied to transform the display R, G, and B to CRT digital counts for display. A convention form of this transform for red channel is given in Eq. A-8 where $k_{g,r}$, γ, and $k_{o,r}$ are coefficients that need to be determined from CRT calibration. Similar expressions to Eq. A-8 are used for the green and blue channels.

$$d_r = (\frac{d_{\max}}{k_{g,r}}) \cdot (R_{display}{}^{1/\gamma} - k_{o,r}), \quad 0 \le R_{display} \le 1 \qquad (A-8)$$

Appendix C: MTF of LCD Display

LCD display is matrix addressed display. Fig. A-1 shows the LCD pixel structure when displaying different colors on screen.

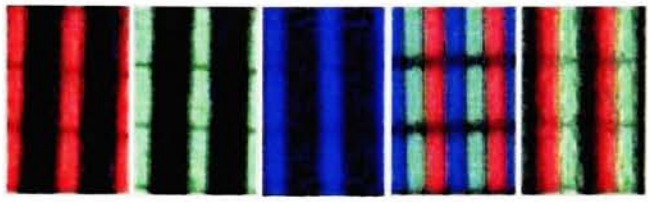

red *green* *blue* *white* *yellow*

***Figure A-1**. LCD pixel structure under microscope.*

The resolution of LCD, such as MTF, is determined only by the number picture elements. The MTF of LCD describes the information transfer with respect to spatial detail.[81] However, it is difficult to express the resolution of LCD display in terms of a MTF, because the information is sampled by the discrete elements of the display.[76] In the following we will derive the MTF of LCD based on Berten's[76] theory with some practice modification.

It is well known that MTF is equal to the absolute value of the Fourier transform of the line-spread function. It is not difficult to prove that the line-spread function of a system can be determined by differentiating the unit-step function. This method is called the knife-edge method. We first consider the horizontal resolution of green channel on LCD. Fig. A-2 shows horizontal step response of a LCD. Fig. A-2(a) shows the horizontal row of green pixel elements with pixel center-to-center distance k. The first pixel elements of this row are dark and the other is light green. The signal shown in

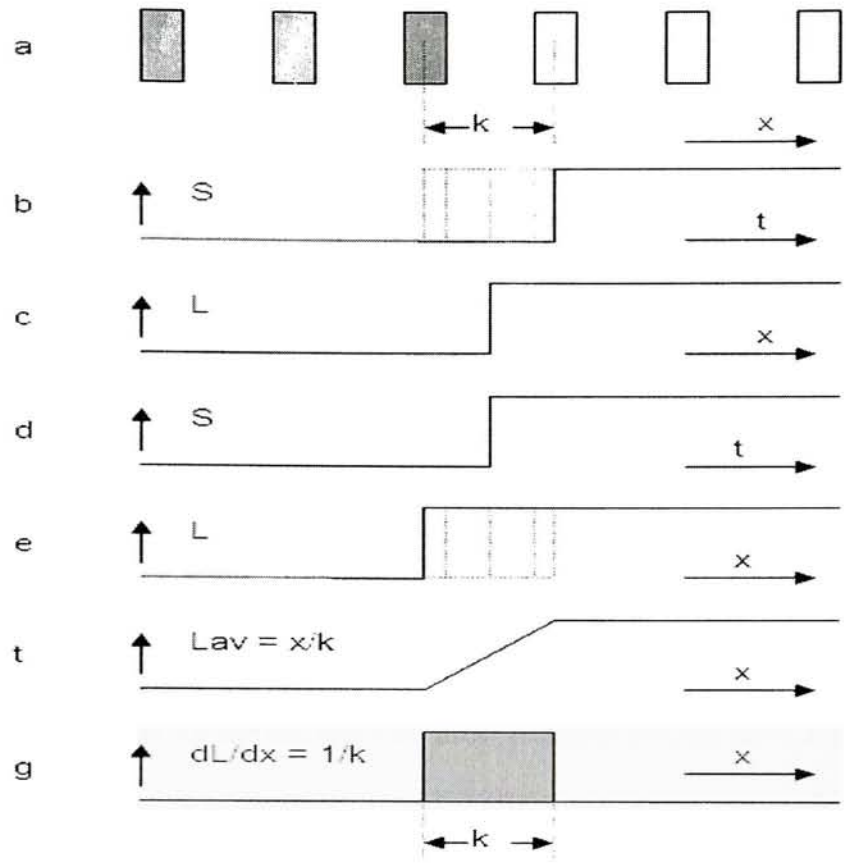

Figure. A-2. *Step response of the LCD display.*
a: row of series of dark pixel elements followed by a series of light pixel elements; b: signals that can cause this situation; c: displayed luminance transition; d: fixed unit-step signal; e: luminance response on this signal at various possible positions of the display element; f: average luminance response; g: line-spread function obtained by differentiating the average step response.

Fig. A-2 (b) causes the response at (a). However, other signals can also cause the same situation as shown by dashed lines in Fig. A-2(b). The displayed luminance transition is demonstrated in Fig. A-2(c) neglecting the interruptions between the pixel elements. For a fixed unit-step signal as shown in Fig. A-2(d) and various possible positions of the display elements with respect to the signal, the luminance response will correspond with the solid and dashed lines as shown in Fig. A-2(e). The average luminance response over

all these possible situations is given in Fig. A-2(f). By differentiating this average response with respect to x, the line-spread function is obtained shown in Fig. A-2(g). This line-spread function has a block shape with a width *k*. The Fourier transfermation of this line-spread is given in Eq. A-9:

$$F(f) = \int_{-\infty}^{\infty} \frac{dL}{dx} e^{-i2\cdot\pi\cdot f\cdot x} dx = \frac{1}{k}\cdot\int_{0}^{k} e^{-i2\cdot\pi\cdot f\cdot x} dx$$
$$= \frac{1}{i2\cdot\pi\cdot f\cdot k}(1-e^{-i2\cdot\pi\cdot f\cdot k}) = \frac{\sin(\pi\cdot f\cdot k)}{\pi\cdot f\cdot k}\cdot e^{-i\pi\cdot f\cdot k}. \qquad (A-9)$$

Thus, the MTF can be obtained as in Eq. A-10:

$$MTF = |F(f)| = \left|\frac{\sin(k\cdot\pi\cdot f)}{k\cdot\pi\cdot f}\right| \qquad (A-10)$$

The similar analysis for the red and blue pixel elements and the MTF are the same as in Eq. A-10. For the RGB white response, the distance between the pixel elements of the same color is the same *k*. In real LCD display, there is some "spreading" of the luminance displayed by the pixel elements and the shape of the pixel element is not exactly the box. Thus, the MTF of the LCD will be impacted. Therefore, in this research, the k in Eq. A-10 will be replaced with *1.2k*. The final MTF used in this research is given in Eq. A-11.

$$MTF = |F(f)| = \left|\frac{\sin(1.2\cdot k\cdot\pi\cdot f)}{1.2\cdot k\cdot\pi\cdot f}\right| \qquad (A-11)$$